Since 1955

Strojniški vestnik
Journal of Mechanical Engineering

no. 7-8
year 2021
volume 67

Strojniški vestnik – Journal of Mechanical Engineering (SV-JME)

Aim and Scope
The international journal publishes original and (mini)review articles covering the concepts of materials science, mechanics, kinematics, thermodynamics, energy and environment, mechatronics and robotics, fluid mechanics, tribology, cybernetics, industrial engineering and structural analysis.
The journal follows new trends and progress proven practice in the mechanical engineering and also in the closely related sciences as are electrical, civil and process engineering, medicine, microbiology, ecology, agriculture, transport systems, aviation, and others, thus creating a unique forum for interdisciplinary or multidisciplinary dialogue.
The international conferences selected papers are welcome for publishing as a special issue of SV-JME with invited co-editor(s).

Editorial Office
University of Ljubljana, Faculty of Mechanical Engineering
SV-JME, Aškerčeva 6, SI-1000 Ljubljana, Slovenia
Phone: 386 (0)1 4771 137
Fax: 386 (0)1 2518 567
info@sv-jme.eu, http://www.sv-jme.eu

Print: Demat d.o.o., printed in 250 copies

Founders and Publishers
University of Ljubljana, Faculty of Mechanical Engineering, Slovenia
University of Maribor, Faculty of Mechanical Engineering, Slovenia
Association of Mechanical Engineers of Slovenia
Chamber of Commerce and Industry of Slovenia, Metal Processing Industry Association

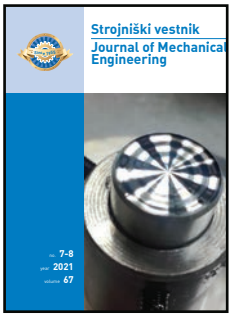

Cover:
The cover image shows a complex sinusoidal mesh surface machined through single point diamond turning technology. In actual machining, the tool path significantly affects the quality of the machined surface. To realize the determined machining accuracy effectively, the tool path that meets the machining accuracy demand can be derived by reverse application of the error calculation process according to the requisition of residual error and chord error.

Courtesy:
Jilin University, School of Mechanical and Aerospace Engineering, China

General information
Strojniški vestnik – Journal of Mechanical Engineering is published in 11 issues per year (July and August is a double issue).

Institutional prices include print & online access: institutional subscription price and foreign subscription €100,00 (the price of a single issue is €10,00); general public subscription and student subscription €50,00 (the price of a single issue is €5,00). Prices are exclusive of tax. Delivery is included in the price. The recipient is responsible for paying any import duties or taxes. Legal title passes to the customer on dispatch by our distributor. Single issues from current and recent volumes are available at the current single-issue price. To order the journal, please complete the form on our website. For submissions, subscriptions and all other information please visit: *http://www.sv-jme.eu.*

You can advertise on the inner and outer side of the back cover of the journal. The authors of the published papers are invited to send photos or pictures with short explanation for cover content.

We would like to thank the reviewers who have taken part in the peer-review process.

ISSN 0039-2480, ISSN 2536-2948 (online)

The journal is subsidized by Slovenian Research Agency.

Strojniški vestnik - Journal of Mechanical Engineering is available on *https://www.sv-jme.eu.*

Contents

Strojniški vestnik - Journal of Mechanical Engineering
volume 67 (2021) 1 , number 7 8
Ljubljana, July August 2021
ISSN 0039-2480

Published monthly

Papers

Strojniški vestnik - Journal of Mechanical Engineering 67(2021)7-8, 343-351

DOI:10.5545/sv-jme.2021.7172 Original Scientific Paper
Received for review: 2021-03-20
Received revised form: 2021-05-18
Accepted for publication: 2021-06-17

Ultra-Precision Single-Point Diamond Turning of a Complex Sinusoidal Mesh Surface Using Machining Accuracy Active Control

Peixing Ning[1] – Ji Zhao[1,2,*] – Shijun Ji[1] – Jingjin Li[1] – Handa Dai[1]
[1]Jilin University, School of Mechanical and Aerospace Engineering, China
[2]Northeastern University, School of Mechanical Engineering and Automation, China

Single-point diamond turning (SPDT) assisted with slow tool servo (STS) is the most commonly utilized technique in the fabrication of optical modules. However, the tool path significantly affects the quality of the machined surface. In order to realize the determined machining accuracy effectively, a tool path generation (TPG) method based on machining accuracy active control (MAAC) is presented. The relationship between tool path and machining error is studied. Corner radius compensation (CRC) and the calculation of chord error and residual error are detailed. Finally, the effectiveness of the proposed approach is verified through a machining error simulation and a cutting experiment of a complex sinusoidal mesh surface fabrication.

Keywords: machining accuracy active control (MAAC), machining error prediction, complex sinusoidal mesh surface, single-point diamond turning (SPDT)

Highlights

- *A tool path generation method based on active control machining error is proposed; the relationship between tool path generation parameters and machining error, including chord error and residual error, is studied.*
- *The analytical geometry method and tool contact point discretization method are used to realize tool path planning.*
- *The presented method can predict machining error and achieve the surface accuracy control before actual processing.*

0 INTRODUCTION

Single point diamond turning (SPDT) is an economical and efficient fabrication technology that can achieve an optical finish without subsequent machining [1] and [2]. At present, complex surfaces are widely used in various areas [3] and [4]. Therefore, scholars have conducted many studies on the ultra-precision machining technology of complex optical surfaces. Kong et al. [5] presented a hybrid tool servo (HTS) process and proposed a tool path generation (TPG) method. A microstructure array compound freeform surface machining experiment verified the validity of the proposed theory. Zhang et al. [6] put forward a termed toroid-surface-based slow tool servo (STS) turning method to generate discontinuously structured micro-lens arrays. Tian et al. [7] developed a novel fast tool servo system and experimented with rear-view mirrors fabrication using that system. Based on the principle of automatic dynamics analysis of mechanical systems, Khagani and Cheng [8] introduced an innovative approach for TPG. In their research, the Newton-Raphson method was used to generate the tool paths of very complex freeform surfaces; the study revealed that the time step size is very important in that method [8]. Li et al. [9] investigated a systematic approach for TPG and a theory for surface topography simulation in SPDT. A sinusoidal grid and micro-lens array sample were machined and measured to validate the effectiveness of the proposed theoretical research. Chen et al. [10] put forward a triangle rotary method; the results of the simulations and experiments showed that the presented approach was very feasible for position-velocity-time (PVT) interpolation. The presented method can decrease the interpolation error. Wei et al. [11] set up a progressive addition lens design model and proposed an optimized TPG method for diamond turning of the optical freeform surface. Ji et al. [12] designed and machined a compound freeform surface using an optimized TPG approach. Fang et al. [13] studied a cylindrical coordinate machining method for freeform surfaces fabrication, in which a typical non-uniform rational B-spline (NURBS) was utilized to fit the feature points. They also carried out a machining experiment of a compound eye structure surface to prove the theory. The above research studies mainly focused on TPG, corner radius compensation (CRC) and machined surface topography analysis. However, few studies have been conducted on the basis of TPG to ensure machining accuracy. In this study, a TPG method based on machining accuracy active control (MAAC) is proposed, and the relationship between TPG parameters and machining error, including chord error and residual error, is studied.

*Corr. Author's Address: Jilin University, School of Mechanical and Aerospace Engineering, China, jzhao@jlu.edu.cn

This paper proposed a TPG method by MAAC for complex surface SPDT assisted by STS. In Section 2, the presented method and CRC are described minutely. The relationship between tool path and machining errors is studied. An experiment for a complex sinusoidal mesh surface fabrication utilizing the proposed method is carried out in Section 3 Finally, Section 4 summarizes the paper.

1 TPG BASED ON MAAC

1.1 Machining Accuracy Active Control Method

In the process of complex mirror-like surface machining, TPG is the first and the most critical step, which has a visible impact on surface topography and surface finish of the machined workpiece. The SPDT technology is based on spindle rotary motion and linear reciprocating motion. The spindle rotation and the Z-axis reciprocating motion produce the chord error in the direction of cutting motion, and the X-axis linear motion produces the residual error in the direction of feed motion.

Considering the above two principle errors, the TPG method based on MAAC can be used as the selection basis of cutting contact points (CCPs). Thus, the tool path for SPDT of the complex surface that meets the requirements of machining errors can be obtained. The method is generally divided into the following two steps:

Firstly, the feed f should be calculated according to the requirement of residual error. Because there is a certain interval between two adjacent circles of the tool path, and the shape of the cutting edge is a circular arc, the cutting residue will be produced in the direction of cutting motion during the machining process. To calculate the residual error, the section curve in radial direction $z=f(r)$ should be obtained, and the curvature radius R_i at CCP $P_i(r_i, z_i)$ should be calculated by Eq. (1):

$$R_i = \frac{1}{K_i} = \frac{(1+(f'(r_i))^2)^{3/2}}{|f''(r_i)|}, \tag{1}$$

where K_i is the curvature at each CCP, $f'(r_i)$ is the first derivative of the section curve, $f''(r_i)$ is the second derivative of the section curve. According to the difference of curvature, the calculation of cutting residual height can be divided into three forms [14]; the principle is indicated in Fig. 1.

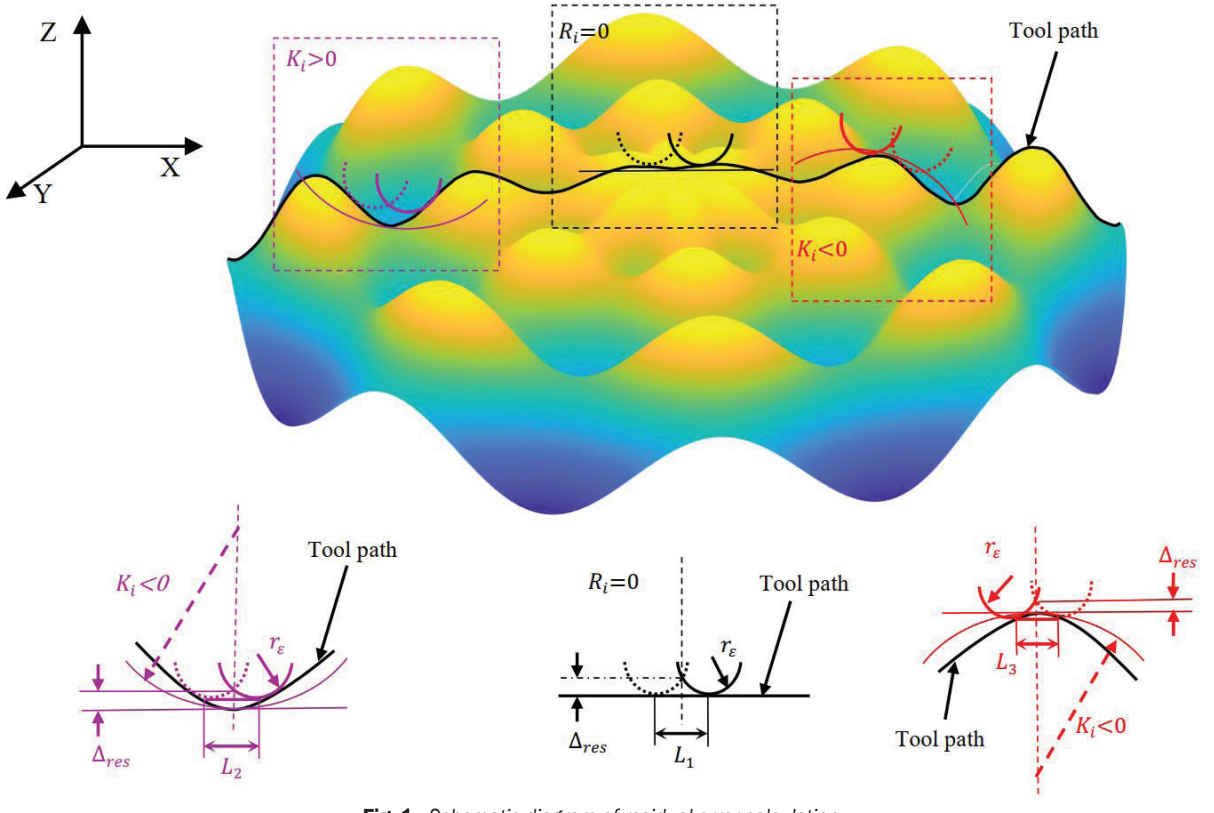

Fig. 1. *Schematic diagram of residual error calculation*

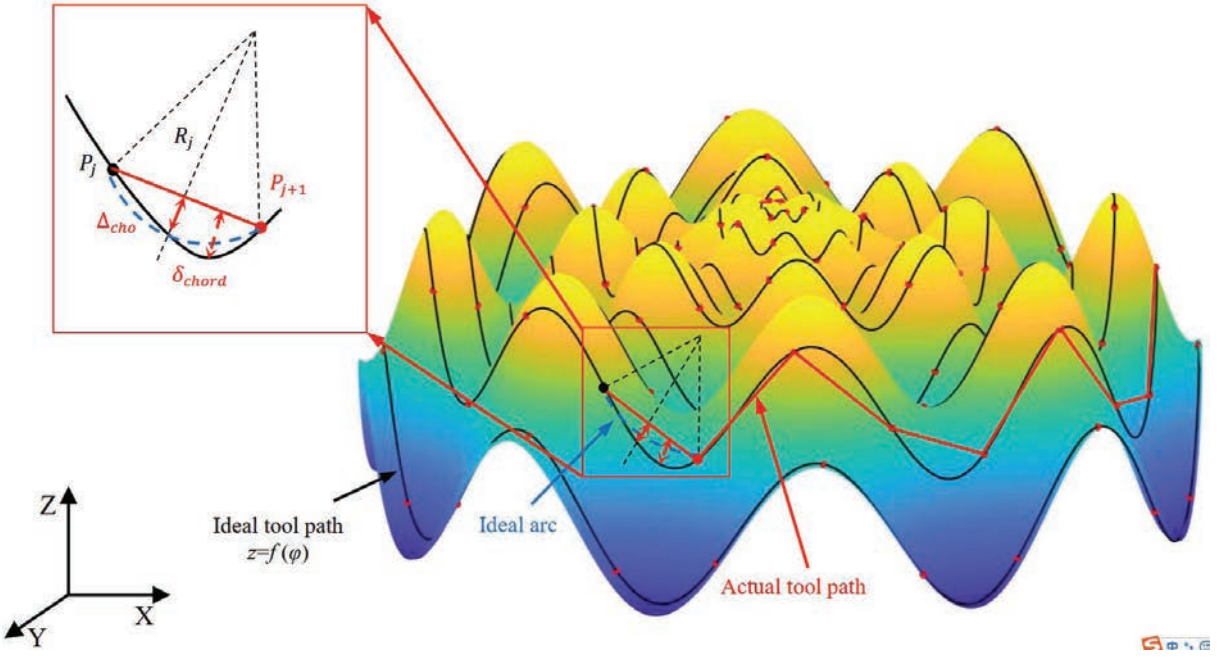

Fig. 2. *Schematic diagram of chord error calculation*

When the requirement of residual error is Δ_{res}, the feed f_i at CCP $P_i(r_i, z_i)$ can be obtained through Eqs. (2) and (3) :

$$\begin{cases} f_1 = 2\sqrt{-\Delta_{res}(\Delta_{res}-2r_\varepsilon)} & R_i = 0 \\ f_2 = \dfrac{\sqrt{-\Delta_{res}(\Delta_{res}-2R_i)(\Delta_{res}-2r_\varepsilon)(\Delta_{res}-2R_i+2r_\varepsilon)}}{(\Delta_{res}-R_i)} & R_i > 0, \\ f_3 = \dfrac{\sqrt{-\Delta_{res}(\Delta_{res}+2R_i)(\Delta_{res}-2r_\varepsilon)(\Delta_{res}+2R_i+2r_\varepsilon)}}{(\Delta_{res}+R_i)} & R_i < 0 \end{cases} \quad (2)$$

$$f_i = \min\{f_1, f_2, f_3\}. \quad (3)$$

Secondly, the TPG could be completed on the basis of the requirement of chord error. In the cutting process, the tool path between two adjacent CCPs is a straight line rather than an ideal curve. The chord error is the linear error between a realistic tool path and an ideal curve, as presented in Fig. 2. The analytical mathematical optimization TPG method can be used to realize active control for chord error: The tool path can be expressed as $z=f(\varphi)$. Because the distance between two adjacent CCPs is very small, the tool path between two points can be approximated as a circular arc. Therefore, the chord error $\Delta_{cho} \approx \delta_{chord}$. According to the geometric relationship of incipient point P_j and required chord error Δ_{cho}, the next CCP P_{j+1} could be derived from Eq. (4) :

$$\Delta_{cho} \approx \delta_{chord} = R_j - \sqrt{R_j^2 - \left(\frac{|P_j P_{j+1}|}{2}\right)^2}. \quad (4)$$

Repeating the above process with P_{j+1} as the initial point, the TPG can be finally achieved based on active control for chord error.

1.2 Corner Radius Compensation (CRC)

In the SPDT process, if the vertex of the cutting edge always moves along the CCPs, overcut will occur when curvature is not zero, and a large machining error will be leaded. To make the cutting edge always tangent to the section curve in the radial direction of the proposed surface in the machining process, the CRC is needed. Unlike the process of milling, the CCPs needs to be compensated in three directions of space. Since there is no Y direction motion in SPDT, the CRC only needs to consider the compensation in the XZ plane. The principle of CRC is detailed in Fig. 3

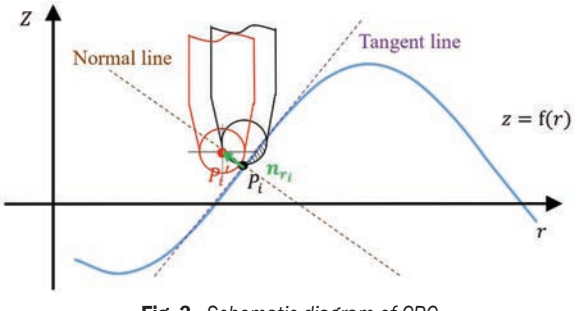

Fig. 3. *Schematic diagram of CRC*

The black line is the original position without CRC. At this point, the shaded area indicates that overcut occurred. To avoid overcut and keep the cutting point position constant, the trajectory of the CCPs $P_i(r_i, z_i)$ offsets a length of corner radius along the normal vector direction $\mathbf{n}_{r_i}$ and the CLPs $P_i(r_i, z_i)$ is obtained, as written in Eq. (5):

$$\begin{cases} r'_i = r_i - r_\varepsilon \dfrac{f'(r_i)}{\sqrt{1+f''(r_i)^2}} \\ z'_i = z_i + r_\varepsilon \dfrac{1}{\sqrt{1+f''(r_i)^2}} \end{cases}. \tag{5}$$

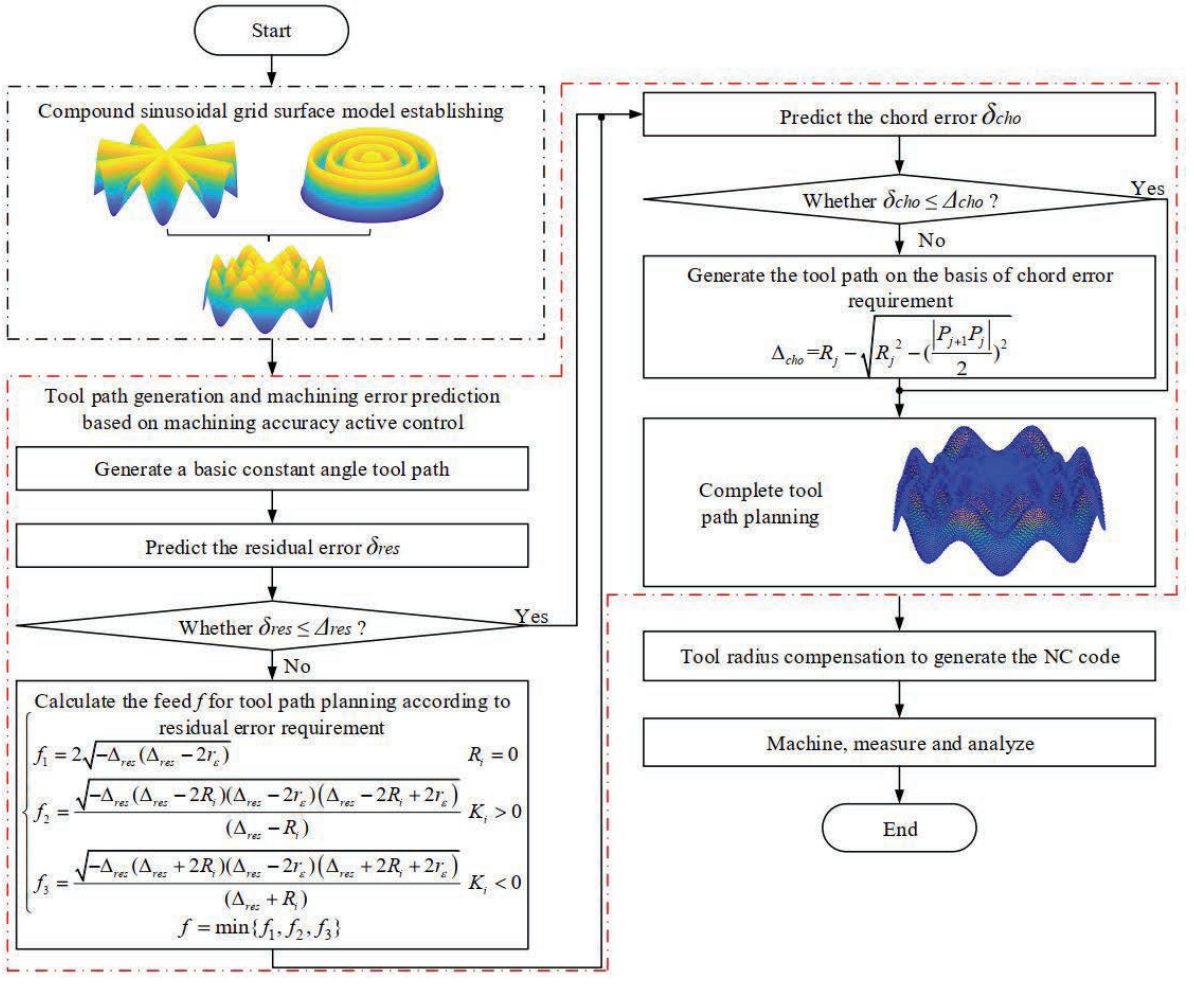

Fig. 4. *Form chart of complex sinusoidal mesh surface machining*

2 MACHINING EXPERIMENT AND DISCUSSION

To prove the feasibility of the proposed method, a machining experiment of a complex sinusoidal mesh surface is conducted. Fig. 4 presents the flowchart of SPDT process for the surface machining.

2.1 Complex Sinusoidal Mesh Surface Model Establishing

The designed complex sinusoidal mesh surface is combined with umbrella surface and radial sinusoidal surface with a gradual amplitude gradient. Therefore, the mathematical model can be established as Eq. (6):

$$Z = \left(\frac{h_1}{R_w} r \cdot \sin\left(\frac{2\pi R_w}{l}\varphi - \frac{\pi}{2}\right) - \frac{h_1}{R_w} r\right) + \left(\frac{h_2}{R_w} r \cdot \sin\left(\frac{2\pi}{\omega}\varphi\right) - \frac{h_2}{R_w} r\right), \tag{6}$$

where $\left(\frac{h_1}{R_w} r \cdot \sin\left(\frac{2\pi R_w}{l}\varphi - \frac{\pi}{2}\right) - \frac{h_1}{R_w} r\right)$ expresses

umbrella surface and $\left(\frac{h_2}{R_w} r \cdot \sin\left(\frac{2\pi}{\omega}\varphi\right) - \frac{h_2}{R_w} r\right)$ indicates complex radial sinusoidal surface; h_1 and h_2 are amplitudes of the two surfaces; l and ω are the number of sinusoids with complete periods in circumferential and radial directions, respectively; r is polar radius, R_w is radius of the workpiece, φ is polar angle.

2.2 TPG and Machining Error Prediction

The designed complex sinusoidal mesh surface is modelled as Eq. (10) with the maximum amplitude $h_{max}=0.2$ mmm, $h_1=h_2=h_{max}/4$ the number of sinusoids with complete periods in a circumferential direction is $l=8$ the number of sinusoids with complete periods in radius direction is $\omega=32/15$ the radius of workpiece $R_w=8$ mm, as shown in Fig. 5 The Δ_{res} is set as 0.5 μm and Δ_{cho} is also set as 0.5 μm. The TPG method based on MAAC is used for tool path planning of the designed surface. Fig. 6 presents the planning result.

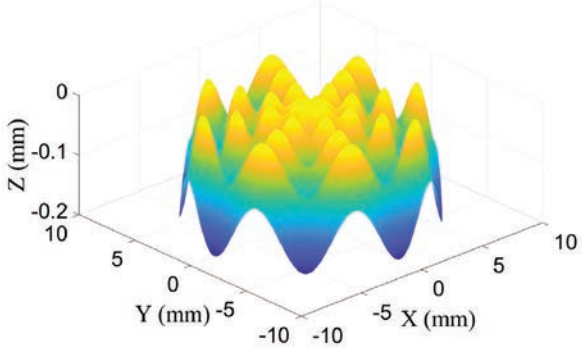

Fig. 5. *Complex sinusoidal mesh surface model*

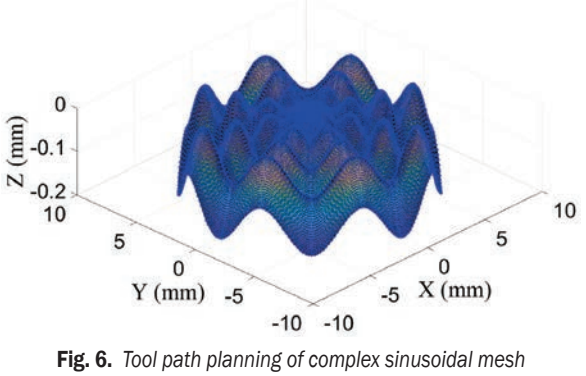

Fig. 6. *Tool path planning of complex sinusoidal mesh surface machining*

Reversing the calculation process of TPG applied above, the prediction of machining errors can be realized. The prediction consequence indicated that the errors are all maintained within 0.5 μm as shown in Fig. 7

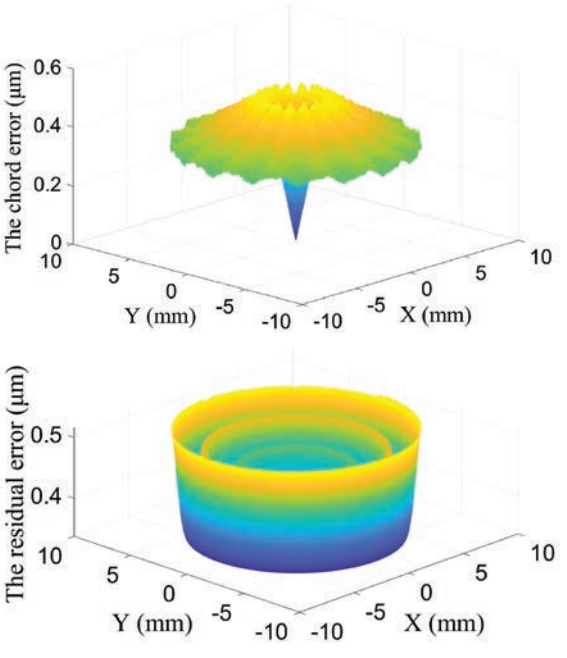

Fig. 7. *Machining error prediction; a) chord error prediction, and b) residual error prediction*

The CLPs after CRC, which can be directly applied to computerized numerical control (CNC) machine for complex sinusoidal mesh surface fabrication, is depicted in Fig. 8

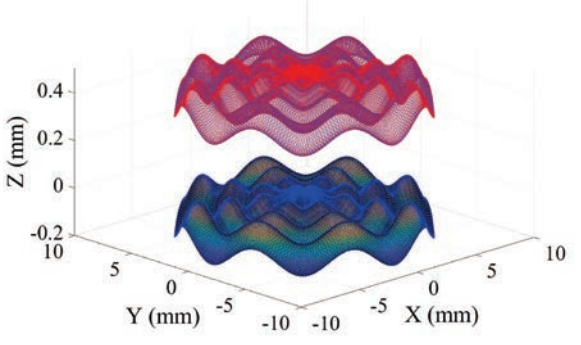

Fig. 8. *CLPs and CCPs trajectory of complex sinusoidal mesh surface machining*

2.3 Machining and Measurement Experiments

The processing experiment is conducted by using a Nanoform 2θS PDT machine. The workpiece is made of Alθθ6 . The cutting parameters are summarized in Table 1. The machine tool system and successfully machined sample are exhibited in Fig. 9

Table 1. *Cutting parameters*

Parameters	Value
Tool rake angle γ	0°
Tool clearance angle α	10°
Tool included angle ε	120°
Corner radius r_ε	0.496 mm
Depth of cut a_p	5 μm
Feed f	0.0402 mm
Average cutting speed v_c	166.72 mm/min

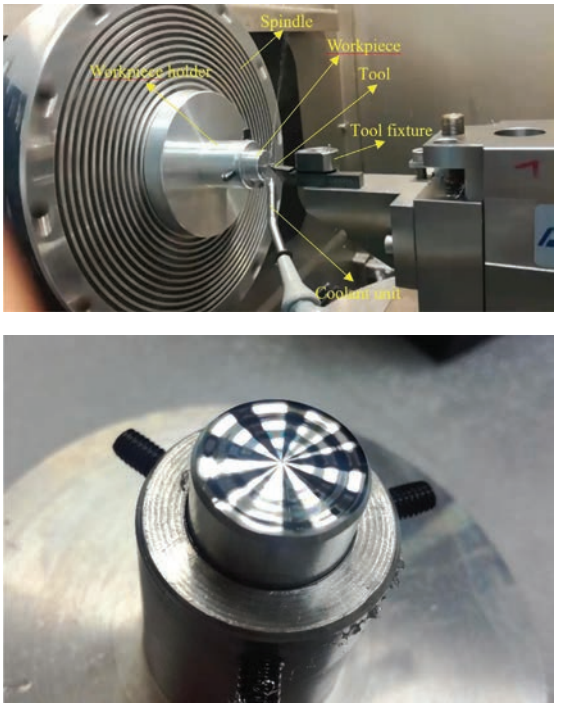

a)

b)

Fig. 9. *The machining experiment; a) machine tool system, and b) the machined complex sinusoidal mesh surface sample*

To verify the machining quality, the machined surface is measured using a newview 7300 white light interferometer profiler Zygo, as shown in Fig. 10. The measurement conditions are as follows: the enlargement factor of zoom lens was set as 1.0× (standard). The enlargement factor of the objective lens was set as 50× . The filter tray was set as Standard F1, which can be used for most surfaces measurement. The bandwidth of the filter tray Standard F1 is 125 nm, and the centre wavelength is 550 nm. The field of view in object-space was set as 0.82 mm × 0.82 mm. The measurement adopts the method of distributing points at equal distances. The number of distributing points in the X and Y directions are all 1000. Due to the limitation of the measurement vision field, eight areas on different radii of the machined surface were randomly selected for measurement,

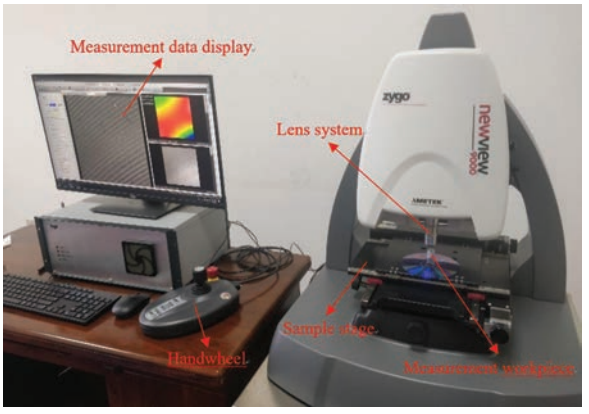

Fig. 10. *The measurement experiment*

including peak areas, valley areas and interim areas. The measurement results and the obtained machining errors are presented in Fig. 11. Figs. 11 (a1) to (h1) are reconstructed surfaces using the measurement data, and Figs. 11 (a2) to (h2) are machining errors after removing the form component of the machined surface from the original measurement data. Because the residual error and the chord error are coupled, which is inconvenient to measure and analyse separately, the machining quality can be evaluated through the peak valley (PV) value of the machined surface. PV represents the maximum peak-valley deviation of the form error of the machined surface. The residual error and the chord error could be negative. So the predicted PV can be calculated through Eq. (7) :

$$\mathrm{PV} = (\Delta_{res} + \Delta_{cho}) - (-\Delta_{res} - \Delta_{cho}) = 2\ \mu\mathrm{m}. \quad (7)$$

From Fig. 11, excluding the random error, the overall deviation (actual PV) of the machined complex sinusoidal mesh surface is about 2.459 μm, which is a little bit larger than the predetermined PV 2 μm, because there are some other uncontrollable factors such as measurement error, machine tool error, tool wear and cutting temperature. Therefore, it also can be demonstrated from the experiment result that the TPG by MAAC is usable.

3 CONCLUSIONS

In this paper, a TPG method based on MAAC is presented by studying the mapping relationship between tool path and processing errors. The simulation and experiment of a complex sinusoidal mesh surface machining attest to the validity of the method. The conclusions are drawn as follows:

1. According to the requisition of residual error and chord error, the tool path that meets the machining

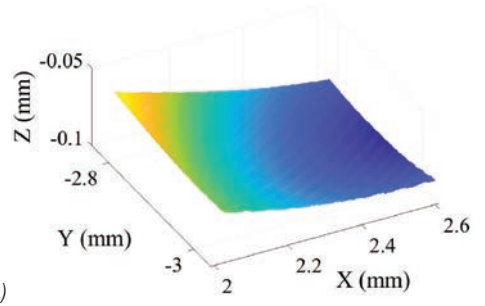

a1)

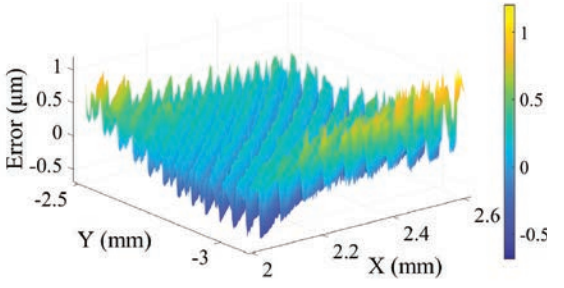

a2)

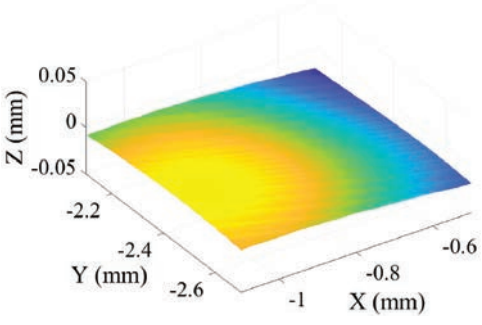

b1)

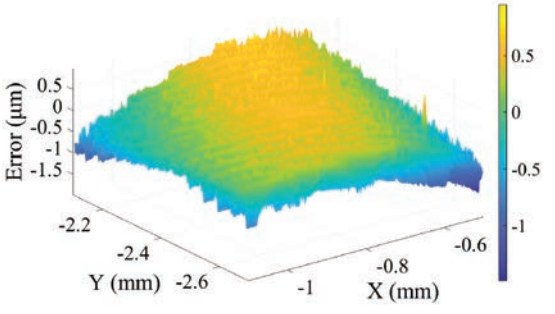

b2)

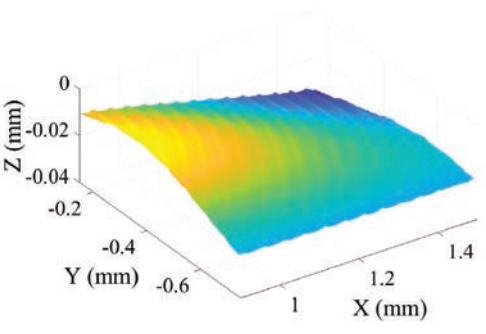

c1)

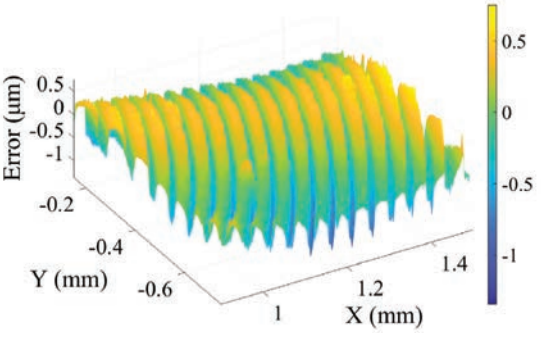

c2)

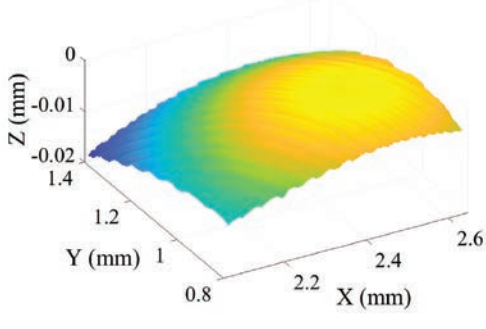

d1)

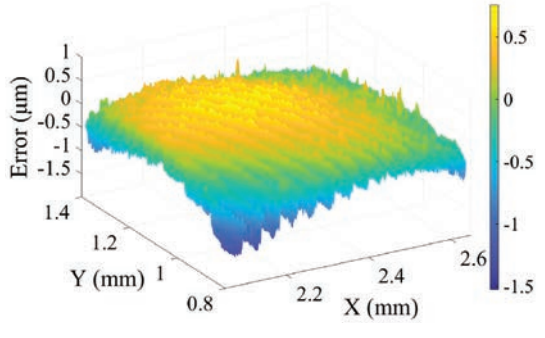

d2)

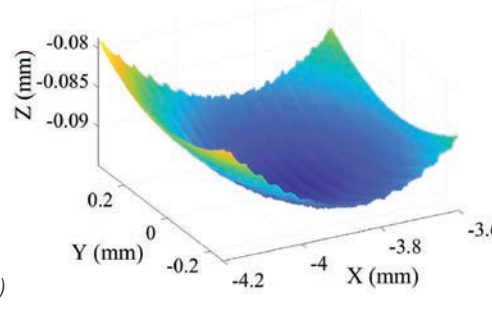

e1)

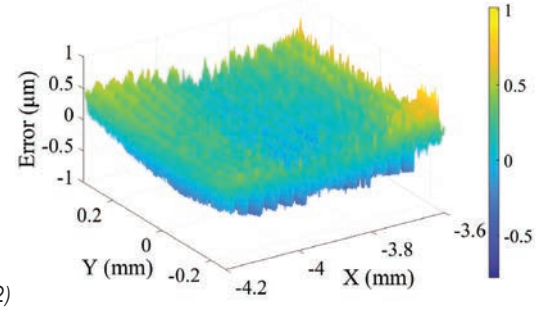

e2)

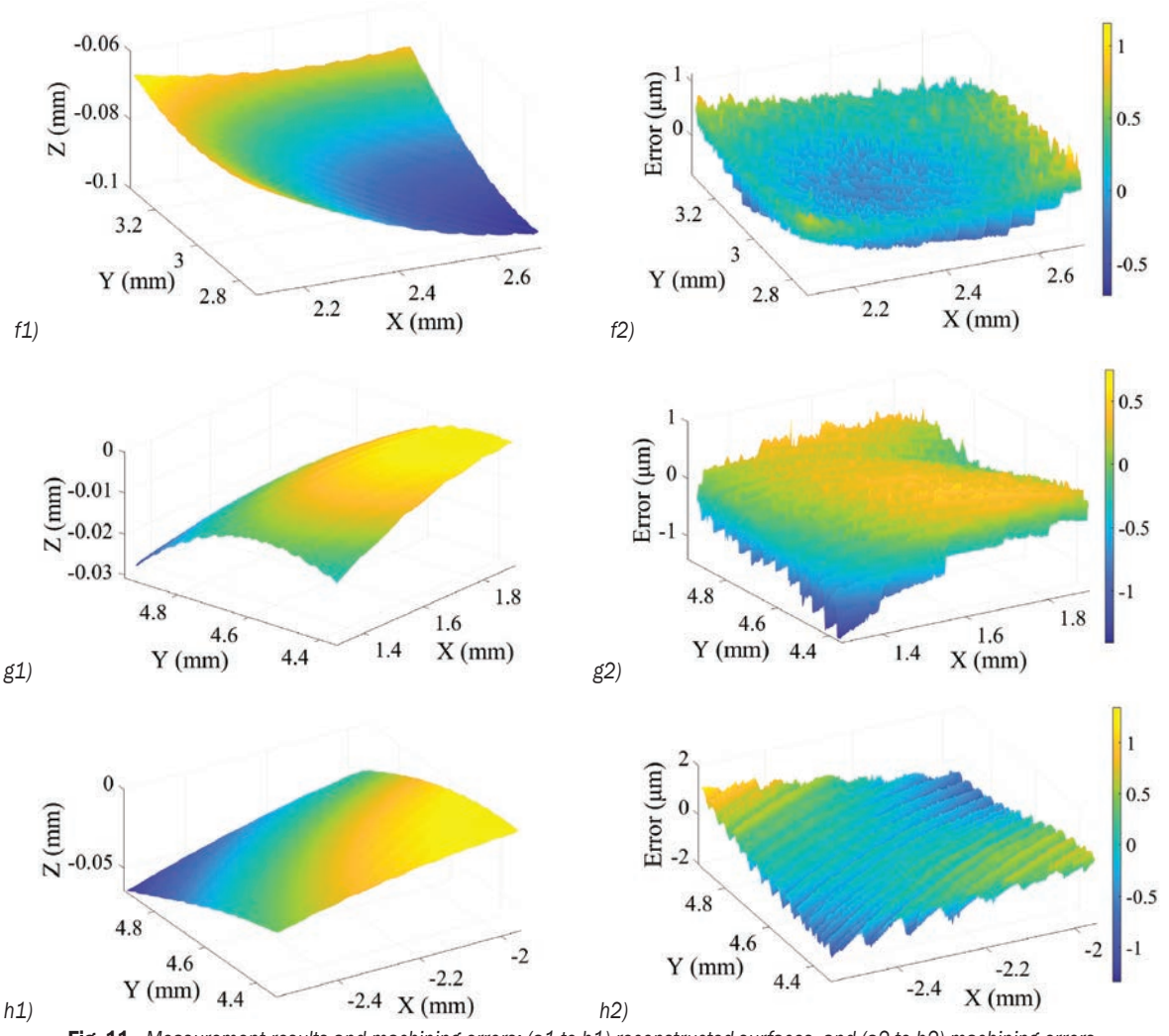

Fig. 11. *Measurement results and machining errors; (a1 to h1) reconstructed surfaces, and (a2 to h2) machining errors*

accuracy demand can be derived by reverse application of the error calculation process.

2. Using the proposed method, the TPG and CRC for a complex sinusoidal mesh surface machining are carried out systematically. The machining error simulation manifests that the generated tool path can meet the machining accuracy requirement.
3 Machining and measurement experiment results show that the PV of the machined complex sinusoidal mesh surface is not significantly different from the predetermined PV, which attest to the effectiveness of the TPG method by MAAC.

4 ACKNOWLEDGEMENTS

This work is supported by Key R&D Projects of the Ministry of Science and Technology of China (Grant Nos. 2017YFA0701200 and 2018YFB1107700) National Natural Science Foundation of China (Grant No 51775233), Graduate Innovation Fund of Jilin University (Grant No. 101832020CX122).

5 REFERENCES

[1] Zhang, S.J., Zhou, Y.P., Zhang, H.J., Xiong, Z.W., To, S. (2019). Advances in ultra-precision machining of micro-structured functional surfaces and their typical applications. *International Journal of Machine Tools and Manufacture*, vol. 142, p. 16-41, **DOI:10.1016/j.ijmachtools.2019.04.009**.

[2] He, C.L., Zong, W.J., Xue, C.X., Sun, T. (2018). An accurate 3D surface topography model for single-point diamond turning.

International Journal of Machine Tools and Manufacture, vol. 134, p. 42-68, **DOI:10.1016/j.ijmachtools.2018.07.004**.

[3] Cai, H.B., Shi, G.Q. (2019). Tool path generation for multi-degree-of-freedom fast tool servo diamond turning of optical freeform surfaces. *Experimental Techniques*, vol. 43, p. 561-569, **DOI:10.1007/s40799-019-00307-1**.

[4] Fountas, N.A., Vaxevanidis, N., V., Stergiou, C.I., Benhadj-Djilali, R. (2019). Globally optimal tool paths for sculptured surfaces with emphasis to machining error and cutting posture smoothness. *International Journal of Production Research*, vol. 57, p. 5478-5498, **DOI:10.1080/00207543.2018.1530468**.

[5] Kong, L.B., Ma, Y.G., Ren, M.J., Xu, M., Cheung, C.F. (2019). Generation and characterization of ultra-precision compound freeform surfaces. *Science Progress*, vol. 103, no. 1, **DOI:10.1177/0036850419880112**.

[6] Zhang, L., Naples, N.J., Zhou W.C., Yi, A.Y. (2019). Fabrication of infrared hexagonal microlens array by novel diamond turning method and precision glass molding. *Journal of Micromechanics and Microengineering*, vol. 29, no. 6, **DOI:10.1088/1361-6439/ab10ff**.

[7] Tian, F.J., Yin, Z.Q., Li, S.Y. (2015). Fast tool servo diamond turning of optical freeform surfaces for rear-view mirrors. *International Journal of Advanced Manufacturing Technology*, vol. 80, p. 1759-1765, **DOI:10.1007/s00170-015-7152-9**.

[8] Khaghani, A., Cheng, K. (2019). Investigation on multi-body dynamics based approach to the tool path generation for ultraprecision machining of freeform surfaces. *Proceedings of the Institution of Mechanical Engineers Part B-Journal of Engineering Manufacture*, vol. 234, no. 3, p. 571-583, **DOI:10.1177/0954405419863961**.

[9] Li, D., Qiao Z., Walton, K., Liu, Y., Xue, J.D., Wang, B., Jinag, X. (2018). Theoretical and experimental investigation of surface topography generation in slow tool servo ultra- precision machining of freeform surfaces. *Materials*, vol. 11, no. 12, **DOI:10.3390/ma11122566**.

[10] Chen, X., Kang, M., Wang, X.S., Hassan, M., Yang, J. (2017). Tool path optimal design for slow tool servo turning of complex optical surface. *Proceedings of the Institution of Mechanical Engineers Part B: Journal of Engineering Manufacture*, vol. 231, no. 5, p. 825-837, **DOI:10.1177/0954405416654192**.

[11] Wei, Y., Zhai, P., Chen, X.Y., He, L. (2020). Study on design and diamond turning of optical freeformsurface for progressive addition lenses. *Mathematical Problems in Engineering*, vol. 2020, art. ID 2850606, **DOI:10.1155/2020/2850606**.

[12] Ji, S.J., Li, J.F., Zhao, J., Feng, M., Sun, C.R, Dai, H.D. (2018). Ultra-precision machining of a compound sinusoidal grid surface based on slow tool servo. *Materials*, vol. 11, no. 6, art. ID 1001, **DOI:10.3390/ma11061001**.

[13] Fang, F.Z., Zhang, X.D., Hu, X.T. (2008). Cylindrical coordinate machining of optical freeform surfaces. *Optics Express*, vol. 16, no. 10, p. 7323-7329, **DOI:10.1364/OE.16.007323**.

[14] Lin, R.S., Koren, Y. (1996). efficient tool-path planning for machining freeform surfaces. *Journal of Engineering for Industry*, vol. 118, no. 1, p. 20-28, **DOI:10.1115/1.2803642**.

Strojniški vestnik - Journal of Mechanical Engineering 67(2021)7-8, 352-362
DOI:10.5545/sv-jme.2021.7216
Original Scientific Paper
Received for review: 2021-04-08
Received revised form: 2021-06-09
Accepted for publication: 2021-07-01

Basic Theoryan d Design Method of Variable Shaft Angle Line Gear Mechanism

Yang-zhi Chen[1,*] – Chao He[1] – Yue-ling Lyu[2]
[1]South China University of Technology, School of Mechanical and Automotive Engineering, China
[2]Sun Yat-sen University, School of Biomedical Engineering, China

In this paper, a novel line gear mechanism is proposed; it is called the variable shaft angle line gear mechanism (VSALGM). VSALGM has two rotational degrees of freedom, one is the rotation of the two gears with a constant transmission ratio, and the other is the relative swing of the two gears shafts. First, a novel contact model of VSALGM composed of one driven contact curve and one driving line teeth working surface (DLTWS) was proposed. With the concept, the basic design equations for VSALGM were derived on the basis of the space curve meshing theory of line gear. Moreover, the design criterion of pressure angle for VSALGM was analysed and proposed on the basis of the contact model. A basic design method for VSALGM was thus developed. A design example was given, and prototypes were manufactured using three-dimensional (3D) printing. Kinematic experiments and gear contact spot testing were carried out on a self-made kinematic test rig by the prototypes. The results show that the VSALGM designed in this paper can achieve a continuous, smooth and stable meshing transmission while the shaft angle is continuously changed within its setting range.

Keywords: line gear, variable shaft angle, degree of freedom, pressure angle, space curve meshing theory

Highlights

- *A variable shaft angle line gear mechanism (VSALGM) was proposed, which achieves a smooth meshing transmission with variable shaft angle.*
- *The basic theory and design of VSALGM were derived.*
- *Experiments were carried out to verify its kinematic performance.*

0 INTRODUCTION

Conventional gear pairs, including cylindrical gear pairs, bevel gear pairs and, non-cylindrical gear pairs, have a fixed shaft angle, meaning that they have only one rotational degree of freedom while working. Some applications, such as angle grinder **[1]**, flexible joint **[2]** and manipulator **[3]**, need the functions of both the constant transmission ratio and the two rotational degrees of freedom, but conventional gear pairs cannot satisfy these demands alone. Those applications **[1]** to **[3]** are generally achieved by a series connection of universal joints and gearboxes, because a universal joint has two rotational degrees of freedom, and a gearbox provides a constant transmission ratio. However, the series connection of universal joint and gearbox leads to a large structure and low transmission efficiency. Although involute gear pairs with two rotational degrees of freedom **[4]** and **[5]** have been developed, their designs are complex.

A line gear based on the space curve meshing theory **[6]** and **[7]** is dissimilar from conventional gear based on the space surface meshing theory **[8]** to **[10]**. In theory, two space conjugate curves can guarantee the transmission accuracy of line gear **[11]**. Common line gear mechanisms, including parallel axes line gear mechanisms **[12]**, intersecting axes line gear mechanisms **[13]** and skew axes line gear mechanisms **[14]**, have only one rotational degree of freedom; specifically, these common line gear mechanisms have a fixed shaft angle. The feature of common line gear mechanisms is that their driving contact curve and driven contact curve is a couple of space conjugate curves.

Based on the space curve meshing theory, a new line gear mechanism referred to as variable shaft angle line gear mechanism (VSALGM) is proposed. VSALGM has a constant transmission ratio and two rotational degrees of freedom. One of the two rotational degrees of freedom is the rotation of the two gears with a constant transmission ratio, and the other rotational degree of freedom is the relative swing of the two gear shafts.

VSALGM is composed of a pair of driving line gear and driven line gear. Different from common line gear mechanisms, VSALGM has a variable shaft angle. Specifically, VSALGM maintains a continuous, smooth and stable meshing transmission with a constant transmission ratio; its shaft angle can be continuously changed within a range.

For VSALGM, the driving contact curve and the driven contact curve are always a couple of space conjugate curves under different shaft angle, wherein the driving contact curve changes with

*Corr. Author's Address: School of Mechanical and Automotive Engineering, South China University of Technology, Guangzhou, China, meyzchen@scut.edu.cn

different shaft angles, but the driven contact curve remains unchanged. The set of driving contact curves constitutes a driving line teeth working surface (DLTWS). As long as the accuracy of the DLTWS and the driven contact curve are high, the transmission accuracy of VSALGM will be high. In addition to having the advantages of common line gear mechanisms, such as small size, a number of teeth, and a large transmission ratio, more importantly, VSALGM has the features of variable shaft angle and two degrees of freedom, which can provide a better choice for the design cases on the requirement of both constant transmission ratio and two rotational degrees of freedom. Also, it should be noted that VSALGM can only design to transmit the motion in one direction, either in the clockwise direction (CW) or counter-clockwise direction (CCW), which means there is no reversibility of VSALGM.

In this paper, the basic design equations for VSALGM were established, and the design criterion of pressure angle for VSALGM was proposed. Furthermore, based on the pressure angle rule, a parameters selection method of the basic design equations is given. According to the method, a design example was given, and kinematics experiments were completed. Finally, the gear contact spot testing was carried out.

1 METHODS

1.1 Basic Design Equations for VSALGM

For VSALGM, the driving line gear and the driven line gear rotate around their axis with a constant angular velocity, respectively; meanwhile, the shaft angle of VSALGM can be continuously changed within a range. The design equations are deduced in the following section.

VSALGM can transmit under different shaft angle; its coordinates system is as shown in Fig. 1.

The design equations for VSALGM are denoted in the space curve meshing coordinates, as shown in Fig. 1. The coordinate system $O-xyz$ is set as a fixed Cartesian coordinate system arbitrarily. The coordinate system $O_p-x_py_pz_p$ is determined by the position of the coordinate system $O-xyz$. The $x_pO_pz_p$ plane coincides with the xOz plane. The distance from O_p to z axis is denoted as a_0, the distance from O_p to x axis as b_0, and the included angle between z axis and z_p axis as θ_z. θ_z is the shaft angle, the range of θ_z is from 0° to 90° ; The designed minimum shaft angle is denoted as $\theta_{z-\min}$ and the designed maximum shaft angle as $\theta_{z-\max}$. The gear shaft z_a and the gear shaft z_b are the shafts of line gear A and line gear B; they are collinear with z axis and z_p axis, respectively. Line gear A rotates around the z axis for an angle φ_a by a uniform angular velocity $\boldsymbol{\omega}_a$. Line gear B rotates around the z_p axis for an angle φ_b by a uniform angular velocity $\boldsymbol{\omega}_b$. In this paper, line gear A is the driven wheel, line gear B is the driving wheel; curve C_1 represents the driving contact curve, curve C_2 represents the driven contact curve; the transmission ratio is denoted as i, and $i=\varphi_b/\varphi_a$.

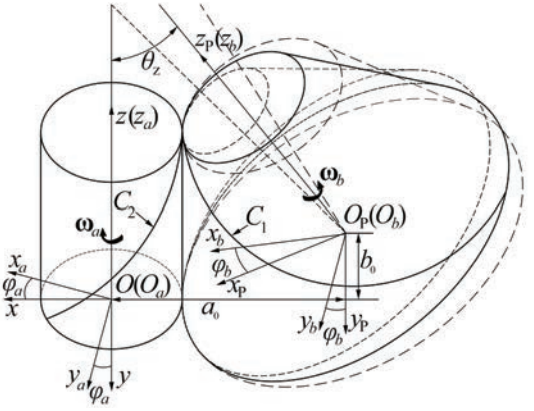

Fig. 1. *Space curve meshing coordinates for VSALGM*

According to [13], the contact curves of intersecting axes line gears are a couple of space conjugate curves, composed of one cylinder helix curve and one cone helix curve. In this paper, the cone helix curve is defined as the driving contact curve and the cylinder helix curve as the driven contact curve. The equations for the driving contact curve and the driven contact curve are given as Eqs. (1) and (2) in their coordinate systems, respectively.

$$\begin{cases} x_{\mathrm{M}}^{(b)} = -\left((m-a_0)\cos\theta_z + (n\pi+nt-b_0)\sin\theta_z\right) \\ \quad \times\cos(it+i\pi) \\ y_{\mathrm{M}}^{(b)} = \left((m-a_0)\cos\theta_z + (n\pi+nt-b_0)\sin\theta_z\right) \\ \quad \times\sin(it+i\pi) \\ z_{\mathrm{M}}^{(b)} = (m-a_0)\sin\theta_z + (n\pi+nt-b_0)\cos\theta_z \end{cases}, \tag{1}$$

$$\begin{cases} x_{\mathrm{M}}^{(a)} = m\cos t \\ y_{\mathrm{M}}^{(a)} = m\sin t \\ z_{\mathrm{M}}^{(a)} = n\pi + nt \end{cases}, \tag{2}$$

where m denotes the helix radius of the driven contact curve; n is the pitch parameter of the driven contact curve, denoting the pitch as p_n, $n=p_n/2\pi$; θ_z is the shaft angle; t is an independent variable, which also indicates the scope of the driven contact curve, that

$t=[0,2\pi]$ means a circle of the driven contact curve. The lengths of driving contact curve and driven contact curve are directly controlled by the scope of t on demand.

For VSALGM, its shaft angle is another independent variable. It can be seen from Eq. (1) that different driving contact curves are corresponding to different shaft angles. In other words, there are a series of corresponded driving contact curves when the shaft angle is continuously changed in a certain range. Accordingly, a DLTWS is constituted by the set of the driving contact curves. The equation for the DLTWS is denoted as Eq. (3) in the coordinate system $O_p-x_py_pz_p$.

$$\begin{cases} x_M^{(b)} = -\left(\left(m-a_0\right)\cos\theta_z + \left(n\pi+nt-b_0\right)\sin\theta_z\right) \\ \quad \times\cos\left(it+i\pi\right) \\ y_M^{(b)} = \left(\left(m-a_0\right)\cos\theta_z + \left(n\pi+nt-b_0\right)\sin\theta_z\right) \\ \quad \times\sin\left(it+i\pi\right) \\ z_M^{(b)} = \left(m-a_0\right)\sin\theta_z + \left(n\pi+nt-b_0\right)\cos\theta_z \\ \theta_z = \pi t_1 \end{cases}, \quad (3)$$

where θ_z denotes the shaft angle of VSALGM, which is an independent variable in this paper, and t_1 represent the scope parameter of the shaft angle.

It should be indicated that θ_z is a constant in Eq. (1) but a variable in Eq. (3). The basic design equations for VSALGM are set as Eqs. (2) and (3), respectively.

1.2 Contact Model for VSALGM

Based on the above basic design equations, the contact model for VSALGM was established by the Wolfram Mathematica software, as shown in Fig. 2.

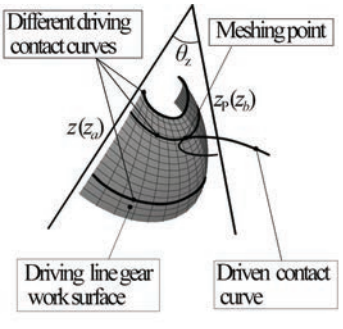

Fig. 2. *Contact model for VSALGM*

VSALGM can transmit under different shaft angles; its meshing process is similar to the common line gear mechanisms when it transmits under a fixed shaft angle. Different driving contact curves on the DLTWS always mesh with the same driven contact curve, while the shaft angle is continuously changing within the setting range.

Two points need to be explained further. One is that VSALGM can only mesh in one direction, either CW or CCW. The other is that the two degrees of freedom of VSALGM do not impact each other. The shaft angle can be changed whether the gears rotate or not; and VSALGM can mesh while the shaft angle continuously changing. A constant transmission ratio remains unchanged when the transmission was conducted from the driving wheel to the driven wheel.

1.3 Analysis of Pressure Angle for VSALGM

For gears, pressure angle (denoted as α) has a great influence on the transmission performance: the larger the pressure angle is, the smaller the effective transmission force will be [15]. It is worse for VSALGM that large deformation would be caused by the radial and axial components of the contact force applied on the cantilevered teeth [16]. Even more so, self-lock would be caused by excessive pressure angle, which would make the gear pair unable to be driven. In other words, the value of driving torque must be greater than the value of maximum friction torque for the driven wheel. In this paper, the driving torque is denoted as M_a, and $M_a \le F\,m\cos\alpha$, where F denotes the contact force; The maximum friction torque is denoted as M_μ, and the static friction coefficient is as μ. In order to avoid self-lock, the value of driving torque must be greater than the value of maximum friction torque, which is that $M_\mu \le \mu F\,m \le M_a \le F\,m\cos\alpha$ [17]. In other words, the value range of pressure angle is as follows: $\alpha \le \arccos\mu$. Therefore, the allowable value of pressure angle depends on the maximum static friction coefficient of the gear pair. For commonly-used materials of line gear pairs [18], the typical value of the maximum friction coefficient is no greater than 0.7 under the condition of poor or no lubrication [19]. Therefore, the allowable value of pressure angle is derived as follows: $\alpha \le 45°$. Moreover, the design criteria of pressure angle for involute gear and non-circular gear is used as a reference. For the involute gear, the standard pressure angle is equal to 20° in the China standard [20], and the maximum pressure angle is approximately equal to 35° when the addendum coefficient is equal to 1 or 0.8 [21]. For the non-circular gear, the maximum pressure angle must be designed to less than 65° [22]. In summary, the design criterion of pressure angle for VSALGM is as follows: $\alpha \le 45°$.

1.4 Parameters Selection Method for VSALGM Based on Pressure Angle Rule

The value of the pressure angle is determined by the parameters of the basic design equations for VSALGM. The parameters selections are diversified in the basic design equations when designing a pair of line gear. To ensure that the pressure angle is within the allowable range, a parameter selection method was given.

First, the calculation formula for the pressure angle was derived. The pressure angle exists during the transmission between the driving wheel and the driven wheel. The pressure angle is defined as the acute angle between the direction of the contact force and the direction of linear velocity at the meshing point on the driven wheel. The contact form of line gear belongs to point contact. According to the contact model, at the meshing point, the direction of the force for the driven wheel is overlapped with the normal direction of the DLTWS, and the expression of the normal vector of the DLTWS is as Eq. (34).

$$\mathbf{f}=\begin{bmatrix} i_1 & j_1 & k_1 \\ x_t' & y_t' & z_t' \\ x_{\theta_z}' & y_{\theta_z}' & z_{\theta_z}' \end{bmatrix}. \tag{34}$$

In Eq.(34), i_1, j_1 and k_1 represent the three unit vectors in a Cartesian coordinate system, x_t', y_t' and z_t' represent the partial derivative of t, x_{θ_z}', y_{θ_z} and z_{θ_z}' represent the partial derivative of θ_z.

Next, the parameters are substituted into Eq. (34), at the meshing point, the expression of the normal vector of the DLTWS in the coordinate system $O_b-x_by_bz_b$ can be obtained as Eq. (35).

$$\mathbf{f}_b=\begin{bmatrix} i\cos\left(it+i\pi\right)\left(\left(-a_0+m\right)\cos\theta_z-i\sin\theta_z\left(n\left(t+\pi\right)-b_0\right)\right)^2+n\left(n\left(t+\pi\right)-b_0\right)\sin\left(it+i\pi\right) \\ in\left(n\left(t+\pi\right)-b_0\right)\cos\left(it+i\pi\right)-i\sin\left(it+i\pi\right)\left(\left(-a_0+m\right)\cos\theta_z-i\sin\theta_z\left(n\left(t+\pi\right)-b_0\right)\right)^2 \\ \dfrac{-i\sin 2\theta_z-\left(m-a_0\right)^2+\left(b_0-n\left(t+\pi\right)\right)^2-2i\left(a_0-m\right)\left(b_0-n\left(t+\pi\right)\right)\cos 2\theta_z}{2} \end{bmatrix}. \tag{35}$$

At the meshing point, the expression of the linear velocity for the driven wheel in the coordinate system $O_a-x_ay_az_a$ is as shown in Eq. (36).

$$\mathbf{v}_a=\begin{bmatrix} -m\sin\left(t\right) \\ m\cos\left(t\right) \\ 0 \end{bmatrix}. \tag{36}$$

Eq. (35) can be seen as the expression of the direction of the contact force. To calculate the pressure angle, the expression of the direction of the contact force needs to be converted from the coordinate system $O_b-x_by_bz_b$ to the coordinate system $O_a-x_ay_az_a$. The transformation matrix from the coordinate system $O_b-x_by_bz_b$ to the coordinate system $O_a-x_ay_az_a$ is as shown in Eq. (37).

$$\mathbf{M}_{ba}=\begin{bmatrix} \cos\theta_z\cos\varphi_a\cos\varphi_b-\sin\varphi_a\sin\varphi_b & \cos\varphi_a\sin\varphi_b+\cos\theta_z\cos\varphi_b\sin\varphi_a & \cos\varphi_b\sin\theta_z & -\cos\varphi_b\left(b\sin\theta_z+a\cos\theta_z\right) \\ -\cos\theta_z\cos\varphi_a\sin\varphi_b-\cos\varphi_b\sin\varphi_a & \cos\varphi_a\cos\varphi_b-\cos\theta_z\sin\varphi_a\sin\varphi_b & -\sin\theta_z\sin\varphi_b & \left(-a\cos\theta_z+b\sin\theta_z\right)\sin\varphi_b \\ -\cos\varphi_a\sin\theta_z & -\sin\theta_z\sin\varphi_a & \cos\theta_z & -b\cos\theta_z-a\sin\theta_z \\ 0 & 0 & 0 & 1 \end{bmatrix}. \tag{37}$$

For the driven wheel, the expression of the direction of the contact force in the coordinate system $O_a-x_ay_az_a$ is as follows: $\mathbf{F}_a=\mathbf{M}_b\ \mathbf{f}_b$.

Finally, according to the calculation formula for the spatial angle between two vectors, for VSALGM, its calculation formula of the pressure angle is deduced as Eq. (38).

$$\alpha=\arccos\left[\frac{\left|\mathbf{f}_a\mathbf{v}_a\right|}{\left|\mathbf{f}_a\right|\left|\mathbf{v}_a\right|}\right]. \tag{38}$$

In order to analyse the values and distributions of the pressure angle more intuitively, calculation example 1 was given referring to [13], and the parameters of VSALGM were as follows: $m=12.5$ mm, $n=6$ mm, $a_0=8$ mm, $b_0=10$ mm, $i=0.5$ mm, $\theta_z=[0°, 8°]$ and $t=[0, 10]$. In calculation example 1, the values and distributions of the pressure angle were obtained by using Eq. (38), and the distribution graph was plotted by using Wolfram Mathematica software, as shown in Fig. 3

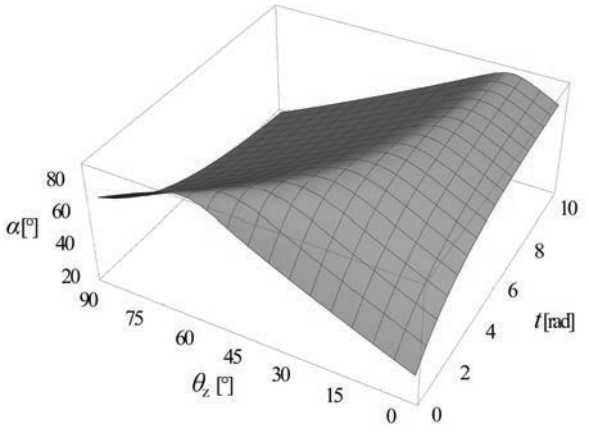

Fig. 3. *The pressure angle distribution graph in calculation example 1*

It can be seen from Fig. 3 that the pressure angle goes beyond the allowable value in some parameter ranges, which may cause self-lock. Therefore, acceptable design parameters must be chosen to ensure that the pressure angle is always within the allowable range.

Parameters including m, n, a_0, and b_0 are usually selected according to the geometric parameters selections of line gear pairs [23], and the transmission ratio i is selected on the requirement of practical design. From Fig. 3 it can be seen that different areas in the pressure angle distribution graphs can be selected by θ_z and t, which means that the pressure angle can be controlled within the allowable range when a reasonable range of θ_z and t are selected. In general, the value range of θ_z is determined on the requirement of practical design. The value range of t is chosen under the conditions of that $\alpha \leq 45°$ and that the contact ratio of line gear greater than 1 with non-interference [24].

The above analysis shows that the value of pressure angle can be controlled by the selection of the variable t. Therefore, the basic design method for VSALGM can be summarized as follows: On the first step, the basic design equations for VSALGM are calculated. On the second step, parameters i and θ_z are selected on the requirement of practical design; Parameters m, n, a_0, and b_0 are selected according to the geometric parameters selections of line gear pairs [23], and parameter t is selected according to the design criterion of pressure angle. On the third step, the 3D models are designed by using the 3D Design Software. In short, the basic design method for VSALGM can be described by the design flow chart in Fig. 4.

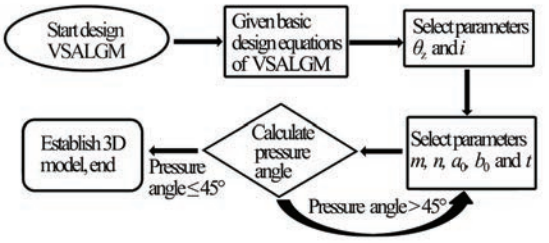

Fig. 4. *Design flow Chart for VSALGM*

Usually, the driving gear and driven gear are installed in their corresponding position. When the driving gear and driven gear have to swap positions, it is necessary to recalculate whether the pressure angle is within the allowable range or not; the calculation method refers to the above analysis.

2 EXPERIMENTAL

2.1 Design Example 2

According to the basic design method for VSALGM proposed in Section 1, design example 2 was derived based on calculation example 1. It is necessary to indicate that the range of shaft angle is selected on specific requirements. In design example 2, the original parameters were set as follows: $m = 12.5$ mm, $n = 6$ mm, $a_0 = 8$ mm, $b_0 = 10$ mm, $i = 0.5$ mm, $\theta_z = [75, 90°]$ and $t = [5, 9]$. The pressure angle distribution graph of design example 2 was shown in Fig. 5

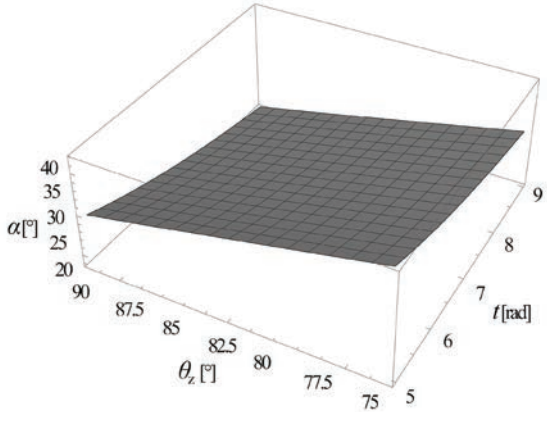

Fig. 5. *Pressure angle distribution graph for design example 2*

For design example 2, when the relevant parameters are substituted into Eq. (3), the equation for the DLTWS is obtained as Eq. (9).

$$\begin{cases} x_{\mathrm{M}}^{(b)} = \left(17.5\cos\theta_{\mathrm{z}} + \left(6\pi + 6t - 10\right)\sin\theta_{\mathrm{z}}\right)\cos 2t \\ y_{\mathrm{M}}^{(b)} = -\left(17.5\cos\theta_{\mathrm{z}} + \left(6\pi + 6t - 10\right)\sin\theta_{\mathrm{z}}\right)\sin 2t \\ z_{\mathrm{M}}^{(b)} = -17.5\sin\theta_{\mathrm{z}} + \left(6\pi + 6t - 10\right)\cos\theta_{\mathrm{z}} \end{cases}. \quad (9)$$

When the relevant parameters are substituted into Eq. (2), the equation for the driven contact curve is obtained as Eq. (10).

$$\begin{cases} x_{\mathrm{M}}^{(a)} = 12.5\cos t \\ y_{\mathrm{M}}^{(a)} = 12.5\sin t \\ z_{\mathrm{M}}^{(a)} = 6\pi + 6t \end{cases}. \quad (10)$$

The tooth model of the driven gear was established by using the Unigraphics NX software. Specifically, a completed DLTWS was fitted and constructed depending on six driving contact curves, which correspond to six shaft angles (74°, 78°, 82°, 86°, 90°, 94°). In order to make VSALGM work properly in the theoretical scope, the practical value range of θ_{z} is slightly greater than the theoretical scope. The structures of the areas, where the shaft angle is out of the setting scope, only play a role of support, but do not participate in transmission. By using the Unigraphics NX software, the fitted DLTWS and the tooth model were obtained, as shown in Fig. 6. The six curves on the driving tooth surface in Fig. 6 represent the six driving contact curves of the above design.

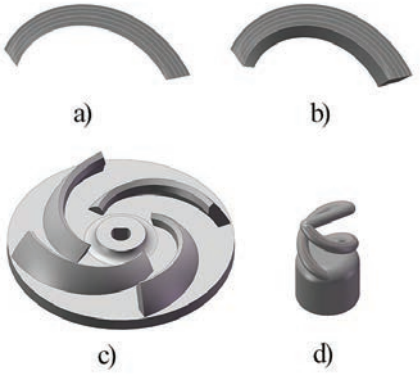

Fig. 6. *3D model of VSALGM; a) fitted DLTWS, b) fitted tooth model, c) driving line gear model, and d) driven line gear model*

Fig. 6a shows one driving tooth surface, Fig. 6b shows a driving tooth model, Fig. 6c shows the driving line gear model, and Fig. 6d shows the driven line gear model.

According to the construction method of the normal line gear teeth, the driven tooth was generated by the function of ScanTo3D in the SolidWorks software, with the driven contact curve as the boundary and a 5 mm diameter circle as the outline, as shown in Fig. 6. The designed structure of line gear has a small volume and light weight. The line gear has the characteristic of a small number of teeth. The tooth number of the driving line gear was set as 4, and the driven line gear as 2. The completed line gear was obtained by connecting the line gear teeth.

2.2 Kinematics Experiments for VSALGM

The prototypes were made by 3D printing according to the above model, as shown in Fig. 7. According to the product manual, the tolerance of the 3D printing line gears is 200 microns.

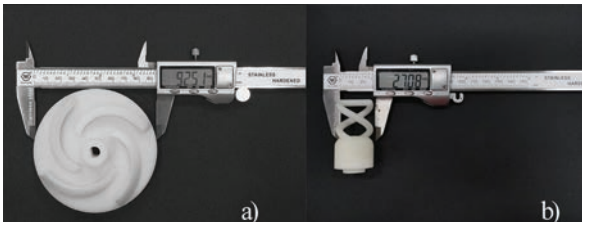

Fig.7. *Prototypes of VSALGM: a) driving wheel, and b) driven wheel*

It can be seen from Fig. 7b that the driven gear consists of a small spiral tooth; therefore, VSALGM can only be used for small loads.

The kinematics performance of VSALGM was verified in the self-made kinematics test rig, as shown in Fig. 8.

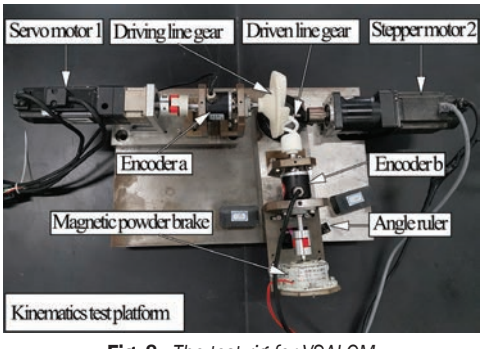

Fig. 8. *The test rig for VSALGM*

According to [25], kinematics experiments for VSALGM were carried out using the self-made kinematics test rig, as shown in Fig. 8. The two gears were installed. The geared servo motor 1 generated a clockwise motion, and the driving wheel transmitted the motion to the driven wheel. The geared stepper motor 2 generated another motion making the shaft angle be changed. There were two encoders installed on the driving wheel and the driven wheel for

recording the angular displacements of the two gears, respectively. A magnetic powder brake connected to the driven wheel, which generated the load. The speed and angular displacement of the geared servo motor 1 can be quantitatively controlled through the motion controller installed on a personal computer. The pulse signals of the two encoders (output 20000 pulses per revolution) are obtained by the data acquisition card installed on the personal computer. The angular displacement of each gear can be obtained from the collected pulse signals.

The kinematics experiments were conducted by three groups, and each group included the testing of fixed shaft angle (8 °, 82° and 86) and the testing of continuously changing shaft angle. The three groups were conducted on the condition of different loads. VSALGM is only suited for small loads. Therefore, the load was set as 0 N·mm in group 1, 0 N·mm in group 2 and 0 N·mm in group 3 The geared servo motor 1 was set as 1.6 rpm. The sampling frequency of the two encoders was set as 20 Hz in the experiment. The geared stepper motor 2 was set as 0.03 rpm, for continuously changing the shaft angle from 90° to 75 . The transmission performance of VSALGM varies periodically relating to the number of teeth. In this paper, the driving line gear and the driven line gear rotated 2 revolutions and 4 revolutions, respectively, during the tests, which mean the testing time equal to 72 s .

2.3 Gear Contact Spot Testing

In this paper, the red lead powder was used as the developer in the gear contact spot testing to research the contact form of VSALGM. The developer was evenly smeared on the driving gear tooth surface, as shown in Fig. 9 When the two gears are meshed, the developer will stick to the driven wheel from the driving wheel at the contact point, and the developer will be driven away at the contact point because of the contact force. The contact spots on the two gear tooth surfaces can be observed after the two gears meshed.

In the gear contact spot testing, the gear pair was installed on the self-made gear kinematics test rig, and the load was set to 0 N·mm. The gear contact spot testing was successively conducted under two different shaft angles (82° and 86), and the contact spots on the two gears tooth surfaces were obtained.

Fig. 9. *Diagram of the gear contact spot testing*

3 RESULTS

In order to study the kinematic performance of VSALGM, the experiments were conducted when the designed gears meshed at different shaft angles. The transmission error is the difference between the real angular displacement and the theoretical angular displacement of the driven line gear shaft [26]. According to [27], the data of the transmission error were measured through the collected encoder's data when the designed gears meshed at different shaft angles, as shown in Figs. 10 to 12.

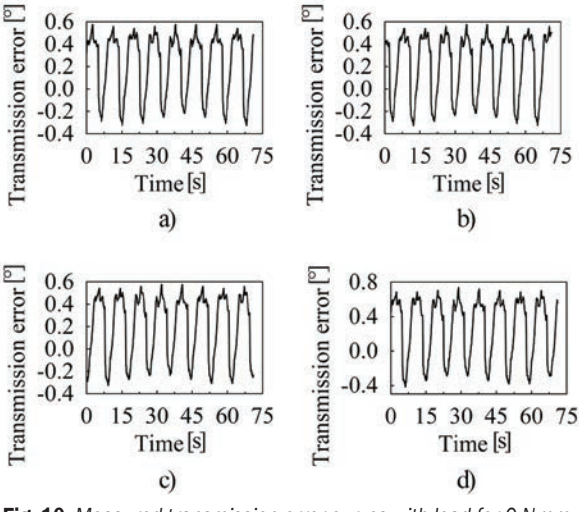

Fig. 10. *Measured transmission error curves with load for 0 N·mm: a) θ_z = 88°; b) θ_z = 82°; c) θ_z = 76°; d) θ_z changing from 90° to 75°*

In Figs. 10 to 12, the four different curves in each figure show the three fixed shaft angle testing results and the changing shaft angle testing result on the condition of different loads. For each transmission error curve, the curve between the bottoms of every two peaks represents 1 tooth rotation, and the bottom of each peak represents the contact conversion

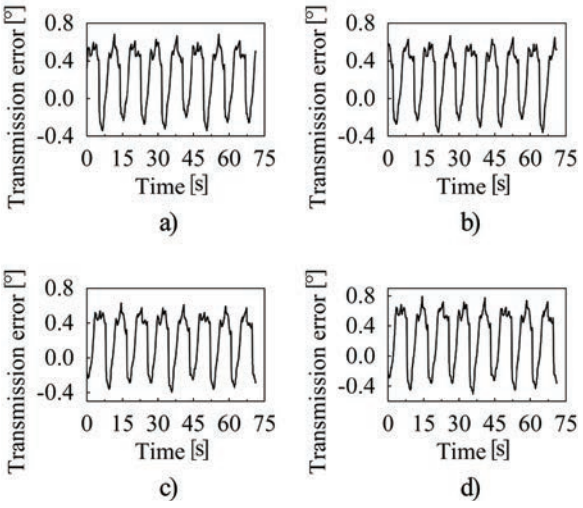

Fig. 11. *Measured transmission error curves with load for 30 N·mm: a) θ_z = 88°; b) θ_z = 82°; c) θ_z = 76°; d) θ_z changing from 90° to 75°*

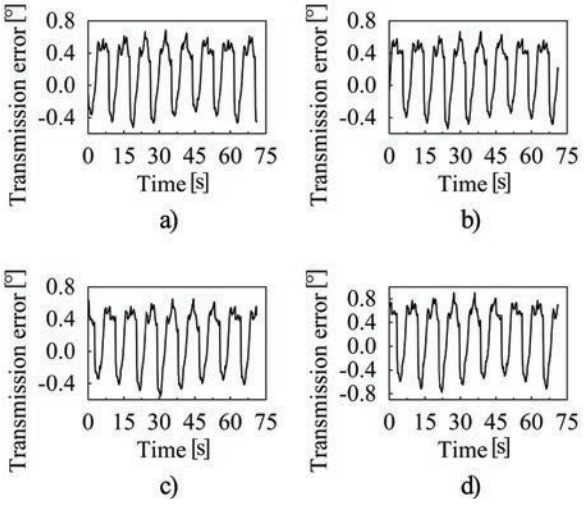

Fig. 12. Measured transmission error curves with load for 60 N·mm: a) θ_z = 88°; b) θ_z = 82°; c) θ_z = 76°; d) θ_z changing from 90° to 75°

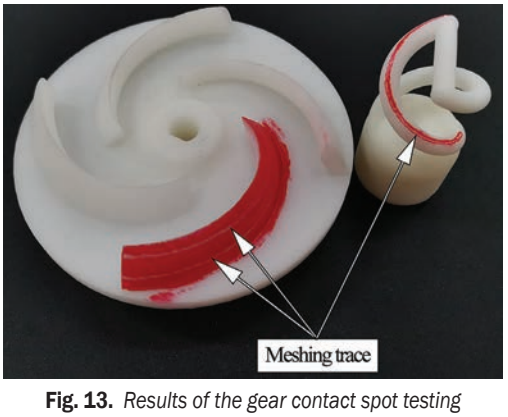

Fig. 13. *Results of the gear contact spot testing*

between two teeth. The transmission errors data analyses are tabulated as Table 1, including the peak-to-peak value, amplitude and standard deviation of the transmission error.

In the gear contact spot testing, the meshing traces appeared on both driving line gear and driven line gear after the two gears meshed. The results of the gear contact spot testing were obtained after rotating the gear pair, as shown in Fig. 13

Table 1. *Transmission errors for the kinematics experiments*

Load [N·mm]	Shaft angle [°]	Peak-to-peak value [°]	Amplitude [°]	Standard deviation [°]
0	88	0.9	0.576	0.284
	82	0.9	0.576	0.284
	76	0.9	0.576	0.286
	90 to 75	1.152	0.738	0.357
30	88	1.026	0.684	0.307
	82	1.026	0.666	0.308
	76	1.026	0.63	0.306
	90 to 75	1.296	0.792	0.385
60	88	1.206	0.684	0.358
	82	1.206	0.666	0.356
	76	1.206	0.648	0.352
	90 to 75	1.674	0.9	0.494

4 DISCUSSION

It can be seen from the kinematics experiments that VSALGM can achieve a continuous, smooth, and stable meshing transmission under the setting range of shaft angle, meaning that VSALGM has two degrees of freedom. The range of shaft angle is selected on specific requirements. In this paper, the range of the shaft angle is from θ° to ℨ , but for other designs, in practically, the range of shaft angle has different options.

It can be seen from Figs. 10 to 12 and Table 1 that the transmission error is a consistent level under different fixed shaft angles on the condition of the same load. However, the transmission error of the testing of continuously changing shaft angle is greater than the testing of fixed shaft angles; it is because of the installation error other than the shaft angle variations. According to the experiment results, the transmission error increases with the increase of the load. Due to the cantilevered teeth, the loads will cause deformations on the teeth of VSALGM, which lead to the errors of the real meshing contact curves and cause the transmission error. Therefore, VSALGM can only conduct transmission under small loads.

The transmission error of VSALGM in the kinematics experiments is mainly due to the errors of the instrument and the test prototypes, which includes the encoder error, the motor vibration error, the gears installation error and the test prototypes error. The different sources of error were analysed for VSALGM. Theoretically, the gear installation error of VSALGM includes axial error and eccentricity error; it mainly depends on the accuracy of the test rig. For the test rig in Fig. 8 the tolerance of the manufactured parts is 20 μm, the tolerance of the gear shaft is 10 μm, the tolerance of the bearing is 10 μm, and the tolerance of the positioning pin is 10 μm. A slide calliper rule with an accuracy of 20 μm was used to assist the gear installation. Therefore, the gear installation error analysis can be obtained, as shown in Fig. 14.

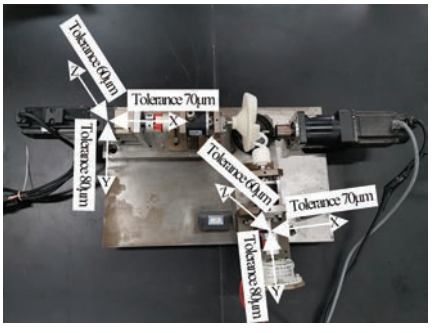

Fig. 14. *The gear installation error*

As shown in Fig. 14, for the gear installation error, both the axial tolerance and the eccentricity tolerance are about 140 μm. In addition, the tolerance of the line gear prototypes is 200μm, and the deformations on the teeth of VSALGM increases with the load. The accuracy of the encoder is 1.08′. The motor vibration error will cause the driving wheel to rotate reverse instantaneously with a small angle. In this paper, a reducer and an elastic coupling were used to reduce the influence of motor vibration. It is difficult to study the accuracy of the gear installation error based on the above experimental equipment. However, the experiments in this paper focus on verification of the basic theory and design method of VSALGM, which have proved that VSALGM has two degrees of freedom and maintains a smooth transmission while continuously changing the shaft angle. In the future, the precision testing bench and precision line gears will be developed to investigate the transmission error and dynamic performance for VSALGM.

For the gear contact spot testing, it can be seen from Fig. 13 that there are two different meshing traces on the driving tooth surface and only one meshing trace on the driven line gear after the gear pair meshing under the two different shaft angles. The meshing trace on the driven line gear is a cylindrical helix curve under the two different shaft angles. The gear contact spot testing proved that for VSALGM, different driving contact curves always mesh with the same driven contact curve under different shaft angle. The gear contact spot testing also proved that VSALGM belongs to point contact.

Finally, it can be seen from the kinematics experiments and the gear contact spot testing that whether it is a theoretically designed driving contact curve or a fitted driving contact curve, they all can achieve a smooth meshing transmission by meshing with the same driven contact curve.

5 CONCLUSIONS

In this paper, a line gear mechanism with two rotational degrees of freedom referred to as Variable Shaft Angle Line Gear Mechanism (VSALGM) is proposed. The main work is summarized as follows:

(1) Based on the space curve meshing theory of line gear, the basic design equations for the proposed VSALGM were established. The design criterion of pressure angle was proposed, and a parameter selection method was given.

(2) The prototypes of VSALGM were manufactured by using 3D printing. Based on the prototypes, the kinematic experiments for VSALGM were conducted under different shaft angles. The kinematic experiments results have proved that VSALGM has two degrees of freedom and maintains a smooth transmission while continuously changing the shaft angle.

(3) The gear contact spot testing were carried out, which have shown that there are different driving contact curves meshing with the same driven contact curve under different shaft angle for VSALGM.

However, many problems remain to be studied, such as the non-interference between two gears, parameters optimization, structural design, strength formula and sliding ratio for VSALGM, the efficiency and friction losses, the transmission error. More importantly, we will manufacture precision prototypes and develop a practical precision testing bench for testing the integrated performance of transmission for VSALGM in future.

6 ACKNOWLEDGEMENTS

The authors gratefully acknowledge the supports from the National Natural Science Foundation of

China [No. 51975179] , Natural Science Foundation of Guangdong Province [No. 2018A030310044] and 2019 Guangzhou technology project [No.201904010388] . It is our honour to thank the reviewers and editors for their valuable criticisms and comments.

7 NOMENCLATURES

a_0 The distance from point O_p to z axis
b_0 The distance from point O_p to x axis
m The helix radius of driven contact curve
n A pitch parameter of driven contact curve
θ_z The shaft angle of VSALGM
i The transmission ratio
t The scope parameter of helix curve
φ_a The rotation angle of driven wheel
φ_b The rotation angle of driving wheel
$\boldsymbol{\omega}_a$ The angular velocity of driven wheel
$\boldsymbol{\omega}_b$ The angular velocity of driving wheel
F The value of contact force
M_a The value of driving torque
M_μ The value of maximum friction torque of line gear
μ The static friction coefficient of line gear pair
α The pressure angle
f_b The normal vector in the coordinate system $O_b{-}x_by_bz_b$ at the meshing point
$\mathbf{v}_a$ The linear velocity of driven gear at the meshing point
$\mathbf{M_b}$ The transformation matrix from $O_b{-}x_by_bz_b$ to $O_a{-}x_ay_az_a$

8 REFERENCES

[1] Reinvee, M., Aia, S., Pääsuke, M. (2019). Ergonomic benefits of an angle grinder with rotatable main handle in a cutting task. *Human Factors*, vol. 61, no. 7, p. 1112-1124, **DOI:10.1177/0018720819827184**.

[2] Alam, W., Mehmood, A., Ali, K., Javaid, U., Alharbi, S., Iqbal, J. (2018). Nonlinear control of a flexible joint robotic manipulator with experimental validation. *Strojniški vestnik - Journal of Mechanical Engineering*, vol. 64, no. 1, p. 47-55, **DOI:10.5545/sv-jme.2017.4786**.

[3] Yadmellat, P., Shafer, A.S., Kermani, M.R. (2013). Design and development of a sin-gle-motor, two-DOF, safe manipulator. *IEEE/ASME Transactions on Mechatronic*s, vol. 19, no. 4, p. 1384-1391, **DOI:10.1109/TMECH.2013.2281598**.

[4] Jian, G., Wang, Y. , Zhang, P., Xie, Y., Zhao, J. (2020). Analysis of lubricating performance for involute spur gear under vibration. Lubri-cation Science, vol. 32, no. 7, p. 344-357, **DOI:10.1002/ls.1507**.

[5] Zhao, Y., Wei, W., Dong, X. (2008). Some problems on the 2DOF theory of gearing. *Mechanism and Machine Theory*, vol. 43, no. 8, p. 1024-1037. **DOI:10.1016/j.mechmachtheory.2007.07.002**.

[6] Chen, Y.Z., Lv, Y.L., Ding, J., Chen, Z. (2013). Fundamental design equations for space curve meshing skew gear mechanism. *Mechanism and Machine Theory*, vol. 70, p. 175-188, **DOI:10.1016/j.mechmachtheory.2013.07.004**.

[7] Chen, Y., Xiaoyong, X., Liang, L. (2009). A corrected equation of space curve meshing. *Mechanism and Machine Theory*, vol. 44, no. 7, p. 1348-1359, **DOI:10.1016/j.mechmachtheory.2008.11.001**.

[8] Litvin F.L., Demenego, A., Vecchiato, D. (2001). Formation by branches of envelope to parametric families of surfaces and curves. *Computer Methods in Applied Mechanics & Engineering*, vol. 190, no. 35-36, p. 4587-4608, **DOI:10.1016/s0045-7825(00)00334-0**.

[9] Kiekbusch, T., Sappok, D., Sauer, B., How-ard, I. (2011). Calculation of the combined torsional mesh stiffness of spur gears with two- and three-dimensional parametrical FE models. *Strojniški vestnik - Journal of Mechanical Engineering*, vol. 57, no. 11, p. 810-818, **DOI:10.5545/sv-jme.2010.248**.

[10] Guangjian, W., Lin, C., Li, Y., Shuaidong, Z. (2017). Research on the dynamic transmission error of a spur gear pair with eccentricities by finite element method. *Mechanism & Ma-chine Theory*, vol. 109, p. 1-13, **DOI:10.1016/j.mechmachtheory.2016.11.006**.

[11] Chen, Y., Hu, Y., Lyu, Y., He, G. (2020). Development of a form milling method for line gear: principle, CNC machine, cutter, and testing. *International Journal of Advanced Manufacturing Technology*, vol. 107, no. 3-4, p. 1-11, **DOI:10.1007/s00170-019-04771-2**.

[12] Chen, Y.Z., Yao, L. (2016). Design formulae for a concave convex arc line gear mechanism. *Mechanical Science*s, vol. 7, no. 2, p. 209-218, **DOI:10.5194/ms-7-209-2016**.

[13] Chen, Y., Huang, H., Lv, Y. (2016). A var-iable-ratio line gear mechanism. *Mechanism and Machine Theory*, vol. 98, p. 151-163, **DOI:10.1016/j.mechmachtheory.2015.12.005**.

[14] Chen, Y.Z., Lv, Y.L., Ding, J., Chen, Z. (2013). Fundamental design equations for space curve meshing skew gear mechanism. *Mechanism and Machine Theory*, vol. 70, p. 175-188, **DOI:10.1016/j.mechmachtheory.2013.07.004**.

[15] Marimuthu, P., Muthuveerappan, G. (2013). Influence of pressure angle on load sharing based stresses in asymmetric normal contact ratio spur gear drives. *Applied Mechanics and Materials*, vol. 465-466, p. 1229-1233, **DOI:10.4028/www.scientific.net/amm.465-466.1229**.

[16] Ding, J., Chen, Y.Z., Lv, Y.L., Song, C. (2014). Position-parameter selection criterion for a helix-curve meshing-wheel mechanism based on sliding rates. *Strojniški vestnik - Journal of Mechanical Engineering*, vol. 60, no. 9, p. 561-570, **DOI:10.5545/sv-jme.2013.1574**.

[17] Litvin, F.L., Fuentes, A., Hayasaka, K. (2006). Design, manufacture, stress analysis, and experimental tests of low-noise high endurance spiral bevel gears. *Mechanism and Machine Theory*, vol. 41, no. 1, p. 83-118, **DOI:10.1016/j.mechmachtheory.2005.03.001**.

[18] Kulkarni, N., Gautham, B.P., Zagade, P., Panchal, J., Allen, J.K., Mistree, F. (2014). Exploring the geometry and material space

in gear design. *Engineering Optimization*, vol. 47, no. 4, p. 561-577, **DOI:10.1080/0305215x.2014.908868**.

[19] Björling, M., Miettinen, J., Marklund, P., Lehtovaara, A., Larsson, R. (2015). The corre-lation between gear contact friction and ball on disc friction measurements. *Tribology International*, vol. 83, p. 114-119, **DOI:10.1016/j.triboint.2014.11.007**.

[20] Wu, X.T. (2009). *Principle of Gearing*. Jiaotong University Press, Xi'an. (in Chinese)

[21] Li, X., Sosa, M., Olofsson, U. (2015). A pin-on-disc study of the tribology characteris-tics of sintered versus standard steel gear materials. *Wear*, vol. 340-341, p. 31-40, **DOI:10.1016/j.wear.2015.01.032**.

[22] He, J., Wu, X., Cui, Y. (2004). Gearing principle and geometric design of conical in-volute gear pairs with crossed axes. *Proceedings of the Institution of Mechanical Engineers. Part C: Journal of Mechanical Engineering Science*, vol. 218, no. 12, p. 1517-1526, **DOI:10.1243/0954406042690461**.

[23] Chen, Y.Z. (2014). *Line Gear.* Science Press, Beijing. (in Chinese)

[24] Chen, Y.Z., Luo, L., Hu, Q. (2009). The contact ratio of a space-curve meshing-wheel transmission mechanism. *Journal of Mechanical Design*, vol. 131, no. 7, art. ID 074501, **DOI:10.1115/1.3116343**.

[25] Wang, G., Su, L., Zou, S. (2020). Uneven load contact dynamic modelling and trans-mission error analysis of a 2K-V reducer with eccentricity excitation. *Strojniški vestnik - Journal of Mechanical Engineering*, vol. 66, no. 2, p. 91-104, **DOI:10.5545/sv-jme.2019.6298**.

[26] Yu, L., Wang, G., Zou, S. (2018). The ex-perimental research on gear eccentricity error of backlash-compensation gear device based on transmission error. *International Journal* of *Precision Engineering and Manufacturing*, vol. 19, p. 5-12, **DOI:10.1007/s12541-018-0001-7**.

[27] Guangjian, W., Lin, C., Li, Y., Shuaidong, Z. (2017). Research on the dynamic transmis-sion error of a spur gear pair with eccentricities by finite element method. *Mechanism and Machine Theory*, vol. 109, p. 1-13, **DOI:10.1016/j.mechmachtheory.2016.11.006**.

Strojniški vestnik - Journal of Mechanical Engineering 67(2021)7-8, 363-368
DOI:10.5545/sv-jme.2021.7139
Original Scientific Paper
Received for review: 2021-02-21
Received revised form: 2021-05-11
Accepted for publication: 2021-06-21

Predictive Estimation of Sliding Bearing Load-Carrying Capacity and Tribological Durability

Myron Chernets[1] – Marek Opielak[2] – Anatolii Kornienko[1,*] – Oleg Radko[3]
[1]Aerospace Faculty, National Aviation University, Ukraine
[2]Lublin University of Technology, Poland
[3]National Defence University of Ukraine named after Ivan Cherniakhovskyi, Ukraine

A computational method is presented as a method for solving a plane contact problem of the theory of elasticity to determine the contact strength and tribological durability of sliding bearings. The effect of load and radial clearance on the initial contact pressures and their reduction due to wear is studied. The durability of the bearing is estimated. Qualitative and quantitative regularities of changes in contact parameters and durability from the factors under study are established. In particular, it has been shown that both contact angles and maximum contact pressures are approximately linearly dependent on the load, and the durability decreases nonlinearly with increasing load.
Keywords: sliding bearing, wear-contact problem, contact and tribocontact parameters, wear, durability

Highlights
- *A computational method for sliding bearings is presented.*
- *A tribokinetic wear model for sliding friction has been developed.*
- *Evaluation of contact pressures and durability has been carried out.*
- *Regularities of the influence of wear on contact characteristics and resources have been established.*

0 INTRODUCTION

The use of sliding bearings as one of the common friction units (Fig. 1) currently remains quite significant, where the use of rolling bearings is impossible or impractical. The main recommendations for their use are high load capacity, use at miniature or large shaft diameters, at significant speeds, at shock loads, small radial dimensions, low noise, damping capacity, etc. The range of their application in practice is very diverse **[1]**. They work in various conditions, not only at liquid conditions but also at boundary and dry friction in separate cases. Under certain operating conditions, special alloys can be used to make the shaft, for example **[2]**. It should be noted that the number of new types of composite materials for metal bearings is growing rapidly **[3]**. Therefore, the estimated assessment of their bearing capacity, wear, and durability at the design stage is an urgent task.

The solutions of the corresponding wear-contact problems for such sliding tribosystem are known in the literature **[4]** to **[16]**). In particular, in **[7]** and **[8]**, a model of the sliding bearing wear in conditions of boundary friction was obtained in the form of dependence of the wear rate on the dimensionless complexes of contact pressure and sliding velocity. The parameters of wear resistance in the model were determined by the calculation-experimental method on the basis of wear tests with the "cone – three balls" structure under variable contact conditions. Such a non-standard friction structure (ISO 7148-2) significantly limits the use of this wear model. Paper **[9]** presents the results of an experimental and numerical study of fibre-reinforced polymer bearings. The authors developed a two-dimensional finite-element model to study the stresses in the bearing and researched three-dimensional quasi-static and two-dimensional dynamic models. A study on the effect of the clearance on the contact stresses and kinematics of large-scale composite bearings in **[10]** was conducted experimentally, using the finite element method. The results of the wear study are not given. Paper **[11]** presents an adaptive wear-modelling method in plain bearings. Validation was done for a laminated polymeric composite bearing. A study of the effect of clearance on the wear and the evolution of contact pressure due to wear was performed. In **[12]**, the method of triboelements and the modelling of the behaviour of sliding tribosystems on the basis of Archard's law of abrasive wear with use of ANSYS are presented. Paper **[13]** aimed to study the wear of a fine elastic layer with the rigid bearing and shaft with the same method. Numerical analysis of the effect of the external load scattering and the initial radial clearance in the bearing on its wear was carried out. Paper **[14]** presents the results of a numerical simulation with the triboelement method to determine the wear of a thin elastic layer on a hard bushing of a cylindrical linear plain bearing. These works use Archard's law of wear. Methods for estimating the parameters of the

*Corr. Author's Address: National Aviation University, Lubomyr Huzar 1, 03680 Kyiv, Ukraine, anatoliykor80@gmail.com

durability model under the mechanism of high-cycle fatigue under sliding friction conditions are proposed in [15]. The results are recommended for analysing the reliability and durability of friction units of machines under fatigue wear conditions. For the numerical modelling of the wear kinetics of tribosystems, an iterative approach is presented in [16], which takes into account the discrete states and operational factors affecting wear. The wear of the tribosystem elements is calculated.

The abovementioned methods have not yet found proper practical application due to the use of a simplified Archard's law of abrasive wear assuming the wear intensity linear dependence on the contact pressure and the friction path, although this type of wear is unacceptable in sliding bearings. Today, in engineering practice and in the design calculations of sliding bearings, it is customary to use two main parameters: the average pressure p and the parameter pv. This simplification is very approximate, because the contact area characteristics depend not only on the load and the diameter of the shaft journal but also significantly on the radial clearance in the bearing and the elastic characteristics of the element materials. The last of the specified significant factors of influence are not considered in any way in the specified criteria, and the problem of predictive evaluation of sliding bearings durability at the design stage is not considered here at all. Therefore, reasonable methods for calculating bearings should be based on the contact problems of the theory of elasticity for cylindrical bodies of close radii. This study aims to use the author's generalized computational method [4] and [17] to [23] to estimate tribocontact pressures and durability when the bearing wears. This method is based on the concept [4], [17] and [18] of near-surface layers frictional-fatigue destruction of tribosystem elements in the process of sliding friction. In particular, in [17], the author presented a method of approximate solution of cylindrical sliding tribosystem consisting of elements with small non-circularity of its contours for the first time. The model of the triboprocess and the method of calculating the contact pressures were considered; in [18], a set of different contact problems is considered, taking into account wear for cylindrical tribosystems consisting of elements with non-circular contours; in [19], a cumulative analytical model of wear and durability of plain bearings is presented and schemes of plain bearings with different faceting of the shaft and the bushing are investigated; in [20], a generalized method for solving the contact problem for a cylindrical joint with complex faceting is presented. The parameters of one- and two-region contact are determined; in [21], according to the author's cumulative model of wear of plain bearings with technological ovality of adjacent parts, the accuracy of calculations of their service life was evaluated. The developed express calculation method of the tribocontact interaction of the shaft and the bushing is given; in [22], the generalized cumulative model of research of wear kinetics for the plain bearings in the case of one- and two-region contact is given. The results of solving the nonclassical contact problem and the wear contact problem are presented; in [23], the solution of the wear-contact problem for a bearing with different faceting of the shaft is given. Using the cumulative model, the influence of the faceting on the service life of the bearing at the complete one-region and mixed-region contact was investigated.

Based on the above methods of solving a complex wear-contact problem of the theory of elasticity, an easier-to-implement engineering method is presented below.

1 WEAR TRIBOKINETIC MODEL OF SLIDING FRICTION

According to [4], the materials' wear kinetics in sliding tribosystem is described by a system of ordinary differential equation:

$$\gamma_k = \frac{1}{v}\frac{\mathrm{d}h_k}{\mathrm{d}t}\Phi_k(\tau) = 1, \tag{1}$$

where h_k is the linear wear function of tribosystem elements; γ_k is the wear rate of their materials; v is the sliding speed; t is the triboprocess time; $\Phi(\tau)$ is the basic parameter of the model as the characteristic function of wear resistance of tribocouple materials; $k = 1, 2$ is the numbering of tribosystem elements.

The specific force of friction in mechanics and tribology is determined by the Amonton-Coulomb formula:

$$\tau = f\sigma_r, \tag{2}$$

where f is the sliding friction coefficient; $\sigma_r = -p(\alpha)$ is the contact stress calculated according to the methods of the elasticity theory; $p(\alpha)$ are the contact pressures.

The characteristic function $\Phi_i(\tau_i)$ of wear resistance of materials for discrete values of specific friction forces τ_i is established by the results of tribo-experimental studies according to the method [18] and [19]:

$$\Phi_i(\tau_i) = \frac{L_i}{h_i}, \tag{3}$$

where $L = vt$ is the friction path; $i = 1, 2, 3$ ... are the levels of load in the tribo-experiment.

Approximation of experimental values of wear resistance functions $\Phi_i(\tau_i)$ is carried out by the relation [18] and [19]:

$$\Phi_k(\tau) = B_k \frac{\tau_{k0}^{m_k}}{(\tau - \tau_{k0})^{m_k}}, \quad (4)$$

where B_k, m_k, τ_{k0} are the wear resistance characteristics of materials in the tribocouple.

2 FORMULATION OF A TRIBOCONTACT PROBLEM

The arrangement of the sliding bearing is presented in Fig. 1. Shaft 2 rotates at a constant angular velocity ω_2. Under the influence of the reduced external load $N = F/l$, the contact pressures $p(\alpha)$ unknown in distribution and magnitude arise in the contact area. There is the radial clearance $\varepsilon = R_1 - R_2 > 0$ in the bearing. The materials of the shaft and the bushing usually have different elastic properties and different wear resistance. The bearing elements have different wear areas: the bushing 1 in the area $2R_2\alpha_0$ and shaft 2 along the contour. The problem is solved as a plain problem of the elasticity theory, where the external load F on the shaft is related to the length of the journal l.

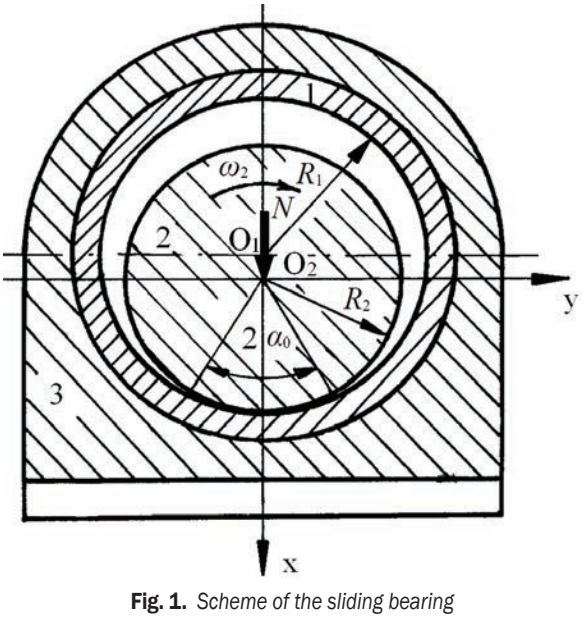

Fig. 1. *Scheme of the sliding bearing*

When solving the problem, it is necessary to determine: initial contact angle $2\alpha_0$; maximum initial contact pressures $p(0)$; tribocontact angle $2\alpha_{0h}$; maximum tribocontact pressures at wear $p(0, t, h)$; bearing durability t at the accepted elements permissible wear h_{k*}; bearing elements wear h_k during the accepted service life t_*.

According to the methods in [4], [18], and [20], the equilibrium Eq. (5) is used to determine the initial contact semi-angle α_0 under the action of the reduced load $N = F/l$, the journal radius R_2 and the radial clearance ε.

$$N = R_2 \int_{-\alpha_0}^{\alpha_0} p(\alpha)\cos\alpha\, d\alpha = 4\pi R_2 E\varepsilon \sin^2\left(\frac{\alpha_0}{4}\right), \quad (5)$$

where $E = \frac{e\cos^2(\alpha_0/4)}{R_2}$, $e = \frac{4E_1E_2}{Z}$, $0° < \alpha_0 < 90°$, $Z = (1+\kappa_1)(1+\mu_1)E_2 + (1+\kappa_2)(1+\mu_2)E_1$, $\kappa_k = 3 - 4\nu_k$, E_k, μ_k are Young's modules and Poisson's ratios of shaft 1 and bearing bushing 2 materials. Eq. (5) is solved using the method of successive approximations, by ensuring the equality of its left and right parts with the accepted accuracy. Accordingly, to determine the maximum initial contact pressures $p(0)$, which characterize the bearing load-carrying capacity, the developed method uses the formula:

$$p(0) = E\varepsilon \tan\left(\frac{\alpha_0}{2}\right). \quad (6)$$

Determining the tribocontact semi-angle α_{0h} while shaft and bearing bushing wear is carried out by a similar dependence as for the contact semi-angle α_0:

$$N = 4\pi R_2 E(\varepsilon + C_h\varepsilon_h)\sin^2\left(\frac{\alpha_{0h}}{4}\right), \quad (7)$$

where $\varepsilon_h = h_{k\,max}\left(-K_t^{(k)} + h_k'\right)$, $h_1' = h_2/h_1$, $K_t^{(1)} = 1$, $K_t^{(2)} = \alpha_0/\pi$ are the overlap coefficients; $C_h > 0$ is the wear rate indicator; h_{1*} is the permissible bushing wear:

$$h_1' = \frac{h_2}{h_1} = \frac{\Phi_1(\tau)}{\Phi_2(\tau)} = \frac{B_1\tau_{10}^{m_1}(\tau - \tau_{20})^{m_2}}{B_2\tau_{20}^{m_2}(\tau - \tau_{10})^{m_1}} K_t^{(2)},$$

$$h_2' = \frac{h_1}{h_2} = \frac{\Phi_2(\tau)}{\Phi_1(\tau)} = \frac{B_2\tau_{20}^{m_2}(\tau - \tau_{10})^{m_1}}{B_1\tau_{10}^{m_1}(\tau - \tau_{20})^{m_2}} K_t^{(1)},$$

where $\tau = fp(0) = fE\varepsilon\tan(\alpha_0/2)$ is the maximum specific friction force acting at the wear process beginning when $t = 0$; h_1, h_2 are the linear wear of bushing and shaft, respectively.

Maximum contact pressure $p(0, t, h)$ in the bearing at elements wear:

$$p(0,t,h) = p(0) + p(0,h). \quad (8)$$

The change in the maximum initial contact pressure $p(0,h)$ due to bearing elements wear is calculated as follows:

$$p(0,h) = EC_h\varepsilon_h \tan\left(\frac{\alpha_{0h}}{2}\right). \quad (9)$$

Since the bushing material is less wear-resistant than the shaft material and the bushing wears at a limited contact area, the bearing service life is determined by the bushing durability when it reaches the maximum permissible wear. According to **[4]**, **[22]**, and **[23]**, taking into account the dependences, Eqs. (1), (2), (4), (6) and (9), the bearing service life t_* is calculated by the formula:

$$t_* = \frac{-B_1\tau_{01}^{m_1}}{vC_hS_h\left(-1+h_1'\right)\left(1-m_1\right)K_t^{(1)}} \times \\ \times\left\{(S\varepsilon)^{1-m_1} - \left(S\varepsilon + C_hS_h\varepsilon_h\right)^{1-m_1}\right\}, \quad (10)$$

where $S = f\cdot p(0)/\varepsilon$, $S_h = f\cdot p(0,h)/(\varepsilon_h\cdot C_h)$, $v = \omega\cdot R_2$.

If it is necessary to estimate the shaft wear h_2 along its entire contour over time t_*, the wear is calculated as follows (after the corresponding transformation of Eq. (10)):

$$h_2 = \left|\frac{1}{C_hS_h\left(K_t^{(2)} - h_2''\right)K_t^{(2)}} \times \right. \\ \left. \times\left[\sqrt[1-m_2]{\frac{M_2(S\varepsilon)^{1-m_2} - t_*}{M_2}} - (S\varepsilon)\right]\right|, \quad (11)$$

where $M_2 = \dfrac{B_2\tau_{02}^{m_2}}{vC_hS_h(1-m_2)\left(K_t^{(2)} - h_2''\right)K_t^{(2)}}$, and

$h_2' = K_t^{(2)} / K_t^{(1)}h_1'$.

3 RESULTS OF NUMERICAL SOLUTION

Data for calculation of contact and tribocontact parameters, durability: N = 25 N, 82.5 N, 125 N, $F = Nl$; D_2 = 60 mm; $l = D_2$; ω_2 = 1 s^{-1}, 5 s^{-1}; v = 25 mm/s, 125 mm/s; ε = 0.125 mm, 0.25 mm; f = 0.05 at boundary friction; $h_{1*} = 0.5\ \varepsilon$; $C_h = 0.05$

Bushing material: teen bronze $E_1 = 1.2\cdot10^5$ MPa, $\mu_1 = 0.33$ $B_1 = 1.9\ 10^9$, $m_1 = 0.56$ $\tau_{01} = 0.1$ MPa; shaft material: hardened steel $E_2 = 2.1\cdot10^5$ MPa, $\mu_2 = 0.3$, $B_2 = 4.9\ \ 10^9$, $m_2 = 0.6$ $\tau_{02} = \tau_{01}$.

The calculation of contact semiangle α_0, maximum contact pressure $p(0)$, tribocontact semiangle α_{0h}, maximum contact pressure at wear $p(0,t,h)$, bearing service life t_* and linear shaft wear h_2 was performed according to the given flow diagram (Fig. 2).

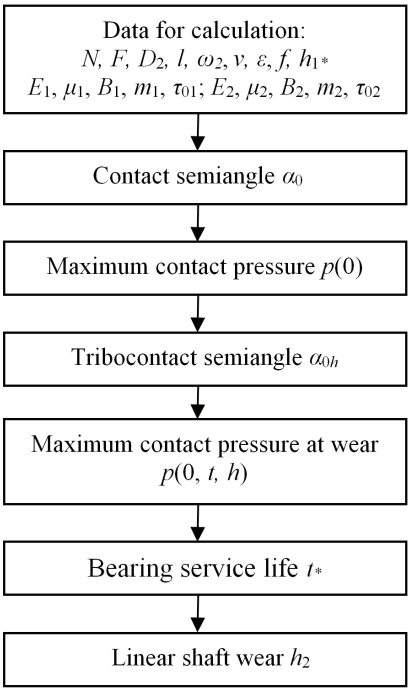

Fig. 2. *The flow diagram of calculation of contact and tribocontact parameters*

The results of solving the considered wear-contact problem are presented in Figs. 3 to 5

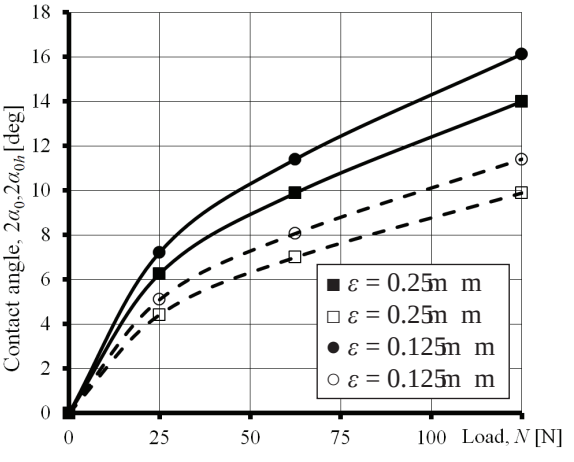

Fig. 3. *Dependences of initial contact angles on loading and their changing at wear: $2\alpha_0$ in dashed lines, and $2\alpha_{0h}$ in solid lines*

For the initial contact angle $2\alpha_0$ in the studied range of loads, there is an almost linear dependence in their increase. Naturally, with smaller radial clearances, these angles will be larger. When the accepted permissible wear is reached, the tribocontact angles $2\alpha_{0h}$ increase up to $\sqrt{2}$ times at both values of the radial clearances.

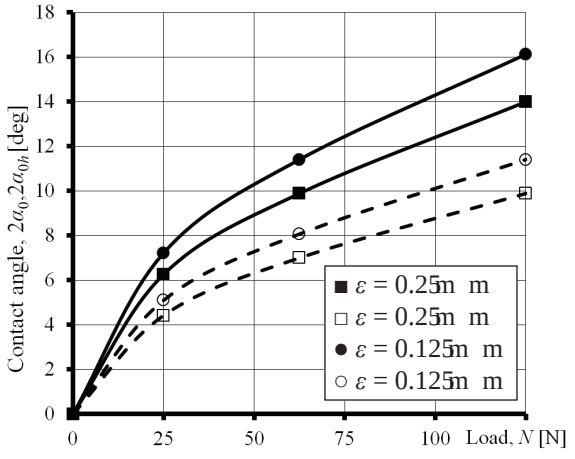

Fig. 4. *Dependences of initial contact angles on loading and their changing at wear:* $p(0)$ *in dashed lines,* $p(0,t,h)$ *in solid lines*

At relatively low loading, a nonlinear increase in the initial maximum pressures $p(0)$ is observed, and a further increase in the load leads to their linear increase. The wear of the bronze bushing contributes to a significant reduction in pressure. Tribocontact pressures $p(0,t,h)$ depend to varying degrees on radial clearance and wear.

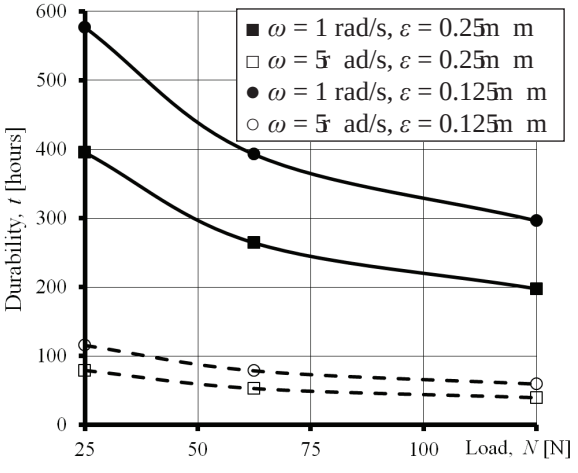

Fig. 5. *Dependence of the bearing service life on loading*

As the load increases, the bearing service life decreases nonlinearly. With a fivefold increase in angular velocity, there is a directly proportional decrease in service life.

4 CONCLUSIONS

1. The presented method of predictive estimation of sliding bearings load-carrying capacity and tribological durability allows carrying out substantiated and effective research on such basic factors of influence as external loading, shaft diameter, radial clearances, and wear.
2. An important feature of the method is the ability at the design stage to perform both the calculation of bearing service life, and the solution of inverse problem: the assessment of the bushing and shaft wear accepted service life. The solution is presented in a closed form, and this allows its implementation using the simplest software, starting from Excel (Figs. 3 to 5).
3. It should also be noted that the method (presented in Section 2) can be used without any restrictions not only for the calculation of bearings with metal elements, as presented above, but also when the friction surfaces are coated with different composition and purpose (protective, antifriction, wear-resistant) coatings.
4. On the basis of this method, it is possible to carry out the optimization on criteria of contact strength, wear resistance and durability, as well as an optimum choice of materials at the stage of the bearings designing. It is also very promising to use the method for hybrid bearings, with materials that are significantly different in their properties are used.
5. It is an advanced method for the calculation of metal-polymer bearing assemblies, because there are no calculation methods for such friction assemblies.
6. Solutions of this type of wear-contact problems can also be used to estimate the error of calculations obtained by various numerical methods (the finite element method, the boundary element method, etc.).

4 REFERENCES

[1] Lawrowski, Z. (2007). Sliding bearings. History, current state, development prospects. *Tribologia*, vol. 26, no. 6, p. 7-61.

[2] Cherepova, T., Dmitrieva, G., Tisov, O., Dukhota, O., Kindrachuk, M. (2019). Research on the properties of Co-TiC and Ni-TiC HIP-sintered alloys. *Acta Mechanica et Automatica*, vol. 13, no. 1, p. 57-67, **DOI:10.2478/ama-2019-0009**.

[3] Panarin, V. Ye., Kurdyumov, G.V., Svavil'nyy, M. Ye., Khominych, A.I., Kindrachuk, M.V., Kornienko, A.O. (2017). Creation of a diffusion barrier at the interphase surface of composite coatings reinforced with carbon nanotubes. *Journal of Nano- and Electronic Physics*, vol. 9, p. 06023-1–06023-5, **DOI:10.21272/jnep.9(6).06023**.

[4] Andreikiv, A.E., Chernets, M.V. (1991). *Evaluation of the Contact Interaction of Rubbing Machine Elements*. Naukova Dumka, Kiev.

[5] Kuzmenko, A.G. (2010). *Development of Methods of Contact Tribomechanics*. KhNU, Khmelnytsky.

[6] Zwieżycki, W. (1999). *Predicting the Reliability of Wearing Machine Elements*. Institute for Sustainable Technologies, Radom.

[7] Dykha, A., Sorokatyi, R., Makovkin, O., Babak, O. (2017). Calculation-experimental modeling of wear of cylindrical sliding bearings. *Eastern-European Journal of Enterprise Technologies*, vol. 5, no. 1, p. 51-59, **DOI:10.15587/1729-4061.2017.109638**.

[8] Dykha, A., Marchenko, D. (2018). Prediction the wear of sliding bearings. *International Journal of Engineering & Technology*, vol. 7, no. 2.23, p. 4-8, **DOI:10.14419/ijet.v7i2.23.11872**.

[9] Rezaei, A., Ost, W., Van Paepegem, W., De Baets, P., Degrieck, J. (2011). Experimental study and numerical simulation of the large-scale testing of polymeric composite journal bearings: Three-dimensional and dynamic modelling. *Wear*, vol. 270, no. 7-8, p. 431-438, **DOI:10.1016/j.wear.2010.11.005**.

[10] Rezaei, A., Ost, W., Van Paepegem, W., De Baets, P., Degrieck, J. (2012). A study on the effect of the clearance on the contact stresses and kinematics of polymeric composite journal bearings under reciprocating sliding conditions. *Tribology International*, vol. 48, p. 8-14, **DOI:10.1016/j.triboint.2011.06.031**.

[11] Rezaei, A., Van Paepegem, W., De Baets, P., Ost, W., Degrieck, J. (2012). Adaptive finite element simulation of wear evolution in radial sliding bearing. *Wear*, vol. 296, no. 1-2, p. 660-671, **DOI:10.1016/j.wear.2012.08.013**.

[12] Sorokatyi, R.V. (2002). Modeling the behavior of tribosystems using the method of triboelements. *Journal of Friction and Wear*, vol. 23, no. 1, p. 16-22.

[13] Sorokatyi, R.V. (2003). Solution of the problem of wear of a fine elastic layer with a rigid bearing mounted on a rigid shaft using the method of triboelements. *Journal of Friction and Wear*, vol. 24, no. 1, p. 35-41.

[14] Sorokatyi, R.V. (2003). Evaluation of efficiency of sliding bearings during reciprocation. *Journal of Friction and Wear*, vol. 24, no. 2, p. 136-143.

[15] Sorokatyi, R., Chernets, M., Dykha, A., Mikosyanchyk, O. (2019). Phenomenological model of accumulation of fatigue tribological damage in the surface layer of materials. *Mechanisms and Machine Science*, vol. 73, p. 3761-3769, **DOI:10.1007/978-3-030-20131-9_371**.

[16] Dykha, A., Sorokatyi, R., Pasichnyk, O., Yaroshenko, P., Skrypnyk, T. (2020). Machine wear calculation module in computer-aided design systems. *IOP Conference Series Materials Science and Engineering*, vol. 1001, art. ID 012040, **DOI:10.1088/1757-899X/1001/1/012040**.

[17] Chernets, M.V. (1996). On the issue of assessing the durability of cylindrical sliding tribosystems with boundaries close to circular. *Friction and Wear*, no. 3, p. 340-344.

[18] Chernets, M.V. (2009). *Contact Problems for Cylindrical Systems with Low Angularity of Contours When Worn*. Drohobycz State Pedagogical University, Lviv.

[19] Chernets', M.V., Andreikiv, O.E., Liebiedieva, N.M., Zhydyk, V.B. (2009). A model for evaluation of wear and durability of plain bearing with small non-circularity of its contours. *Materials Science*, vol. 2, p. 279-290, **DOI:10.1007/s11003-009-9176-5**.

[20] Chernets', M.V. (2009). Contact problem for a cylindrical joint with technological faceting of the contours of its parts. Materials Science, vol 45, p. 859-868, **DOI10.1007/s11003-010-9252-x**.

[21] Chernets', M.V., Zhydyk, V.B., Chernets', Yu.M. (2014). Accuracy of evaluation of the service life of a plain bearing according to the generalized cumulative model of wear. *Materials Science*, vol. 50, p. 39-45, **DOI:10.1007/s11003-014-9689-4**.

[22] Chernets, M., Chernets, Ju. (2015). Generalized method for calculating the durability of sliding bearings with technological out-of-roundness of details. *Proceedings of the Institution of Mechanical Engineers, Part J: Journal of Engineering Tribology*, vol. 229, no. 2, p. 216-226, **DOI:10.1177/1350650114554242**.

[23] Chernets, M.V. (2015). Prediction of the life of a sliding bearing based on a cumulative wear model taking into account the lobing of the shaft contour. *Journal of Friction and Wear*, vol. 36, p. 163-169, **DOI:10.3103/S1068366615020038**.

Strojniški vestnik - Journal of Mechanical Engineering 67(2021)7-8, 369-379
DOI:10.5545/sv-jme.2021.7156
Original Scientific Paper
Received for review: 2021-03-09
Received revised form: 2021-05-18
Accepted for publication: 2021-06-28

Experimental Investigation and Mathematical Modelling of Heat Transfer Coefficient in Double Slope Solar Still

Raj Vardhan Patel[1,2] – Anshul Yadav[1,2] – Jerzy Winczek[3]*
[1]Kamla Nehru Institute of Technology, India
[2]CSIR-Central Salt and Marine Chemicals Research Institute, India
[3]Czestochowa University of Technology, Poland

In this study, a double slope solar still has been designed and fabricated with the help of locally available materials for the climatic condition of Sultanpur, India. The experimental study was performed to investigate the effect of basin water, wind velocity on the heat transfer coefficient (convective, evaporative, and radiative) and yield of solar still. A mathematical model is developed to understand the impact of wind velocity and basin water depth in the double slope solar still on the heat transfer coefficient. It was found that the convective heat transfer coefficient depends upon the water mass and the temperature of basin mass, and glass cover temperature. The maximum value of h_{ew} (55.05 W/(m²K) and 31.80 W/(m²K)) and h_{cw}, (2.48 W/(m²K) and 2.38 W/(m²K)) found for depths of 2 cm and 5 cm, respectively. The radiative heat transfer coefficient found to be a maximum of 8.31 W/(m²K) for 2 cm depth, and it increases as the condensation increases, because the glass surface temperature increases as vapour transfers its energy to the surface. On increasing the depth from 2 cm to 5 cm, the yield from the solar still decreases by 25.45 %. The maximum yield of 2.5 l/m²/day was found for a 2 cm water depth. The theoretical and experimental yield agreed with an error of 7.5 %, 3.25 %, 7.4 %, and 8.4 % for water depths of 2 cm, 3 cm, 4 cm, and 5 cm, respectively. It was also found that the yield from the solar still increases as the wind speed increase because this leads the faster condensation at the glass surface.
Keywords: double slope solar still; solar energy; distillation; heat transfer coefficient

Highlights
- *A mathematical model is developed to find the yield and heat transfer coefficient for double slope solar still with the experimental findings on the yield and heat transfer coefficient.*
- *Convective and evaporative heat transfers were the most critical parameters for a solar distillation unit.*
- *The radiative heat transfer coefficient increases as the condensation increase because, due to condensation, the glass surface temperature increases as vapour transfers its energy to the glass surface.*
- *The yield from the still increases as the basin water depth decreases. The evening time production is higher for higher basin mass because of the heat-storing capacity of basin mass.*
- *The yield of solar still increases as the wind speed increases because this leads to higher condensation on the glass surface.*

0 INTRODUCTION

Currently, energy and fresh water supplies are major challenges in remote areas. Only 1 % of the total water available on the earth can be used for drinking. Current distillation methods use conventional fuel, which are a limited resource, and there is environmental pollution when such fuels are used to generate power. Solar stills are simple devices that can be used to produce potable water. They can be an effective solution for providing potable water in remote areas **[1]** and **[2]**.

Solar stills are generally classified into two categories: active and passive **[3]** and **[4]**. Solar stills require only solar energy for their operation, which is freely available and eco-friendly, and work on the simple principle of evaporation and condensation. Solar distillation removes salts and other impurities **[5]** and **[6]**. It is used to produce potable or pure water for hospitals, laboratories, and commercial products **[7]** and **[8]**.

The yield of a conventional solar still depends on the water mass in the basin. The effect of that water mass on the solar heat transfer still has been investigated by various researchers **[9]** to **[11]**. The studies concluded that as the mass of basin water increases, the yield from the system decreases. Dev et al. **[9]** investigated the inverted absorber single slope solar still, and found higher production of freshwater with 1 cm depth compared to 2 cm and 3 cm depths. Phadatare and Verma **[10]** studied water depth on the internal heat and mass transfer in the single-basin double-slope solar still (DSSS). Tripathi and Tiwari **[11]** concluded that the yield from the system decreases as the mass of basin water increases. The experimental and analytical study performed by Feilizadeh et al. **[12]** reported that the production from the solar still increases as the water depth and distance between the water basin and the condensing cover is lower.

The radiative and convective heat transfer decrease as the water mass in the basin increases.

*Corr. Author's Address: Czestochowa University of Technology, 42201 Czestochowa, Poland, winczek@gmail.com

The influence of wind on the production of solar stills was investigated by El-Sebaii [13] and [14], who determined that the increase in wind speed up to a critical value increases the yield of still. Higher wind speed decreases the yield because it decreases the basin temperature. An experiment conducted by Danish et al. [15] to enhance the performance of the solar still by using a vacuum pump and geothermal energy found that the increases in wind speed have a detrimental effect on the yield of solar still, because the increase in speed increases the heat loss from the basin water.

The production rate of solar stills is low; therefore, they cannot be used as a conventional water purifier. The yield from a solar desalination unit increased by incorporating phase change materials (PCM) [16] and [17] and nanofluids [18] and [19] to the basin water. Mathematical modelling has been as subject of some interest as it can optimize the efficiency and production by changing the different operational and geometrical parameters without losing its inherent feature of low cost; the main advantage associated with modelling analysis that much effort and cost can be minimized for carried out the experimentation [20] and [21]. Rahbar and Esfahani [22] proposed a numerical correlation to determine the productivity of a solar still by assuming the fixed water depth and glass temperature. The trends of water production are similar to the convective heat transfer coefficients. Madhlopa [23] modelled the radiative heat transfer inside a solar still with and without considering the view factor, and the numerical model with view factor involving provides better yield. Keshtkar et al. [24] proposed a novel transient model to calculate transient temperature and concentration distribution and also production from a solar still without specifying the water and glass surface temperatures as the boundary condition.

The production of a solar still is dependent on the rate of heat transfer in the solar still, basin water, and wind velocity (which provides glass cover cooling), and similar factors. The present study focuses on studying the variation of the heat transfer coefficient with basin water temperature and wind velocity for the acrylic solar still for the summer climatic condition of Sultanpur, India. The different heat transfer coefficient associated with DSSS is compared for different water depths, and the comparisons have been made for the orientations (i.e., east and west sides).

1 EXPERIMENTS

1.1 Solar Distillation Unit

The schematic diagram and the experimental setup of the DSSS are shown in Figs. 1 and 2, respectively. A passive DSSS is designed and fabricated to investigate the effect of climatic and operational parameters on a solar still for the summer climatic condition of Sultanpur (latitude: 26.26° N and longitude: 82.07° E) Uttar Pradesh, India. The basin of the solar still is fabricated frin a black acrylic sheet of a thickness of 4 mm. The basin size of the still is 1 m × 1 m × 0.1 m. Plywood of 12 mm thickness is used for support and insulation of solar still basin in order to reduce the heat transfer from the bottom and side of solar still basin. The acrylic material has been selected due to its low thermal conductivity and high water-resistant nature. The still is designed for the maximum water depth of 10 cm. Glass of 3.5 mm thickness used as the condensing cover, which is inclined at an angle of 30° . The condensing cover inclination is equal to the latitude of Sultanpur to receive maximum radiation from the sun. The basin of the still is painted black to enhance the capacity of the basin to receive the maximum solar radiation. A V-shaped trough of length 1.02 m is provided below the condensing cover to collect the condensed water from the glass surface. M-seal and putty were used to make still airtight and prevent water leakage.

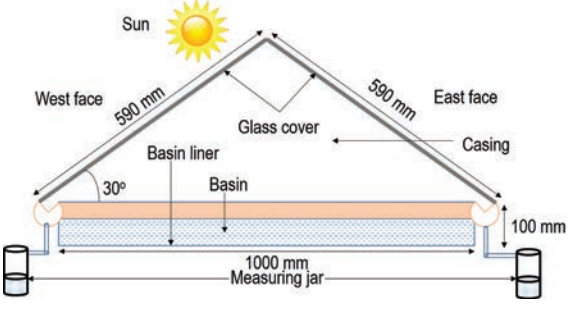

Fig. 1. *A schematic diagram of solar still*

1.2 Experimental Measurements

The experiments were performed in March and April 2016 The solar still was placed in the east-west orientation for the experiments. Seven digital temperature sensors were used to record the temperature reading at the different locations of solar still. Global solar radiation, ambient temperature, and wind speed data were taken from the solar radiation

resource assessment (SRRA) station installed at the KNIT, Sultanpur, India. A digital anemometer was used for measuring the wind velocity. The temperature readings were recorded at a one-hour interval. The experiments were carried out for different water depths, of which 2 cm, 3 cm, 4 cm, and 5 cm are presented in this study.

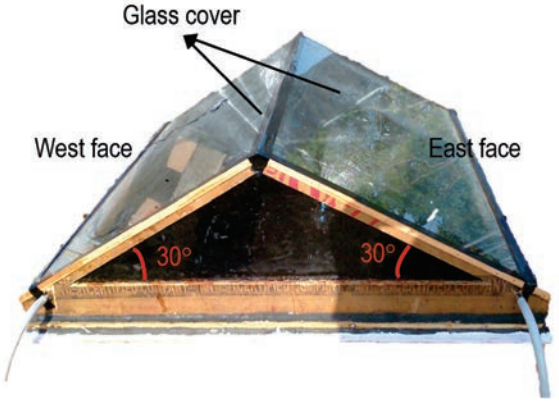

Fig. 2. *Experimental setup of solar still*

1.3 Error Analysis of Experimental Measurements

The errors associated with the different measuring instruments (solarimeter, digital thermometer, digital anemometer, and measuring jar) have been calculated based on the least count and the least value measured from that instrument during the experimentation. The minimum error is the ratio of the least value that an instrument can measure to the least value measured from that instrument. Table 1 shows the error percentages associated with the different measuring instruments.

Table 1. *List of measuring devices and their accuracy and error*

Instrument	Range	Accuracy	Error [%]
Solarimeter	0 W/m² to 2500 W/m²	±1 W/m²	0.707
Thermometer	–50 °C to 150 °C	±0.1 °C	0.37
Anemometer	0 m/s to 15 m/s	±0.1 m/s	9.17
Measuring jar	0 ml to 1500 ml	±1 ml	10

2 THERMAL CALCULATION FOR THE MODEL

2.1 Mathematical Model for Heat Transfer in Solar Still

The heat transfer can be classified into two categories: internal and external heat transfer in a solar distillation system. The different heat interactions in the solar distillation unit are explained below.

2.1.1 Internal Heat Transfer

The internal heat transfer is the heat transfer between basin water and glass cover by convection, evaporation, and radiation.

2.1.2 Convective Heat Transfer

The heat transfer is taking place across the air, which is inside the solar still. As the system is airtight, there is no external velocity provided to the inside air to cause heat transfer. The air is humid because of vapour evaporating from the water surface; the heat transfer is due to the buoyancy only, meaning that free convection heat transfer occurs inside the still casing. The rate of convective heat transfer ($\dot{q}_{cw}$) from the water surface to condensing glass cover is given by:

$$\dot{q}_{cw} = h_{cw}\left(T_w - T_g\right). \tag{1}$$

The convective heat transfer coefficient depends on the operating temperature range of still and physical properties of the fluid at this operating temperature, condensing cover geometry and flow characteristics of the fluid. Dunkle [25] developed an equation for evaluation of the internal heat transfer coefficient:

$$h_{cw} = 0.0884(\Delta T^*)^{\frac{1}{3}}, \tag{2}$$

where $\Delta T^* = \left[\left(T_w - T_g\right) + \dfrac{\left(P_w - P_g\right)\left(T_w + 273.15\right)}{268.9\times10^3 - P_w}\right]$.

2.1.3 Evaporative Heat Transfers

The evaporative heat transfer occurs between the water surface and the inner glass surface of the DSSS.

The rate of evaporative heat transfer ($\dot{q}_{ew}$) from the water surface to glass cover surface is given by:

$$\dot{q}_{ew} = h_{ew}\left(T_w - T_g\right), \tag{3}$$

and the evaporative heat transfer from the water surface to the glass surface is given by:

$$\dot{q}_{ew} = 0.0162\times h_{cw}\left(P_w - P_g\right). \tag{4}$$

The above equation can be rearranged as:

$$\dot{q}_{ew} = 16.273\times10^{-3} h_{cw}\frac{\left(P_w - P_g\right)}{\left(T_w - T_g\right)}\left(T_w - T_g\right), \tag{5}$$

where $h_{ew} = 16.273\times10^{-3} h_{cw}\dfrac{\left(P_w - P_g\right)}{\left(T_w - T_g\right)}$,

where P_w and P_g are partial saturation pressures [W/m²] and given by [26]:

$$P_g = \exp\left[25.317 - \frac{5144}{T_{gi} + 273.15}\right], \quad (6)$$

$$P_w = \exp\left[25.317 - \frac{5144}{T_w + 273.15}\right]. \quad (7)$$

2.1.4 Radiative Heat Transfer Coefficient

The rate of radiative heat transfer ($\dot{q}_{rw}$) from the water surface to glass cover for these infinite parallel surfaces is given by:

$$\dot{q}_{rw} = \varepsilon_{eff}\sigma\left[\left(T_w + 273.15\right)^4 - \left(T_g + 273.15\right)^4\right]. \quad (8)$$

The rate of radiative heat transfer is also given by:

$$\dot{q}_{rw} = h_{rw}\left(T_w - T_g\right). \quad (9)$$

The (h_{rw}) is the radiative heat transfer coefficient from the water surface to the glass cover and is given by (by comparing Eqs. (8) and (9)):

$$h_{rw} = \varepsilon_{eff}\sigma\left[\left(T_w + 273.15\right)^2 + \left(T_g + 273.15\right)^2\right] \times\left[T_w + T_g + 546.30\right]. \quad (10)$$

where e_{ff} is effective emissivity of water and glass surface, σ Stefan-Boltzmann constant (5.6 10^{-8} W/(m²K⁴)).

2.1.5 External Heat Transfers

The external heat transfer is primarily governed by conduction, convection, and radiation process, which are independent of each other. These heat transfers occur outside the solar distiller, from the glass cover and the bottom and side insulation.

2.1.6 Top Loss Coefficient

Due to the small thickness of the glass cover, the temperature of the glass may be assumed to be uniform. The external rate of heat transfer radiation ($\dot{q}_{rg}$), convection ($\dot{q}_{cg}$) and total heat ($\dot{q}_{tg}$) losses from the glass to the ambient surroundings are expressed as:

$$\dot{q}_{tg} = \dot{q}_{rg} + \dot{q}_{cg}, \quad (11)$$

$$\dot{q}_{rg} = \sigma\varepsilon_g\left[\left(T_g + 273.15\right)^4 - \left(T_{sky} + 273.15\right)^4\right], \quad (12)$$

$$\dot{q}_{rg} = h_{rg}\left(T_g - T_a\right). \quad (13)$$

Comparing the above Eqs. (12) and (13), we obtain:

$$h_{rg} = \frac{\varepsilon_g\sigma\left[\left(T_g + 273.15\right)^4 - \left(T_{sky} + 273.15\right)^4\right]}{\left(T_g - T_a\right)}, \quad (14)$$

where $T_{sky} = T_a - 6$ [27], ε_g emissivity of the glass surface. The ambient emissivity is assumed to be 1, as it behaves as a black body [8]. (In case of clear and cloudy sky, the difference between ambient temperature and effective sky temperature was assumed to be 6 °C) and the rate of convective heat transfer from the glass surface to ambient is given by:

$$\dot{q}_{cg} = h_{cg}\left(T_g - T_a\right). \quad (15)$$

On substituting the value of ($\dot{q}_{rg}$) and ($\dot{q}_{cg}$) in Eq. (11), we obtain:

$$\dot{q}_{tg} = h_{tg}\left(T_g - T_a\right), \quad (16)$$

where $h_{tg} = h_{rg} + h_{cg}$.

The expression for (h_{tg}) and (h_{cg}) is given by Watmuff and Charters [27]:

$$h_{tg} = 5.7 + 3.8\ V, \quad (17)$$

$$h_{cg} = 2.8 + 3\,V, \quad (18)$$

where V is wind velocity [m/s], h_{tg} is, h_{rg} and h_{cg} total, radiative, and convective heat transfer coefficient [W/m²] from the top glass surface, respectively.

2.1.7 Bottom and Side Loss Coefficient

Heat is also lost from the water in the basin to the ambient through the insulation, subsequently by convection and radiation from the bottom or side surface of the basin. The bottom loss coefficient (U_b) can be written as:

$$U_b = \left[\frac{1}{h_w} + \frac{1}{h_b}\right]^{-1}. \quad (19)$$

The side loss coefficient (U_e) can be expressed as:

$$U_e = \frac{U_b A_{SS}}{A_S}, \quad (20)$$

where A_S is a sidewall surface area [m²] in contact with basin water and A_S area of the basin of the distiller [m²]. A_S is very small in comparison to A_S, for small water depth. Therefore, it can be neglected.

The rate of heat loss per m² from the basin liner to ambient can be written as:

$$\dot{q} = h_b \left(T_w - T_a\right), \tag{21}$$

where $h_b = \left[\frac{t_i}{K_i} + \frac{1}{h_{cb} + h_{rb}}\right]^{-1}$, where h_w and h_b are convective and overall heat transfer coefficient from basin liner to ambient through the bottom, t_i thickness, K_i thermal conductivity of the insulation material at the bottom, h_{cb} and h_{rb} convective and radiative heat transfer coefficient basin liner to ambient through the bottom.

2.1.8 Determination of Distillate Output

The hourly distillate output per m² from the solar still can be obtained as:

$$m_{ew} = \frac{\dot{q}_{ew}}{L} 3600, \text{ or } m_{ew} = \frac{h_{ew}\left(T_w - T_g\right)}{L} 3600, \tag{22}$$

where L is latent heat of vaporization [J/kg] for less than 0°C and given by [27]:

$$L = 2.4935 \times 10^6 \left[1 - 9.4779 \times 10^{-4} T + 1.3132 \times 10^{-7} T^2 - 4.7974 \times 10^{-9} T^3\right],$$

where temperatures are in °C and heat transfer coefficients are in W/(m²K). The heat transfers rate presented in the thermal modelling are in W/m². The subscripts *w*, *g*, *a*, and *i* indicate the basin water, glass surface, ambient and insulation respectively.

3 RESULTS AND DISCUSSIONS

The present experimental work has been carried out for heat transfer analysis of the east-west orientation of DSSS for various basin water depths (2 cm, 3 cm, 4 cm and 5 cm). The east-west orientation has been chosen because the still gives maximum yield for this orientation. The experimental measurements were recorded and accurately from 8 00 h to 17 00 h. The mathematical equations which are used in the thermal model have solved analytically. As the difference between basin water and glass cover increases, the rate of heat transfer, as well as the production from the DSSS increases.

3.1 Variation of Basin Water Temperature with Basin Water Depth

In Fig. 3 the variation of basin water temperature with the depth of basin water and wind velocity are represented. It can be seen that the basin water temperature for 2 cm water depth is higher compared to 3 cm, 4 cm, and 5 cm water depths. This is because the basin water with 3 cm, 4 cm and 5 cm depths have high thermal inertia compared to 2 cm water depth. Therefore, the basin filled with 2 cm water depth will be heated faster than other water depths. During the experiments, it was found that the

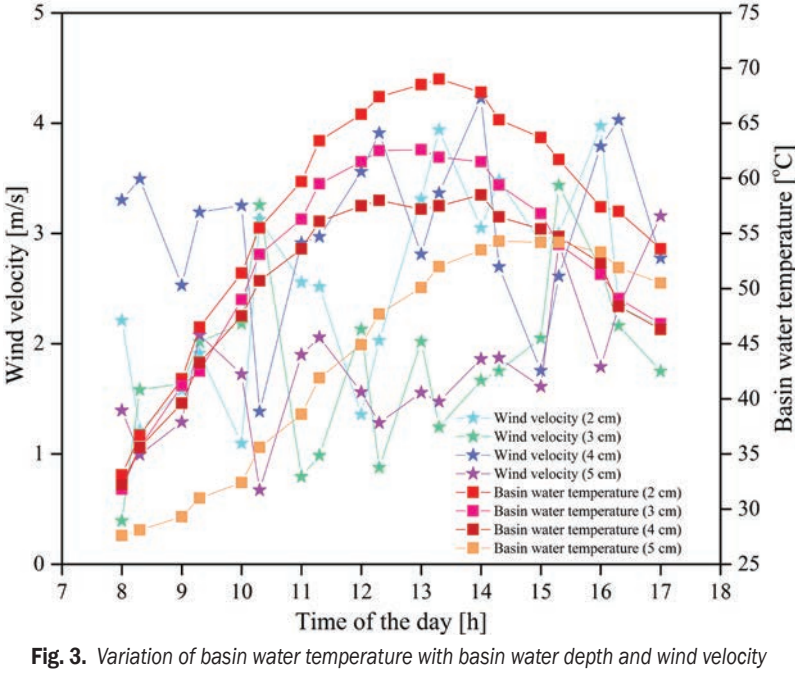

Fig. 3. *Variation of basin water temperature with basin water depth and wind velocity*

maximum temperature for 2 cm, 3 cm, 4 cm, and 5 cm depths are 60 °C, 62.6 °C, 65 °C, and 64 °C, respectively, between 13:00 h and 14:30 h. The peak starts shifted towards the right side as basin water depth increases from 2 cm to 5 cm. This is because 5 cm water depth requires more time to be heated, due to the higher mass present in the basin. The basin water temperature was found to be maximum for 2 cm depth. The temperature decrease for 2 cm water depth was higher than other higher water depth after 14:00 h because of lower heat storage capacity. During the experimentation, the average wind velocity was found to vary between 2 m/s to 3 m/s.

3.2 Variation of Heat Transfer Coefficients with Basin Water Depth

Figs. 4 to 6 show the variation of heat transfer coefficients (convective, evaporative, and radiative, respectively) for DSSS for the east and west glass. The curves are drawn for the positive value of temperature difference between basin water and glass cover surface (δT). The yield from the solar still increases either increase in evaporation temperature or decrease in condensing surface temperature. In both cases, the (δT) increases and the heat transfer rate increases.

Fig. 4 shows the variation of the convective heat transfer coefficient obtained from Eq. (2). The convective heat transfer rate is strongly dependent on the temperature difference between the water and glass cover surface. Fig. 4 shows that the average heat transfer coefficient for 2 cm water depth is maximum because of the higher temperature difference than higher water depths. This is because the lesser mass present in the basin with 2 cm depth requires less time to be heated. The maximum value of h_{cw} were 2.8 W/(m²K), 2.25 W/(m²K), 2.21 W/(m²K), and 2.8 W/(m²K) for 2 cm, 3 cm, 4 cm, and 5 cm depths, respectively. The heat transfer coefficients are higher than the results obtained in the experimental studies by Shukla and Rai [28]. The maximum heat transfer occurs around 13:00 to 14:00 h, while in the case with 5 cm depth, the maximum value of h_{cw} occurs at 16:00 h. This is because of the higher wind speed, which leads to faster cooling of the glass. Thus, the heat transfer of convection increases. The heat transfer coefficient is lower for 2 cm depth compared to 5 cm depth after 16:00 h. This is because of the higher thermal storage capacity of 5 cm water depth, which leads to higher basin water temperature.

Fig. 5 shows the variation of the evaporative heat transfer coefficient (calculated from Eq. (5)) with basin water depth for the experimental setup. It can be observed from Fig. 5 that the h_{ew} is high for west glass because there is no direct sun heating of it in the morning, but as the evaporation starts and vapour start condensing on the west glass surface, the heat released during condensation heated the glass surface which leads the increase in the surface temperature of the glass. Thus, as the process continued, the temperature of west glass approaches saturation temperature, and due to this, condensation starts decreasing after 13:00 h, 13:30 h and 14:00 h, and 14:30 h for 2 cm, 3 cm, 4 cm, and 5 cm water depths.

It is seen that from Figs. 4 and 5 that in the morning for 2 cm water depth, the rate of h_{cw} and h_{ew} is maximum for the west glass because basin water, as well as the east glass, is heated; therefore, the δT is higher for the west glass as compared to the east glass. After 13:00 h, the variation becomes closer for east and west glass because solar radiation does not directly fall on one glass only. This is also due to the higher basin water temperature as it absorbs solar energy since morning. However, in the case of higher water depths (i.e., 3 cm, 4 cm, and 5 cm), the east and west variation is almost eliminated because of the heating due to solar radiation and cooling due to wind. While 2 cm depth variation of heat transfer is faster than other depths, the wind velocity is higher with the 5 cm water depth; this is because of higher thermal energy storing capacity with the 5 cm depth consequent the slower cooling of the basin water. The h_{cw} of east and west surfaces for the present solar still is higher for the period of 15:00 to 17:00, compared to Shukla and Rai [28]. This is because of the higher basin temperature and low thermal conductivity of acrylic material of solar still, which reduces the heat loss of the basin water.

The average evaporative heat transfers were higher for 2 cm depth than other water depths (3 cm, 4 cm, and 5 cm). Therefore, the yield in the case of 2 cm water depth is maximum as the evaporation rate is the main driving parameter for the production from the solar still. From Fig. 5, the h_{ew} starts decreasing at a faster rate for 2 cm depth compared to other water depths. This is not only because of low heat-storing capacity for 2 cm water depth but also because of the lower heating rate for the other higher depths; thus, from the evening, the production rate starts decreasing faster for lower and nocturnal production is more for higher depths.

The maximum value of h_{ew} is found to be 5.05 W/(m²K), 4.23 W/(m²K), 3.25 W/(m²K) and 3.0 W/(m²K) for 2 cm, 3 cm, 4 cm and 5 cm water depths. The peak of h_{ew} shifted to the right as the mass in the basin starts increasing; this is due

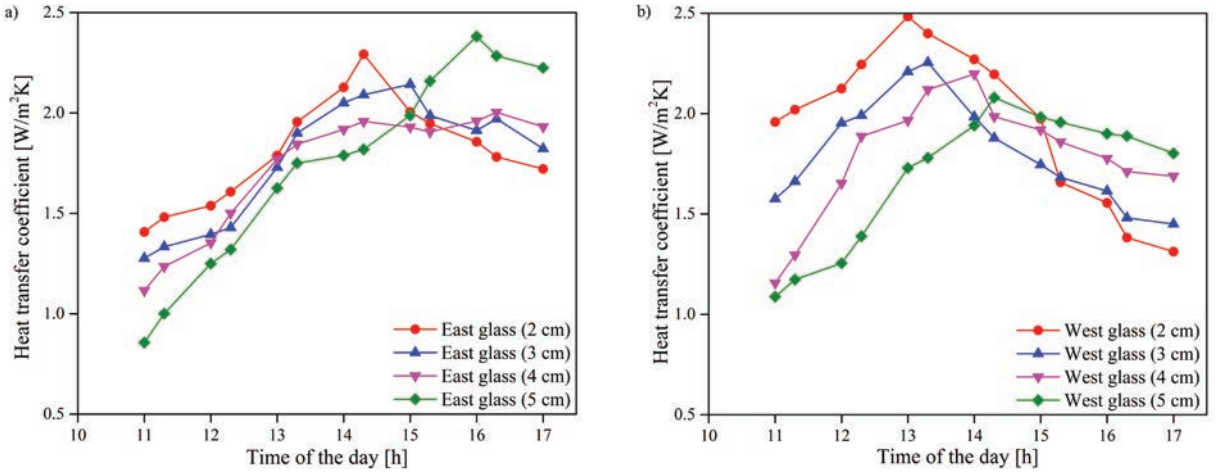

Fig. 4. *Variation of the convective heat transfer coefficient with basin water depth for: a) east glass, and b) west glass*

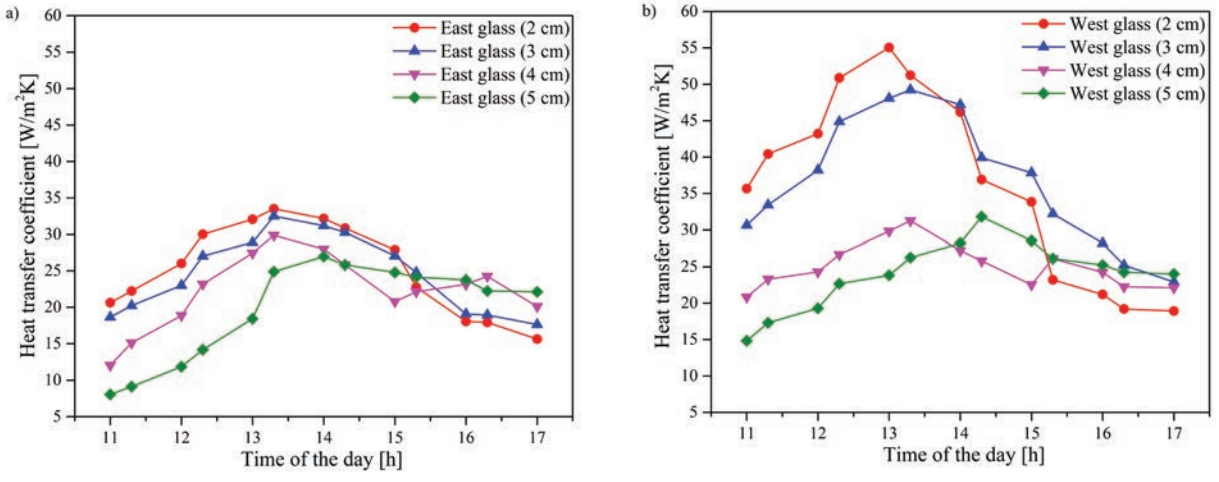

Fig. 5. *Variation of evaporative heat transfer coefficient with basin water depth for a) east glass b) west glass*

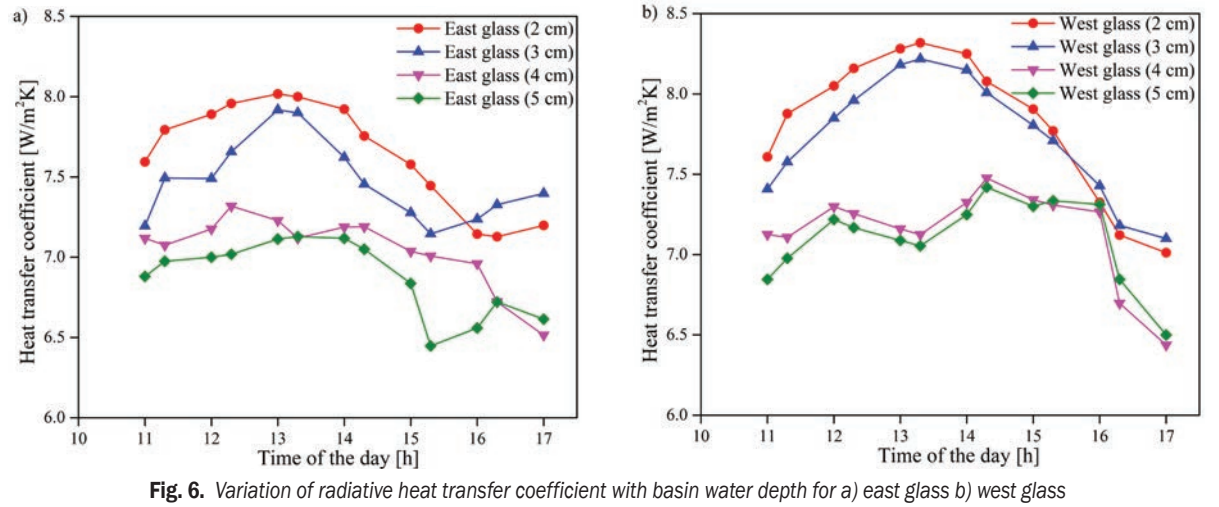

Fig. 6. *Variation of radiative heat transfer coefficient with basin water depth for a) east glass b) west glass*

to lower thermal inertia for 2 cm depths compared to others depth. The maximum value of h_{cw} and h_{ew} are found to be 2.8 W/(m²K) and 5.05 W/(m²K) for the west glass, respectively, for 2 cm depth.

There are some fluctuations in heat transfer because of uncontrolled wind speed over the DSSS glass surfaces. From Fig. 5 it can be seen that the heat transfer coefficient increases for higher water depths. This is due to an increase in wind speed which leads to better evaporation as well as condensation. When the results are compared with those of Shukla and Rai [28], the maximum and average evaporative heat transfer coefficients are found to be higher in this study. This is due to the higher temperature difference obtained with the present experimental setup. This higher temperature difference is because of higher basin temperature also due to the insulating nature of acrylic.

Fig. 6 shows the variation of radiation heat transfer's coefficient (calculated from Eq. (38)) for 2 cm, 3 cm, 4 cm and 5 cm water depth a for the experimental setup for the east and west glass of DSSS. The radiation heat transfer mainly depends on the basin water and glass surface temperature and the emissivity of basin water and glass surface. As the evaporation increases, the surface temperature of the glass surface increases due to the condensation of vapour on the glass surface. Therefore, the radiation heat transfer coefficient increases. The maximum heat transfer coefficients are found to be 8.2 W/(m²K), 8.21 W/(m²K), 7.4 W/(m²K) and 7.4 W/(m²K) for 2 cm, 3 cm, 4 cm and 5 cm water depths, respectively. Shukla and Rai [28] showed a lower radiative heat transfer coefficient than the present study did. This is because of the higher evaporation and condensation associated with the design of DSSS. In the present

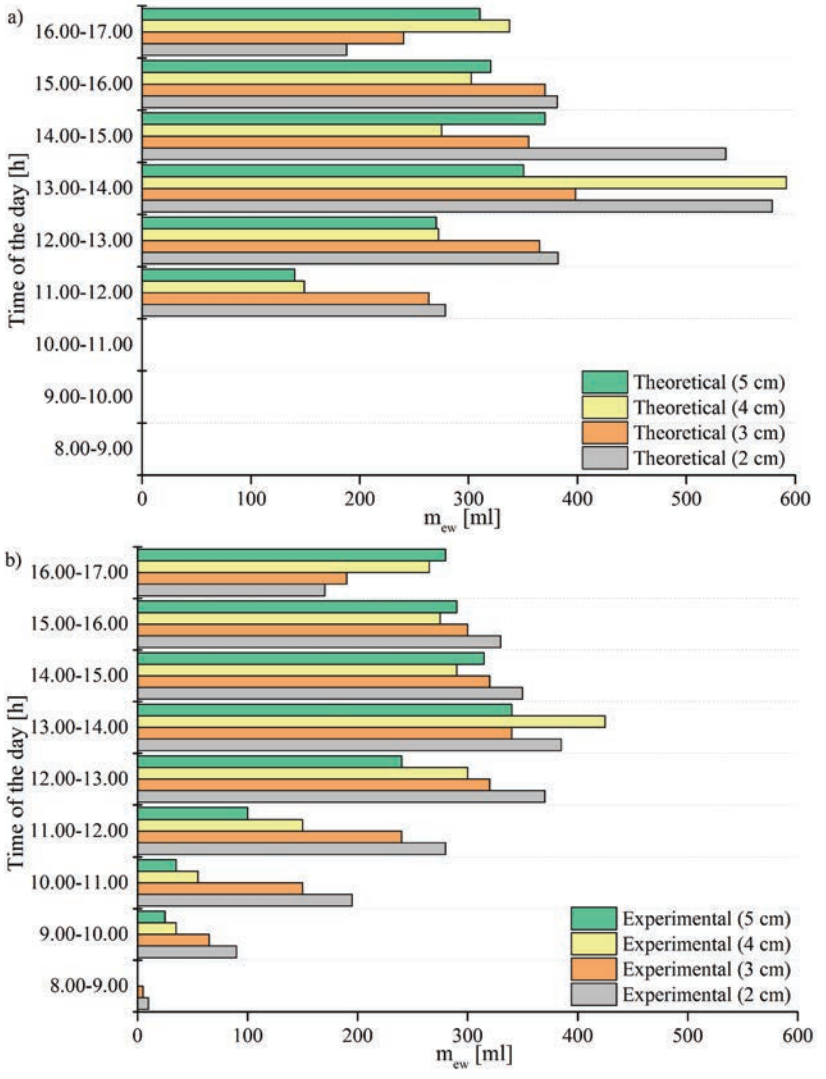

Fig. 7. *Hourly yield from per m² area of the solar still at 2 cm, 3 cm, 4 cm and 5 cm water depth; a) theoretical, and b) experimental*

study, the radiative heat transfer coefficient for 2 cm and 3 cm depth are higher because of the high basin temperature and higher evaporation associated with these depths, leading to increases in glass temperature as the h_{rw} is the function of both glass and basin water temperature. It was also observed that the h_{ew} (west surface) was much higher for 3 cm compared to h_{rw}, but the variation in h_{rw} for 2 cm and 3 cm (Fig. 6) is closer due to higher evaporation compensated by higher basin temperature for 2 cm depth.

Fig. 7 shows the theoretical (calculated from Eq. (17)) and experimental yield from the still for 2 cm, 3 cm, 4 cm, and 5 cm water depths in the basin. The theoretical yield from the still is higher than the experimental yield, but sometimes it is lower than experimental because of the atmospheric condition like wind speed; due to this, the vapour is condensed rapidly, whereas the theoretical yield depends on the temperature difference between the glass and basin water; also. the data recorded are average data. The yield for 2 cm water depth is higher than 3 cm, 4 cm. and 5 cm water depths. This proves that the yield is higher for a lower basin mass. After 15 00 h, it can be seen that the yield for 2 cm depth is decreasing at a faster rate compared to other higher depts. This is due to the heat-storing capacity of the basin mass. This proves that the evening and off-sun time production is higher for higher basin mass. Before the afternoon, the yield rate is higher for 2 cm depth because of the higher evaporation rate as compared to other water depths.

The wind has a positive effect on yield with higher depth compared to a lower depth. This is because the lesser depth (2 cm) of basin water's temperature decreases faster, which enhances the yield. While for higher depth (4 cm), this has a less negative effect due to the higher energy storing capability of water mass. It can be seen from Figs. 3 and 7 that the yield is higher when wind speed increases. This is because of the higher temperature gradient between the basin water condensing glass cover for 4 cm compared to the 2 cm depth water depth. The yield from the still is higher for the 4 cm depth between 13 00 h and15 00 h not only because of the wind speed but also due to the higher water mass, which stores more thermal energy and release during this time period. From Fig. 7, it can be seen that the rate of production increases for 2 cm as well as 4 cm depths at a very high rate. This is due to an increase in wind speed and the high solar radiation during this period.

4 CONCLUSIONS

The DSSS of acrylic with basin area 1 m² with an inclination angle of 30° was fabricated for the climatic condition of Sultanpur, Uttar Pradesh, India. Various experiments were performed on this setup to analyze the effect of parameters, including different depths (2 cm, 3 cm, 4 cm and 5 cm), the wind velocity effect on the yield, and heat transfers. The experimental and theoretical yields have been compared. The following conclusions have been drawn from the present study.

1. Convective and evaporative heat transfers are the most critical parameter for a solar distillation unit. The maximum value of h_{ew} (30.5 W/(m²K), 29.2 W/(m²K), 31.25 W/(m²K) and 31.0 W/(m²K)) and h_{cw} (2.48 W/(m²K), 2.25 W/(m²K), 2.19 W/(m²K) and 2.18 W/(m²K)) was found for 2 cm, 3 cm, 4 cm, and 5 cm depths, respectively.
2. The radiative heat transfer coefficient is found to be a maximum of 89 W/(m²K) for 2 cm depth, and it increases as the rate of condensation increases on the glass surface.
3. The yield from the still increases as the basin water depth decreases because the lower basin water requires less time to come into steady-state, and due to this, the evaporation starts earlier.
4. On increasing the depth from 2 cm to 4 cm, the yield decreases by 17.2 %. In comparison, it decreases by 25.4 % when the water depth is 5 cm. The maximum yield of 2.5 l/m² per day is found for 2 cm water depth. The theoretical and experimental yield from solar still agreed with an error of 7.5 %, 3.25 %, 7.4 % and 8.4 % for 2 cm, 3 cm, 4 cm and 5 cm water depths, respectively.
5. The afternoon production is higher for the higher basin mass because of the heat-storing capacity of basin mass.
6. During the initial time duration of still (i.e. 1 h to 2 h of operations), the rate of convective, evaporative, and radiative heat transfer coefficients is less. This is due to the slow heating of water mass in the basin because of the outer glass surface at a higher temperature than the lower surface.
7. The yield of DSSS increases as the wind speed increase because this leads to faster condensation at the glass surface. The higher basin mass temperature is less affected by the variation in wind velocity.

5 NOMENCLATURES

$\dot{q}_{cw}$ rate of convective heat transfer from water to glass cover, [W/m^2]
h_{cw} convective heat transfer coefficient from water to condensing cover, [W/(m^{2}K)]
$\dot{q}_{ew}$ rate of evaporative heat transfer from water to glass cover, [W/m^2]
h_{ew} evaporative heat transfer coefficient, [W/(m^{2}K)]
$\dot{q}_{rw}$ rate of radiative heat transfer from water to glass cover, [W/m^2]
h_{rw} radiative heat transfer coefficient, [W/(m^{2}K)]
ε_{eff} effective emissivity of glass and water, [-]
ε_g emissivity of glass, [-]
ε_w emissivity of water, [-]
ρ Stefan Boltzmann constant, [W/(m^{2}K^4)]
$\dot{q}_g$ rate of total heat transfer from glass cover to ambient, [W/m^2]
$\dot{q}_{rg}$ rate of radiative heat transfer from glass cover to ambient, [W/m^2]
h_{rg} radiative heat transfer coefficient from glass cover to ambient, [W/(m^{2}K)]
$\dot{q}_{cg}$ rate of convective heat transfer from glass cover to ambient, [W/m^2]
h_{cg} convective heat transfer coefficient from glass surface to ambient, [W/(m^{2}K)]
$\dot{q}_{tg}$ rate of total heat transfer from glass cover to ambient, [W/m^2]
h_{tg} total heat transfer coefficient from glass surface to ambient, [W/(m^{2}K)]
U_b bottom heat loss coefficient, [W/(m^{2}K)]
U_e side heat loss coefficient, [W/(m^{2}K)]
h_w convective heat transfer coefficient from basin liner to water, [W/(m^{2}K)]
h_{cb} convective heat transfer coefficient from basin liner to ambient, [W/(m^{2}K)]
h_{rb} radiative heat transfer coefficient from basin liner to ambient, [W/(m^{2}K)]
h_b overall heat transfer coefficient from basin liner to ambient through bottom, [W/(m^{2}K)]
T_g temperature of condensing cover, [°C]
T_b temperature of basin, [°C]
T_w water temperature, [°C]
T water vapour temperature, [°C]
T_{sky} temperature of sky, [°C]
T_a ambient temperature, [°C]
V wind velocity, [m/s]
t_i thickness of insulation material, [m]
K_i thermal conductivity of insulation material, [W/(m·K)]
P_w partial vapour pressure at water temperature, [N/m^2]
P_g partial vapour pressure at glass temperature, [N/m^2]
m_{ew} distillate output, [kg/m^2/h]
L latent heat of vaporization, [J/kg]
h_b overall heat transfer coefficient from basin liner to ambient through bottom insulation, [W/(m^{2}K)]
AS surface area in contact with water, [m^2]
AS area of the basin of the distiller, [m^2]

6 REFERENCES

[1] Kannan, N., Vakeesan, D. (2016). Solar energy for future world: A review. *Renewable and Sustainable Energy Reviews*. vol. 62, p. 1092-105, **DOI:10.1016/j.rser.2016.05.022**.

[2] Patel, R.V.P., Kumar, A. (2017). Experimental investigation of double slope solar still for the climatic condition of Sultanpur. *International Journal of Engineering and Technology*, vol. 9, no. 6, p. 4019-4033, **DOI:10.21817/ijet/2017/v9i6/170906309**.

[3] Patel, R.V., Bharti, K., Singh, G., Mittal, G., Singh, D.B., Yadav, A. (2021). Comparative investigation of double slope solar still by incorporating different types of collectors: A mini review. *Materials Today: Proceedings*, vol. 38, p. 300-304, **DOI:10.1016/j.matpr.2020.07.338**.

[4] Misra, S., Patel, R.V., Kumar, A., Yadav, A., Patel, V. (2021) Effect of Climatic Conditions and Water Depth on Yield of Single Slope Solar Still. *Current Advances in Mechanical Engineering: Select Proceedings of ICRAMERD 2020*, p. 137-147, **DOI:10.1007/978-981-33-4795-3_14**.

[5] Sharshir, S.W., Ellakany, Y.M., Algazzar, A.M., Elsheikh, A.H., Elkadeem, M.R., Edreis, E.M.A., Waly, A.S., Sathyamurthy, R., Panchal, H., Elashry, M.S. (2019). A mini review of techniques used to improve the tubular solar still performance for solar water desalination. *Process Safety and Environmental Protection*, vol. 124, p. 204-212, **DOI:10.1016/j.psep.2019.02.020**.

[6] Tiwari, A.Kr., Tiwari, G.N. (2006). Effect of water depths on heat and mass transfer in a passive solar still: in summer climatic condition. *Desalination*, vol. 195, no. 1-3, p. 78-94, **DOI:10.1016/j.desal.2005.11.014**.

[7] Zarasvand Asadi, R., Suja, F., Ruslan, M.H., Jalil, N.A. (2013). The application of a solar still in domestic and industrial wastewater treatment. *Solar Energy*, vol. 93, no. 63-71, **DOI:10.1016/j.solener.2013.03.024**.

[8] Ali, M.T., Fath, H.E.S., Armstrong, P.R. (2011). A comprehensive techno-economical review of indirect solar desalination. *Renewable and Sustainable Energy Reviews*, vol. 15, no. 8, p. 41874199, **DOI:10.1016/j.rser.2011.05.012**.

[9] Dev, R., Abdul-Wahab, S.A., Tiwari, G.N. (2011). Performance study of the inverted absorber solar still with water depth and total dissolved solid. *Applied Energy*, vol. 88, no. 1, p.252-264, **DOI:10.1016/j.apenergy.2010.08.001**.

[10] Phadatare, M.K., Verma, S.K. (2007). Influence of water depth on internal heat and mass transfer in a plastic solar still. *Desalination*, vol. 217, no. 1-3, p. 267-275, **DOI:10.1016/j.desal.2007.03.006**.

[11] Tripathi, R., Tiwari, G.N. (2006). Thermal modeling of passive and active solar stills for different depths of water by using the

concept of solar fraction. *Solar Energy*, vol. 80, p. 956-967, **DOI:10.1016/j.solener.2005.08.002**.

[12] Feilizadeh, M., Karimi Estahbanati, M.R., Ahsan, A., Jafarpur, K., Mersaghian, A. (2016). Effects of water and basin depths in single basin solar stills: An experimental and theoretical study. *Energy Conversion and Management*, vol. 122, p. 174-181, **DOI:10.1016/j.enconman.2016.05.048**.

[13] El-Sebaii, A.A. (2011). On effect of wind speed on passive solar still performance based on inner/outer surface temperatures of the glass cover. *Energy*, vol. 36, no. 8, p. 4943–4949. **DOI:10.1016/j.energy.2011.05.038**.

[14] El-Sebaii A.A. (2004). Effect of wind speed on active and passive solar stills. *Energy Conversion and Management*, vol. 45, no. 7-8, p. 1187–1204, **DOI:10.1016/j.enconman.2003.09.036**.

[15] Danish, S.N., El-Leathy, A., Alata, M., Al-Ansary, H. (2019). Enhancing solar still performance using vacuum pump and geothermal energy. *Energies*, vol. 12, no. 3, art. ID 539, **DOI:10.3390/en12030539**.

[16] Thalib, M.M., Manokar, A.M., Essa, F.A., Vasimalai, N., Sathyamurthy, R., Garcia Marquez, F.P. (2020). Comparative study of tubular solar stills with phase change material and nano-enhanced phase change material. *Energies*, vol. 13, no. 15, art. ID. 3989, **DOI:10.3390/en13153989**.

[17] Singh, R., Kumar, A., Yadav, A. (2019). Performance analysis of the solar photovoltaic thermal system using phase change material. *IOP Conference Series: Materials Science and Engineering*, vol. 577, art. ID 012166, **DOI:10.1088/1757-899X/577/1/012166**.

[18] Safaei, M.R., Goshayeshi, H.R., Chaer, I.. (2019). Solar still efficiency enhancement by using graphene oxide/paraffin nano-PCM. *Energies*, vol. 12, no. 10, art. ID 2002, **DOI:10.3390/en12102002**.

[19] Nazari, S., Safarzadeh, H., Bahiraei, M. (2019). Performance improvement of a single slope solar still by employing thermoelectric cooling channel and copper oxide nanofluid: An experimental study. *Journal of Cleaner Production*, vol. 208, p. 1041-1052, **DOI:10.1016/j.jclepro.2018.10.194**.

[20] El-Sebaey, M.S., Ellman, A., Hegazy, A., Ghonim, T. (2020). Experimental analysis and CFD modeling for conventional basin-type solar still. *Energies*, vol. 13, no. 21., art. ID 5734, **DOI:10.3390/en13215734**.

[21] Rahbar, N., Esfahani, J.A. (2013). Productivity estimation of a single-slope solar still: Theoretical and numerical analysis. *Energy*, vol. 49, no. 289-297, **DOI:10.1016/j.energy.2012.10.023**.

[22] Setoodeh, N., Rahimi, R., Ameri, A. (2011). Modeling and determination of heat transfer coefficient in a basin solar still using CFD. *Desalination*, vol. 268, no. 1-3, 103-110, **DOI:10.1016/j.desal.2010.10.004**.

[23] Madhlopa, A. (2014). Modelling radiative heat transfer inside a basin type solar still. *Applied Thermal Engineering*, vol. 73, no. 1, p. 707-711, **DOI:10.1016/j.applthermaleng.2014.07.065**.

[24] Keshtkar, M., Eslami, M., Jafarpur, K. (2020). A novel procedure for transient CFD modeling of basin solar stills: Coupling of species and energy equations. *Desalination*, vol. 481, art. ID 114350, **DOI:10.1016/j.desal.2020.114350**.

[25] Dunkle, R.V. (1961). Solar wter distillation: the roof type still and a multiple effect diffusion still. *International Developments in Heat Transfer, ASME, Proceeding of International Heat Transfer*, part V, p. 895.

[26] Fernández, J., Chargoy, N. (1990). Multi-stage, indirectly heated solar still. *Solar Energy*, vol. 44, no. 4, p. 215-223, **DOI:10.1016/0038-092X(90)90150-B**.

[27] Watmuff, J.H., Charters, W.W.S., Proctor, D. (1977). Solar and wind induced external coefficients-solar collectors. *CMES*, p. 56.

[28] Shukla, K.S., Rai, A.K. (2008). Analytical thermal modeling of double slope solar still by using inner glass cover temperature. *Thermal Science*, vol. 12, no. 3, p. 139-152, **DOI:10.2298/TSCI0803139S**.

Strojniški vestnik - Journal of Mechanical Engineering 67(2021)7-8, 380-388
DOI:10.5545/sv-jme.2021.7253
Original Scientific Paper
Received for review: 2021-05-12
Received revised form: 2021-06-17
Accepted for publication: 2021-07-09

Mechanical Properties of Adhesive Joints Made with Pressure-Sensitive Adhesives

Anna Rudawska[1,*] – Magd Abdel Wahab[2,3]

[1] Lublin University of Technology, Faculty of Mechanical Engineering, Poland
[2] Duy Tan University, Institute of Research and Development, Vietnam
[3] Ghent University, Faculty of Engineering and Architecture, Belgium

The paper aims to determine the mechanical properties of the adhesive joints made with acrylic pressure-sensitive adhesives. Two types of double-sided acrylic pressure-sensitive adhesive tapes are used. Three construction materials are used to prepare the adhesive joints: structural steel sheet (C45), aluminium alloy sheet (EN-AW 5754), and titanium sheet (Grade 2). Strength tests of adhesive joints made with the pressure-sensitive adhesive tapes are carried out both after conditioning time at room temperature (23 °C) and subjected to thermal shocks (500 cycles: +60 °C / –40 °C). Strength tests are carried out based on the DIN EN 1465 standard on a Zwick/Roell Z150 testing machine. The main conclusion from the tests carried out was the positive effect of thermal shocks on the mechanical strength of joints bonded with pressure-sensitive adhesive tape.

Keywords: adhesive joint, pressure-sensitive adhesive, mechanical properties, thermal shocks

Highlights

- *In the investigated range of the thermal shocks, the post-conditioning does not appear to trigger the deterioration of the mechanical properties of the adhesive joints bonded with the pressure-sensitive adhesive tapes.*
- *The increase in the adhesive joints' strength is also associated with the type of adherend.*
- *There is a positive correlation between the thermal shocks and the mechanical strength of the adhesive joint bonded with the pressure-sensitive adhesive tapes.*
- *The pressure-sensitive adhesive tapes exhibit a good capacity for bonding the considered adherends under the considered conditions.*

0 INTRODUCTION

Assembly joints can be made using various joining methods, including bonding [1] to [3]. One type of adhesive material used in assembly processes is pressure-sensitive adhesives. Pressure-sensitive adhesive tape is an alternative to conventional mechanical joining methods, including screws, rivets, dowels and other fasteners. In addition to bonding, i.e., their primary function, adhesive tape is also used for sealing purposes, by protecting bonded components against penetration by an external medium [1], [4], and [5]. Manufacturers of industrial pressure-sensitive adhesive tapes will sometimes develop their products tailored to specific assembly and industry needs [6] to [8].

The term "pressure-sensitive" describes adhesives that are aggressively and permanently tacky in the dry form at room temperature and firmly adhere to a variety adherends' surfaces upon mere contact, without the need of more than hand pressure [9]. Pressure-sensitive adhesives consist mainly of tacky polymeric materials that adhere to adherends surface upon applying a contact pressure [9] to [11]. Pressure-sensitive adhesives require a balance of cohesive strength and viscoelastic properties. Such adhesives can be easily detached from the adherend surface and may be reusable [12]. An essential property of pressure-sensitive adhesive tapes is their tack performance, which relates the adhesive force generated by a small short-term pressure on the tapes [12]. One of the important features of pressure-sensitive adhesive tapes is their flexibility (even exceptional flexibility), which allows for relative component movement in the assembly related to the thermal expansion of adherends [4], [5], [13], and [14].

Various issues of mechanical properties related to pressure-sensitive adhesives are presented in many works [7], [11], [12], and [15] to [17]. Czech and Milker [7] underlined that pressure-sensitive adhesives (PSA) presented a novel generation of self-adhesives with a large number of excellent properties. In this work, several groups of pressure-sensitive adhesives were described. Foster et al. [15] defined bonding principles for the development of commercial water-bone pressure-sensitive adhesive. Zosel [17] presented that the correlations between shear resistance and the mechanical properties of pressure-sensitive adhesives. Also, issues related to the rheological properties of pressure-sensitive

*Corr. Author's Address: Lublin University of Technology, Nadbystrzycka 38D, Lublin, Poland, a.rudawska@pollub.pl

adhesive on the mechanical behaviour were discussed, among others in the works [10], [16], and [18] to [20]. Dynamic mechanical properties of pressure-sensitive adhesives were presented by Chu [10]. Marin and Derail [20] investigated the relationship between rheological and peeling properties for hot-melt pressure-sensitive adhesives based on homopolymers or copolymers blended with tackifier resins. Sun et al. [21] indicated that the mechanical properties of pressure-sensitive adhesives are usually described by tack, shear resistance and peel strength. Sosson et al. [22] investigated the shear failure mechanisms of pressure-sensitive adhesive. The effect of tackifier on the adhesive properties of pressure-sensitive adhesives tape was investigated by Sasaki et al. [23].

The article characterizes adhesive joints formed using industrial pressure-sensitive adhesive tapes that were subjected to temperature shock testing. The major finding emerging from the tests was the positive effect of thermal shocks on the mechanical strength of pressure-sensitive adhesive tape bonded joints.

1 METHODS AND EXPERIMENTAL

1.1 Adherends and Pressure-Sensitive Adhesives

The substrates bonded using the tested adhesive tapes were: C45 steel sheets (PN/EN 10083 -2), EN-AW 5754 aluminium alloy sheets (PN-EN 573) and Grade 2 titanium sheets (according to American standard ASTM F67 2000-Ti Grade 2). The thickness of the adherends was 1 ± 0.02 mm.

Two pressure-sensitive adhesives in the form of double-sided tapes were subjected to testing: 3M VHB double-sided tape (3M company, VHB brand, No. 49 , 3M Deutschland GmbH) and 3M Scotch® double-sided pressure-sensitive adhesive tape (3M company, Scotch® Brand, 3M Deutschland GmbH). Table 1 lists the characteristics of the 3M VHB tape. The presented characteristics have been prepared based on the information provided on the manufacturer's websites [24] to [26].

Table 1. *Characteristics of 3M VHB pressure-sensitive adhesive tape*

Properties	Details/value
Adhesive tape specification	Double-sided adhesive tape
Adhesive type	Multi-purpose acrylic
Foam type	Acrylic foam
Density	720 kg/m³
Liner	PE film

The maximum and minimum operating temperatures are +90 °C and –40 °C. Short- and long-term temperature resistance are 149 °C and 9 °C, respectively.

Selected properties of the 3M Scotch® double-sided pressure-sensitive adhesive tape are shown in Table 2. The maximum and minimum operating temperatures are +93 C and -53 C.

Table 2. *Characteristics of 3M Scotch® pressure-sensitive adhesive tape*

Properties	Details/value
Adhesive tape specification	Double-sided adhesive tape
Adhesive type	Modified acrylic
Liner	PET

1.2 Adhesive Joints and Adhesives Samples

Two research objects were used in the study: single-lap adhesive joints of three construction materials, i.e., structural steel sheet (C45 , aluminium alloy sheet (EN-AW 5 and titanium sheet (Grade 2), joined with pressure-sensitive adhesives, and a pressure-sensitive adhesive in the form of rectangular samples.

The single-lap adhesive joints (Fig. 1) have the following dimensions: sheet width (*ws*) 20±0.12 mm, sheet length (*Ls*) 100±0.2 mm, overlap length after curing process (*ld*) 20±0.8 mm, sheet thickness *g* = 1±0.02 mm, adhesive tape thickness (*td*): 3M VHB pressure-sensitive adhesive tape 1.1 mm, 3M Scotch® 1.9m m.

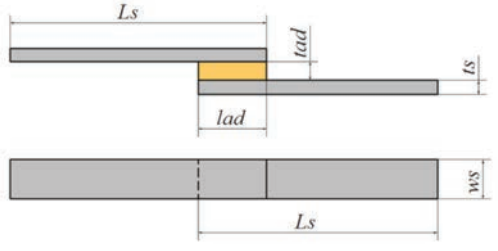

Fig. 1. *The parametric scheme of single-lap adhesive joints*

For each type of adherends and pressure-sensitive adhesives, 8 adhesive joints were made. A total of 0 adhesive joint samples were subjected to strength tests (3 types of adherends × 2 types of pressure-sensitive adhesives, tapes × 2 variants of testing conditions × 8 samples).

The dimensions of rectangular samples of pressure-sensitive adhesives are 100 mm × 20 mm. For each pressure-sensitive adhesive variant, 6 adhesive samples were made.

1.3 Bonding Technology

The adhesive joints were prepared in several steps: adherend surface preparation, cutting off the pressure-sensitive adhesive tape, applying the adhesive onto adherends surfaces, and curing.

1.3.1 Surface Treatment and Applying the Adhesive

The surface treatment of adherends prior to bonding consisted of degreasing with acetone. Specifically, the degreasing agent was applied in 3 repetitions onto the surfaces: after the first two applications, it was wiped off with dust-free swabs; after the third application, the samples were allowed to dry for approx. 2 minutes. The surface treatment procedure was performed at 26±1 °C and humidity 40 ±1 %.

The pressure-sensitive adhesive tape was cut with scissors to the required overlap length of 20 mm. Next, it was applied onto one of the adherend surfaces and pressed appropriately once the adherend and the adhesive tape were in line. Given that the bond strength is relative to the condition and the size of the contact surface (according to theoretical mechanics), an even amount of pressure needed to be applied. To ensure better contact between the tape and the bonded surface, and thus to increase the strength of the fixture, the proper pressure was applied with a hand roller.

1.3.2 Curing

Once the joint was assembled, it was subjected to curing, according to the following procedure:

- 2-hour subjecting under a load of 0.20 MPa, at a temperature of 26±1 °C and humidity of 41 ±1 %,
- hold at a temperature of 10 ±1 °C for 10 minutes (Fig. 2),
- cooling at 26±1 °C for 1 hour.

During curing, the joints were heat-treated at an elevated temperature to accelerate and improve the deposition of the tape adhesive in the irregularities of the adherends. The curing was carried out in a climatic chamber SH-6 (Klimatest, Poland).

The bonded joints were subsequently conditioned at 23±1 °C and relative humidity of 28±1 % for 24 hours, upon which time their quality was verified in visual inspection. Finally, the specimens were divided into two test batches that differed in terms of the thermal post-treatment.

1.3.3 Thermal Post-Conditioning

Prior to failure strength tests, the specimens from the first test group (RT) conditioning in room temperature, whereas for the second variant (TS) the specimens were additionally subjecting using thermal shocks, carried out using a thermal shock chamber STE 11 (ESPEC, Klimatest, Poland). The test groups are described in Tables 3 and 4.

Table 3. *Description of test groups*

Test group variant	RT (without thermal shocks)	TS (with thermal shocks)
Conditions	Temperature: 23 ± 1 °C RH: 28 ± 1 % Time: 24 h	500 cycles 1 cycle: +60 °C / 15 min. and −40 °C / 15 min.

Table 4. *Description of test adhesive joints*

Adherend (designation)	Adhesive tape 3M	Test group	Designation of adhesive joints
Steel (S)	VHB	RT	S/VHB/RT
	Scotch®		S/S/RT
	VHB	TS	S/VHB/TS
	Scotch®		S/S/TS
Aluminium alloy (Al)	VHB	RT	Al/VHB/RT
	Scotch®		Al/S/RT
	VHB	TS	Al/VHB/TS
	Scotch®		Al/S/TS
Titanium (Ti)	VHB	RT	Ti/VHB/RT
	Scotch®		Ti/S/RT

1.4 Strength Test

The shear strength tests of adhesive joints were conducted according to the DIN EN 1 standard test temperature 23±1 °C and during the test speed of 10 mm/min, using Zwick/Roell Z2.5 testing machine (Zwick/Roell GmbH&Co. KG, Ulm, Germany).

The elongation strength tests pressure-sensitive adhesive samples were performed at test temperature 23±1 °C and during the test speed, according to DIN EN ISO 37 1 standard, using Zwick/Roell Z2.5 testing machine (Zwick/Roell GmbH&Co. KG, Ulm, Germany).

2 RESULTS

2.1 Mechanical Properties of Adhesive Joints - RT Variant: Conditioning in Room Temperature

Figs. 2 and 3 compare the results from shear strength tests of steel sheet, aluminium alloy sheet and

titanium sheet adhesive joints bonded using two pressure-sensitive adhesive tapes. Specifically, Fig. 2 reports the strength performance of these joints, and Fig. 3 compares the elongation at break of joints under testing conditions. The designations in the charts in Figs. 2 and 3 have been adopted in accordance with the designations presented in Table 5

From the data presented in Fig. 2, it can be seen that adhesive joints bonded with the acrylic adhesive tape tended to develop higher strength, regardless of the adherends. With respect to the material of adherends, the aluminium alloy was shown to develop the highest shear strength of all the joints, both when bonded with the 3M VHB (0.8 MPa) and the 3M Scotch® (0.28 MPa) pressure-sensitive adhesive tapes. For these types of joints, the difference in the shear strength amounted to approx. 27 %. The lowest shear strength was recorded for the adhesive joints of titanium sheets. This applies to both types of pressure-sensitive adhesive tapes: 3M VHB (0.5 MPa) and 3M Scotch® (0.15 MPa). The shear strength of titanium adhesive joints joined with 3M Scotch® pressure-sensitive adhesive tape corresponded to approx. 40 % of the shear strength of adhesive joints made with 3M VHB pressure-sensitive adhesive tape.

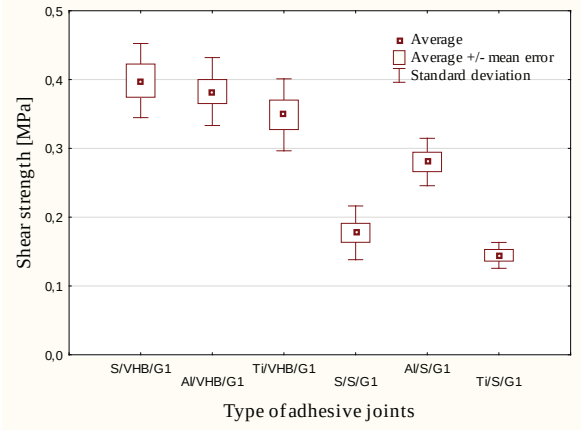

Fig. 2. *Shear strength of tested adhesive joints - RT variant*

A meaningful difference in shear strength was also observed in the case of steel sheet joints. The strength of joints made with the 3M VHB pressure-sensitive adhesive tape is 0.5 MPa and 0.18 MPa with the use of 3M Scotch® pressure-sensitive adhesive tape, which corresponds to almost 60 % of the difference between the strength of the compared adhesive joints. In general, in all material cases, greater strength was observed when using 3M VHB pressure-sensitive adhesive tape.

As indicated in the previous paragraph, significantly greater differences in the strength values were observed in the joints bonded with 3M Scotch® pressure-sensitive adhesive tape (nearly 60 %), which can be interpreted as the effect of this type of tape sensitivity to the type of adherend used in the bonding processes. Similar dependencies result from the analysis of the elongation of adhesive joints (Fig. 3).

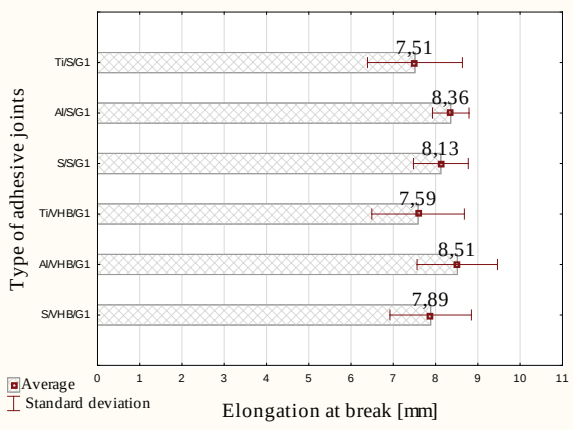

Fig. 3. *Elongation at break of tested adhesive joint – RT variant*

Considering the elongation values (Fig. 3), it can be seen that there are no statistical differences of elongation between the different tapes (3M VHB and 3M Scotch® pressure-sensitive adhesive tapes) for the same material due to the relatively high standard deviations. Considering all variants of the samples of adhesive joints depending on the base material, it can be seen that the highest elongation was obtained in aluminium alloys adhesive joints, and the lowest in titanium adhesive joints. Moreover, for the pressure-sensitive adhesive tapes used, the difference between the highest and lowest average elongation is similar and amounts to approximately 10 %; however, it has also been shown that the type of adherends affects the properties of the joints (including the elongation) in strength tests.

2.2 Mechanical PROPERTIES of Adhesive Joints - RT Variant: Conditioning in Room Temperature

The results obtained from the shear strength tests conducted on adhesive joints of steel and aluminium alloy sheet substrates that were bonded with the two types of pressure-sensitive adhesive tapes are reported in Figs. 4 and 5

Several observations emerge from the comparative analysis of the performance (shear strength and elongation at break) of pressure-sensitive

adhesive tape joints subjected to 100 thermal shock cycles (Figs. 4a nd 5) :

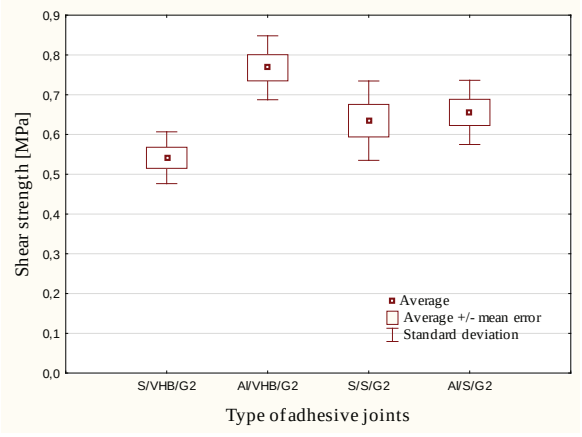

Fig. 4. *Shear strength of tested adhesive joints - TS variant*

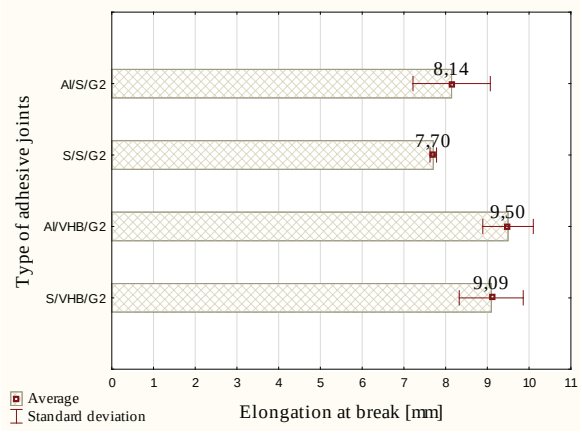

Fig. 5. *Elongation at break of tested adhesive joint – TS variant*

- the strength parameters of adhesive joints of aluminium alloy determined in tests were higher compared to the steel adhesive joints, which applies to both types of pressure-sensitive adhesive tapes,
- the aluminium alloy adhesive joints bonded with the 3M VHB pressure-sensitive adhesive tape were stronger than the steel adhesive joints by 27 % on average,
- the difference in joint strength was less significant in the case of the 3M Scotch® pressure-sensitive adhesive tape, amounting to 3% on average,
- when comparing the elongation of specimens bonded using the 3M VHB pressure-sensitive adhesive tape, the difference between the adherends was equal to 4 %, while for the 3M Scotch® pressure-sensitive adhesive tape it was 11 % on average.

The bonded joints of titanium sheets exhibited the lowest strength, regardless of the type of adhesive type used and were therefore excluded from thermal shock testing.

2.3 Mechanical Properties of Adhesives

The results of strength parameters pressure-sensitive adhesive tapes shown that the average value of the tensile strength of the 3M VHB pressure-sensitive adhesive tape was 0.4 0.03 MPa, whereas the average value of the tensile strength of 3M Scotch® pressure-sensitive adhesive tape was 0.34 ± 0.06 MPa. The modulus of the 3M VHB pressure-sensitive adhesive tape was 1.0 ± 0.12, and the modulus of the 3M Scotch® pressure-sensitive adhesive tape was 0.23 ± 0.09

It can be seen that 3M VHB pressure-sensitive adhesive tape is characterized by a 20 % higher value of tensile strength than Scotch pressure-sensitive adhesive tape. In the case of the tensile modulus, it was observed that the 3M Scotch® pressure-sensitive adhesive tapes have almost 5 times lower value compared to the VHB pressure-sensitive adhesive tape. Elongation at break was at a similar level, and no significant differences were observed, i.e., for the 3M VHB pressure-sensitive adhesive tape was 20 $\pm$4 %, and was 3 $\pm$0% for the 3M Scotch® pressure-sensitive adhesive tape.

3 DISCUSSION

The comparison of the results of shear strength of adhesive joints curing and conditioning in room temperature (RT) and additionally subjected to thermal shocks (TS) was presented in Figs. 6a nd 7

Based on the results presented in Fig. 6, it can be seen that the strength of steel adhesive joints that were subjected to thermal shocks is higher than those of joints that were conditioned at ambient temperature. However, the extent to which the presence of thermal shocks contributes to improving the strength properties of steel adhesive joints depends on the type of pressure-sensitive adhesive tape in use. The adhesive joints bonded with the 3M VHB pressure-sensitive adhesive tape were observed to develop strength increased by 3 % when thermal shock treatment was applied. The difference was even higher in adhesive joints bonded with the 3M Scotch® pressure-sensitive adhesive tape, in which case the increase in the strength of adhesive joints exceeded 80 %.

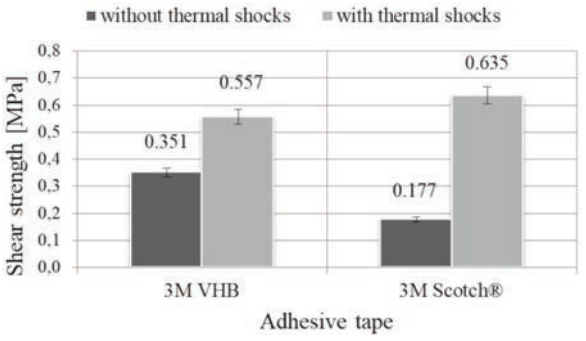

Fig. 6. *The shear strength of steel adhesive joints subjected and not subjected to thermal shock testing*

Considering the correlation between the type of adherend of adhesive joints after thermal shock and the type of pressure-sensitive adhesive tapes, it was observed that the steel adhesive joints prepared with the 3M Scotch® pressure-sensitive adhesive tape showed a 15 % higher strength than the steel adherends bonded with the 3M VHB pressure-sensitive adhesive tape: 0.63 MPa and 0.54 MPa, respectively. In the adhesive joints not subjected to thermal shocks, the opposite mechanism occurred: steel adhesive joints bonded with the 3M VHB pressure-sensitive adhesive tape were capable of resisting higher loads than the 3M Scotch® pressure-sensitive adhesive tape-bonded joints. Also, the difference was far more significant, reaching close to 60 %. What may be then inferred from the observation is that thermal shocks contribute to a certain "levelling-off" of the strength properties of pressure-sensitive adhesive tape, and thus exhibit a positive effect on the strength of adhesive joints.

Considering the shear strength of adhesive joints of aluminium alloy sheets not subjected to and subjected to thermal shock, significant differences in the results of this strength parameter were observed (Fig. 7). Adhesive joints subjected to thermal shocks were characterized by higher shear strength of their joints, and this difference is more than twofold.

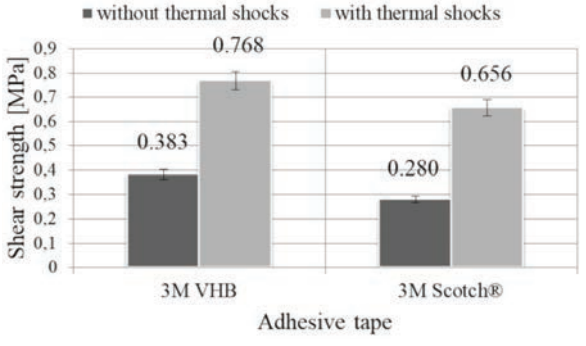

Fig. 7. *The shear strength of the aluminium alloy adhesive joints subjected and not subjected to thermal shock testing*

After the thermal shock, the adhesive joints of aluminium alloy sheets joined with 3M VHB pressure-sensitive adhesive tape (0.7 MPa) are almost 15 % more durable than joints made with 3M Scotch® pressure-sensitive adhesive tape (0.6 MPa). As in the case of bonding steel sheets, there is a clear discrepancy between the strength of adhesive joints prepared with 3M VHB and 3M Scotch® pressure-sensitive adhesive tapes not subjected to thermal shocks: it amounted to approx. 27 %. Therefore, it can be assumed that the heat causes the pressure-sensitive adhesive to cross-link further, as a result of which the properties of the adhesive joints become similar. Nevertheless, other factors were likely to have contributed to this, such as their specific material properties

Thermal shocks are widely known to be among the factors degrading polymer materials, including adhesives. According to the definition of the term, degradation is a process of structural modification that may result from physical or chemical changes occurring within the polymer under the long-term impact of various external factors [4] and [5]. Okba et al. [5] presented that the decrease of residual compressive and tensile strengths depends on the type of polymer adhesive, level of elevated temperature, type of applied stress and, to a lesser degree, on exposure time. The residual bond strength was reduced, and the mode of failure changed due to the high temperature, prolonged exposure time, type of polymer adhesive and the increase in the surface area of the bond. Gilbert et al. [19] investigated the effect of the rheological properties of industrial hot-melt and pressure-sensitive adhesives on the peel behaviour at various temperatures. In the conducted tests, it was noticed that the failure was cohesive with regard to the adhesive layer, and the cracks appeared at the beginning of the adhesive joint overlap. However, as it could be inferred from the results reported here, in certain cases in the first phase of degradation, the properties of an exposed material may actually improve, particularly its mechanical strength. This is a result of additional cross-linking of the material structure that is induced by heat, for example. It is only at a later stage (over a prolonged effect of degradation factors) that other processes begin to contribute, e.g., excessive cross-linking or molecular weight reduction, initiating the deterioration of such material properties, such as strength or elongation, as underlined by Benedek and Feldstein [14] and also Chang [8].

The information from the preceding paragraph and the results from the strength and elongation

tests seem to suggest that, in the reported cases, the mechanical strength of adhesive joints bonded with specific pressure-sensitive adhesive tapes was increased by subjecting the specimens to 100 thermal shock cycles, carried out at +60 °C and –40 °C. It should be noted that the applied temperatures did not exceed the values recommended by the manufacturer regarding their maximum (+90 °C for VHB pressure-sensitive adhesive tape and +93 °C for 3M Scotch® pressure-sensitive adhesive tape) or minimum operating temperatures (–40° C for VHB pressure-sensitive adhesive tape and –5 C for 3M Scotch® pressure-sensitive adhesive tape, although in the last pressure-sensitive adhesive tape the minimum temperature was slightly exceeded). However, it is probable that a greater number of cycles, i.e., increased duration of thermal shocks, could lead to a reduction in the strength of the joints under consideration due to, for instance, excessive cross-linking of the adhesive or molecular weight reduction.

The results of elongation of the adhesive joint specimens bonded with the pressure-sensitive adhesive tapes under investigation that were or were not subjected to thermal shocks are presented in Fig. 8 (steel adhesive joints) and in Fig. 9 (aluminium alloy adhesive joints).

Several observations can be drawn from the elongation tests carried out on the steel adhesive joints subjected and not subjected to thermal shocks (Fig. 8):

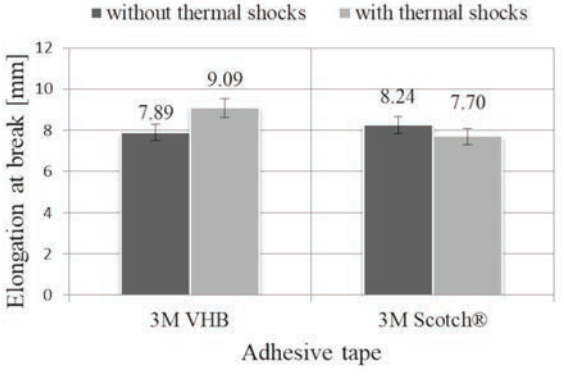

Fig. 8. *Elongation at break of steel adhesive joints with and without thermal shock*

- thermal shocking improved the elongation at break of adhesive joints bonded with the 3M VHB pressure-sensitive adhesive tape (9.09 mm). The difference between the elongation at break of adhesive joints prior to an after thermal shocks is 13%;
- adhesive joints bonded with the 3M Scotch® pressure-sensitive adhesive tape did not respond positively to thermal shocks: slightly better elongation properties were exhibited by the non-post treated joints (8.24 mm versus 7.70 mm), and this difference was approx. 6%;
- following the series of thermal shocks, adhesive joints bonded with the 3M VHS pressure-sensitive adhesive tape showed a 15 % higher elongation at break value than the 3M Scotch® pressure-sensitive adhesive tape-bonded specimens.

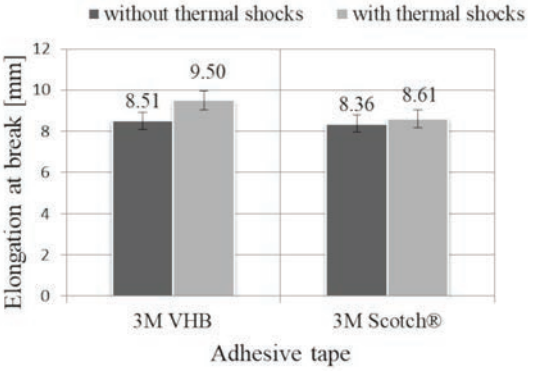

Fig. 9. *Elongation at break of the aluminium alloy adhesive joints with and without thermal shock*

Considering the results from the elongation tests presented in Fig. 9, it can be seen that:

- with respect to the type of pressure-sensitive adhesive tape bonding the aluminium alloy adherends, higher elongation at break was obtained after subjecting the adhesive joints specimens to a specific cycle of thermal shocks;
- after thermal shocks, adhesive joints bonded with the 3M VHS pressure-sensitive adhesive tape showed higher elongation at break value (by about 10 %) compared with the 3M Scotch® tape – similarly to the steel sheet joints;
- the difference in the elongation at break of the adhesive joints of the aluminium alloy adherends bonded with the 3M VHB pressure-sensitive adhesive tape subjected and not subjected to thermal shocks is 10 %, while in the same adherends adhesive joints joined with the 3M Scotch® pressure-sensitive adhesive tape, the difference is negligible – approx. 2 %.

The results above (Figs. 8 and 9) confirm that, with the exception of a single case, the applied number and type of thermal shock cycles increase the elongation at break of adhesive joints prepared with the tested pressure-sensitive adhesive tapes.

Sun et al. [21] underlined that the adhesion properties of pressure-sensitive adhesives strongly depend on surface roughness, tackifier compatibility,

monomers, cross-linking degree and others. On the basis of the obtained results, it can be observed that the type of adherends play an important role in the mechanical properties of adhesive joints prepared by pressure-sensitive adhesives. By bonding thicker (stiffer) elements, a greater strength of the joints is obtained but lower maximum stress of the joined materials under failure load. This was also confirmed in the work of Sun et al. **[21]** and in the work of Peykova et al. **[27]**, who also indicated that different surface also affects the cavity growth mechanisms.

According to Dimas et al. **[28]**, several factors determine the mechanical properties of pressure-sensitive adhesive, e.g., the type of adhesive. Although both acrylate-based pressure-sensitive adhesives were used in the study, the type of acrylic was probably different (the information is very general from the manufacturer on this subject); the thickness and the different base were different. That is, the factors mentioned by Dimas et al. **[28]** could have influenced the noticeable differences in the strength of the adhesive joints of the materials joined with the use of both tapes. According to Chu **[10]** the performance of PSA is related to the viscoelastic response of the bulk adhesives as well as to the surface energies of the adhesives and adherend. Differences in the strength of adhesive joints made with two different pressure-sensitive adhesives (Fig. 2) can probably be explained by the different structures of the adhesive layer and its thickness. The results presented by Poh and Kwo **[29]** highlighted the importance of the thickness of the adhesive layer on the adhesive substrate. They presented that, generally, peel and shear strength increase with coating thickness. The type of materials forming the pressure-sensitive adhesive is an equally important factor, which was emphasized in the works of, among others, Rodrigez et al. **[18]**, Chang **[8]**, and Marin and Derail **[20]**.

4 CONCLUSIONS

The experimental data suggest that in the investigated range of thermal shocks (the number of cycles, temperature and duration of positive and negative temperatures), commonly regarded as a degradation factor, the post-conditioning does not appear to trigger the deterioration of the mechanical properties of adhesive joints bonded with pressure-sensitive adhesive tapes; nevertheless, the increase in strength is also associated with the type of adherend. Thus, there is a positive correlation between thermal shocks and the mechanical strength of adhesive joint bonded with pressure-sensitive adhesive tapes, which should be linked primarily with additional cross-linking of the adhesive material structure under exposure to heat, and the resulting increase in the mechanical strength of the adhesive joints. An implication of this is that pressure-sensitive adhesive tapes exhibit a good capacity for bonding the considered adherends under the considered operating conditions.

5 REFERENCES

[1] Adams, R.D., Comyn, J., Wake. W.C. (1997). *Structural Adhesive Joints in Engineering Book*. Springer, London.

[2] Mojškerc, B., Kek, T., Grum, J. (2016). Pulse-echo ultrasonic testing of adhesively bonded joints in glass façades. *Strojniški vestnik - Journal of Mechanical Engineering*, vol. 62, no.3, p. 147-153, **DOI:10.5545/sv-jme.2015.2988**.

[3] Tušek, J., Klobčar, D. (2004). Current development trends for material joining in the automotive industry. *Strojniški vestnik - Journal of Mechanical Engineering*, vol. 50, no. 2, p. 94-103.

[4] Blackburn, B.P., Tatar, J., Douglas, E.P., Hamilton, H.R. (2015). Effect of hydrothermal conditioning on epoxy adhesives used in FRP composites. *Construction and Building Materials*, vol. 96, p. 679-689, **DOI:10.1016/j.conbuildmat.2015.08.056**.

[5] Okba, S.H., Nasr, E.-S.A., Helmy, A.I.I., Yousef, I.A.-l. (2017). Effect of thermal exposure on the mechanical properties of polymer adhesives. *Construction and Building Materials*, vol. 135, p. 490-504, **DOI:10.1016/j.conbuildmat.2016.12.067**.

[6] Abderrahmen, R, Gavory, C., Chaussy, D., Briançon, S., Fessi, H., Belgacem, M.N. (2011). Industrial pressure sensitive adhesives suitable for physicochemical microencapsulation. *International Journal of Adhesion and Adhesives*, vol. 31, no. 7, p. 629-633, **DOI:10.1016/j.ijadhadh.2011.06.003**.

[7] Czech, Z., Milker, R. (2005). Development trends in pressure-sensitive adhesive systems. *Materials Science Poland*, vol. 23, p. 1015-1022.

[8] Chang, E.P. (1991). Viscoelastic windows of pressure-sensitive adhesives. *Journal of Adhesion*, vol. 4, p. 189-200, **DOI:10.1080/00218469108026513**.

[9] Czech, Z. (2004). Development in the area of UV-crosslinkable solvent-based pressure-sensitive adhesive with excellent shrinkage resistance. *European Polymer Journal*, vol. 40, no. 9, p. 2221-2227, **DOI:10/1016/j.eurpolymj.2004.05.012**.

[10] Chu, S.G. (1991). Dynamic mechanical properties of pressure-sensitive adhesives. Lee, L.-H. (ed.), *Adhesive Bonding*. Springer Science+Business Media, New York, p. 97-138, **DOI:10.1007/978-1-4757-9006-1_5**.

[11] Creton, C. (2003). Pressure-sensitive adhesives: An introductory course. *MRS Bulletin*, vol. 28, p. 434-439. **DOI:10.1557/mrs2003.124**.

[12] Takahashi, K., Shimizu, M., Inaba, K., Kishimoto, K., Inao, Y., Sugizaki, T. (2013) Tack performance of pressure-sensitive adhesive tapes under tensile loading. *International Journal of Adhesion and Adhesives*, vol. 45, p. 90-97, **DOI:10.1016/j.ijadhadh.2013.05.005**.

[13] Schneider, B., Beber, V.C., Schweer, J., Brede, M., Mayer, B. (2018). An experimental investigation of the fatigue damage behavior of adhesively bonded joints under the combined

effect of variable amplitude stress and temperature variation. *International Journal of Adhesion and Adhesives*, vol. 83, p. 41-49, **DOI:10.1016/j.ijadhadh.2018.02.011**.

[14] Benedek, I., Feldstein, M.M. (2009). *Technology of Pressure-Sensitive Adhesives and Products*. CRC Press Taylor & Francis Group, Boca Raton.

[15] Foster, A.B., Lovell, P.A., Rabjohns, M.A. (2009). Control of adhesive properties through structured particle design of water-borne pressure-sensitive adhesives. *Polymer*, vol. 50, no. 7, p. 1654-1670, **DOI:10/1016/j.polymer.2009.01.054**.

[16] Kajtna, J., Alič, B., Krajnc, M., Šebenik, U. (2014). Influence of hydrogen bond on rheological properties of solventless UV crosslinkable pressure sensitive acrylic adhesive prepolymers. *International Journal of Adhesion and Adhesives*, vol. 49, p. 103-108, **DOI:10.1016/j.ijadhadh.2013.12.016**.

[17] Zosel, A. (1994). Shear strength of pressure sensitive adhesives and its correlation to mechanical properties. *Journal of Adhesion*, vol. 44, p. 1-16, **DOI:10.1080/00218469408026613**.

[18] Rodriguez, I., Lim, Ch.T., Natarajan, S., Ho, A.Y.Y., Van, E.L., Elmouelhi, N., Low, H.Y., Vyakarnam, M., Cooper, K. (2013). Shear adhesion strength of gecko-inspired tapes on surfaces with variable roughness. *Journal of Adhesion*, vol. 89, no. 12, p. 921-936, **DOI:10.1080/00218464.2013.767198**.

[19] Gibert, F.X., Allal, A., Marin, G., Derail, C. (1999). Effect of the rheological properties of industrial hot-melt and pressure-sensitive adhesives on the peel behavior. *Journal of Adhesion Science and Technology*, vol. 13, no. 9, p. 1029-1044, **DOI:10.1163/156856199X00497**.

[20] Marin, G., Derail, C. (2006). Rheology and adherence of pressure-sensitive adhesives. *Journal of Adhesion*, vol. 82, no. 5, p. 469-485, **DOI:10.1080/00218460600713618**.

[21] Sun, S., Li, M., Liu, A. (2013). A review on mechanical properties of pressure sensitive adhesives. *International Journal of Adhesion and Adhesives*, vol. 41, p. 98-106, **DOI:10.1016/j.ijadhadh.2012.10.011**.

[22] Sosson, F., Chateauminois, A., Creton, C. (2005). Investigation of shear failure mechanisms of pressure-sensitive adhesives. *Journal of Polymer Science B: Polymers Physics*, vol. 43, no. 22, p. 3316-3330, **DOI:10.1002/polb.20619**.

[23] Sasaki, M., Fujita, K., Adachi, M., Fujii, S., Nakamura, Y., Urahama, Y. (2008). The effect of tackifier on phase structure and peel adhesion of a triblock copolymer pressure-sensitive adhesive. *International Journal of Adhesion and Adhesives*, vol. 28, no. 7, p. 372-381, **DOI:10.1016/j.ijadhadh.2007.11.002**.

[24] Pressure-sensitive adhesive tape, from *https://www.3m.co.uk/3M/en_GB/company-uk/3m-products/~/3M-VHB-tape-4947/*, accessed on 2021-03-08.

[25] Pressure-sensitive adhesive tape, from *https://www.3mpolska.pl/3M/pl_PL/firma-pl/all-3m-products*, accessed on 2021-03-08.

[26] Pressure-sensitive adhesive tape, from *https://www.conrad.com/p/3m-40021915-industrial-tape-scotch-grey-l-x-w-15-m-x-19-mm-15-m-547078*, accessed on 2021-03-08.

[27] Peykova, Y., Lebedeva, O.V., Diethert, A., Müller-Buschbaum, P., Willenbacher, N. (2012). Adhesive properties of acrylate copolymers: effect of the nature of the substrate and copolymer functionality. *International Journal of Adhesion and Adhesives*, vol. 34, p. 107-116, **DOI:10.1016/j.ijadhadh.2011.12.001**.

[28] Dimas, D.A., Dallas, P.P., Rekkas, D.M., Choulis, N.H. (2000). Effect of several factors on the mechanical properties of pressure-sensitive adhesives used in transdermal therapeutic systems. *AAPS PharmSciTech*, vol. 1, p. 80-87, **DOI:10.1208/pt010216**.

[29] Poh, B.T., Kwo, H.K. (2007) Peel and shear strength of pressure-sensitive adhesives prepared from epoxidized natural rubber. *Journal of Applied Polymer Science*, vol. 105, no. 2, p. 680-684, **DOI:10.1002/app.26072**.

Strojniški vestnik - Journal of Mechanical Engineering 67(2021)7-8, 389-397

DOI:10.5545/sv-jme.2021.7262 Original Scientific Paper
Received for review: 2021-05-23
Received revised form: 2021-07-01
Accepted for publication: 2021-07-12

Characterization of the AZ31/AW-6060 Joint Fabricated using Compound Casting with a Zn Interlayer at Relatively Low Temperature Conditions

Tomasz Bucki[1,*] – Marek Konieczny[1] – Dana Bolibruchova[2] – Sylwia Rzepa[3]
[1]Kielce University of Technology, Faculty of Mechatronics and Mechanical Engineering, Poland
[2]University of Zilina, Faculty of Mechanical Engineering, Slovak Republic
[3]COMTES FHT a.s., Mechanical Testing and Thermophysical Measurement Department, Czech Republic

The work deals with the fabrication of a joint between AZ31 magnesium alloy and AW-6060 aluminium alloy with the use of a Zn interlayer. The Zn layer was produced on the surface of an AW-6060 alloy insert by diffusion bonding. The insert was then placed inside a steel mould and kept at room temperature. The joint was produced using compound casting by filling the mould with liquid AZ31 alloy, heated to 650 °C. The microstructure of the bonding zone formed between joined alloys was analysed using an optical microscope and a scanning electron microscope equipped with an energy dispersive X-ray spectroscope. The properties of the joint were examined using Vickers microhardness measurements and simple shear strength testing. As a result of the experiment, the 400 µm thick bonding zone with a complex microstructure was formed between the alloys. The microstructural analysis showed that the bonding zone reveals a high concentration of Zn and Mg. The layers of a eutectoid (a MgZn phase + a solid solution of Al and Zn in Mg), a $Mg_5Al_2Zn_2$ phase and a $Mg(Al,Zn)_2$ phase with fine particles of other phases were observed there. The bonding zone was characterized by relatively high microhardness, which was related to the brittleness of the constituents. The shear strength of the examined joint was 19.6 ± 2.5 MPa.

Keywords: compound casting, magnesium alloy, aluminium alloy, zinc interlayer, microstructure, mechanical properties

Highlights

- *The AZ31/AW-6060 joint was fabricated by compound casting with the use of a Zn interlayer.*
- *The Zn layer was produced on the surface of the AW-6060 alloy insert to act as an interlayer.*
- *The compound casting involved pouring the liquid AZ31 magnesium alloy at 650 °C onto a solid AW-6060 aluminium alloy insert placed in a steel mould and kept at room temperature.*
- *The study focused on the analysis of the microstructure and examinations of microhardness and shear strength of the fabricated joint.*

0 INTRODUCTION

In recent years, there has been a noticeable increase in the application of bimetallic elements based on various metals and their alloys. Such products have unique properties that cannot be achieved with a single alloy. A promising solution is the production of bimetals based on light alloys: magnesium and aluminium. The combination of these materials into one element allows taking the advantages of both alloys: the low density of the magnesium alloy and good resistance to corrosion and abrasion of the aluminium alloy [1] and [2]. The literature review shows that the following methods are used to join magnesium alloys with aluminium alloys: diffusion bonding [3], ultrasonic welding [4], resistance spot welding [5], friction stir welding [6]; explosive welding [7], tungsten inert gas (TIG), metal inert gas (MIG) and laser welding techniques [8] to [10], and compound casting [11].

The advantages of compound casting over other joining techniques include the possibility of producing joints with complex shapes, high efficiency, and a relatively simple and economical production process. The joining of magnesium to aluminium alloys by compound casting seems to be a promising direction that may contribute to the increase in the use of light alloys in various industries, mainly in the automotive industry. This technique involves pouring a liquid alloy onto a product made of a different material. The literature data [11] shows that joints with favourable properties can be fabricated by pouring liquid magnesium onto a solid aluminium insert placed in a casting mould. The typical bonding zone has a complex structure composed of continuous layers of Al_3Mg_2 (β) and $Mg_{17}Al_{12}$ (γ) intermetallic phases, as well as a layer of a eutectic (a $Mg_{17}Al_{12}$ phase + a solid solution of Al in Mg). Mg-Al intermetallic phases are characterized by high brittleness, related to the low strength of the joint and the brittle nature of the fracture. The thickness of the bonding zone depends on the parameters of the casting process, such as the temperature of molten magnesium and temperature of the mould with an aluminium insert [12], Mg-to-Al volume ratio [13] and [14], method of casting [15], and

*Corr. Author's Address: Kielce University of Technology, Faculty of Mechatronics and Mechanical Engineering, 25-314 Kielce, Poland, tbucki@tu.kielce.pl

pressure in the mould [16]. The research results on the properties of such joints show that favourable strength is achieved for the joints with a thin bonding zone. Some studies have focused on the fabrication of joints between Mg and Al alloys, e.g., AZ91/ A[illegible] [17] and [18], AZ91/ AlSi17 [19] and [20], AZ91/ AlSi12 [21], ZE41/ AlSi12 [22], AZ31/ AW-6060 [23]. The results of the above-mentioned works indicate that the presence of alloying elements may lead to significant modification of the structure of the created bonding zone and can affect the mechanical properties of the joint. The properties of the joint can also be improved by using interlayers. Such modification is meant to reduce or block the possibility of the formation of Mg-Al intermetallic phases and replace them with other phases with better properties. Recent studies showed that good results can be achieved when the Zn [23], Ni [24] or Ni + Cu [25] interlayers are used.

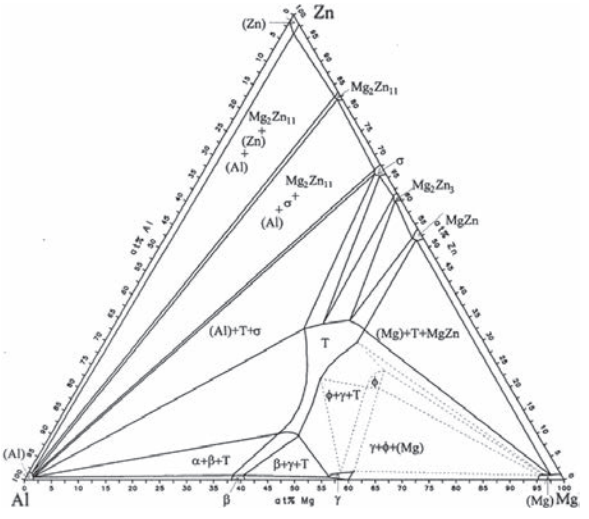

Fig. 1. *Isothermal cross-section of the Mg-Al-Zn phase diagram at the temperature of 25 °C* [29] *© MMMS and ASM Int.*

In order to understand the processes of formation of the Mg alloy/Al alloy joint with the use of a Zn interlayer, it is necessary to become acquainted with the Mg-Al [26], Mg-Zn [27] and Al-Zn [28] phase diagrams as well as the Mg-Al-Zn ternary diagram [29]. Fig. 1 shows the isothermal cross-section of the Mg-Al-Zn phase diagram at the temperature of 25 °C. The system, beyond the binary phases, also includes two ternary phases, marked as φ (also known as $Mg_5Al_2Zn_2$ [30]) and τ ($Mg_3(Al,Zn)_9$ [29]). The authors note that in all binary phases in the system, the solubility of the third element is low, except for the σ phase ($MgZn_2$). Due to the high solubility of Al in $MgZn_2$, this phase can also be stated as $Mg(Al,Zn)_2$. However, the results by Czerwinski [31] indicate that Zn atoms can replace some Al atoms in the $Mg_{17}Al_{12}$ phase. It can be then defined as $Mg_{17}(Al,Zn)_{12}$.

This work is a part of a larger project on the joining of Mg and Al alloys with the Zn interlayer by compound casting. In our previous paper [23], we focused on the effects of the Zn interlayer on the microstructure and properties of the joint formed between the AZ31 magnesium alloy and AW-6060 aluminium alloy. The research involved the formation of a 100 μm thick Zn layer on the surface of AW-6060 insert by diffusion bonding. The insert was next placed inside a steel mould and heated to 170 °C. Then the AZ31 alloy, heated to 680 °C, was poured into the mould. As a result, a continuous bonding zone with a thickness of 500 μm was formed between the alloys. The findings showed that the microstructure of the joint was complex. The layer of a eutectic (a $Mg_5Al_2Zn_2$ phase + a solid solution of Al and Zn in Mg), a layer of a $Mg_3(Al,Zn)_9$ phase, and a layer of a eutectic (a $Mg_3(Al,Zn)_9$ phase + a solid solution of Mg and Zn in Al) were detected in the bonding zone.

Furthermore, the bonding zone contained the fine particles of other phases, identified as $Mg_{17}Al_{12}$, Mg_2Si, $Al_6(Fe,Mn)$, and Al_5FeSi. The analysed joint was characterized by relatively high shear strength. The average shear strength was 24.3 ±2.8 MPa. The strength of the joint formed without an interlayer was much lower. The highest shear strength values (81 ±2.3 MPa) were noted for the joint produced with the following process parameters: pouring temperature 680 °C, mould temperature 300 °C. It was shown that the low strength and high brittleness of the analysed joint are correlated with the presence of brittle Mg-Al intermetallic phases in the bonding zone. In this case, the thickness of the bonding zone (approx. 400 μm) was lower than for the joint fabricated with the Zn interlayer, despite the use of a higher temperature of the insert.

The present paper deals with the fabrication of an AZ31/ AW-6060 joint by compound casting at temperature conditions significantly lower than those applied in our previous work. For this reason, an AW-6060 insert with a Zn surface layer with a steel mould was kept at room temperature. A greater reduction in the temperature of the insert would be inappropriate. Therefore, it was also decided to reduce the temperature of pouring of the AZ31 alloy. This alloy was thus heated to 640 °C and then poured into the mould. The study focuses on the microstructure analysis and examinations of microhardness and shear strength of the fabricated joint.

1 EXPERIMENTAL DETAILS

AZ31 magnesium alloy and AW-6060 aluminium alloy were used as the materials to be joined. The chemical compositions of the alloys are listed in Table 1.

Table 1. *Chemical compositions of AZ31 and AW-6060 alloys [at.%]*

Alloy	Mg	Al	Zn	Si	Mn
AZ31	bal.	3.07	1.05	-	0.31
AW-6060	0.45	bal.	-	0.50	0.19

The 60 mm in diameter and 10 mm thick specimens were cut from an AW-6060 alloy rod. After cutting, the specimens were subjected to grinding with abrasive papers up to 600 grit and to degreasing with ethanol. The Zn layer was formed on the surface of the AW-6060 alloy by diffusion bonding, by annealing the specimen in contact with a 100 μm thick Zn foil. The annealing was conducted in a vacuum furnace at 375 °C for 20 minutes. The pressure of 3 MPa was exerted to ensure good contact with the materials. The insert with Zn surface layer was next placed in a steel mould and kept at room temperature. The mould was then filled with liquid AZ31 alloy, heated to 680 °C under an inert argon atmosphere.

The specimens for microscopic observations were prepared using standard metallographic procedures. The final polishing was carried out using 0.05 μm colloidal silica. No etching was used due to the sufficient revealing of the microstructure of the specimens in contact with water. The microscopic observations were conducted with a Nikon ECLIPSE MA 200 optical microscope (OM) and a JEOL JSM-7100F scanning electron microscope equipped with an energy dispersive X-ray spectroscope detector (SEM/EDS).

The microhardness was tested by Vickers method, using a MATSUZAWA MMT Vickers microhardness tester at a load of 100 g.

The strength of the joints was examined by a simple shear test with a LabTest 5.20S P1 universal testing machine, using the setup described in the previous study [23]. The specimens with dimensions of 7 mm × 7 mm × 20 mm were cut from the central part of the joints. The shear strength was tested at a displacement of 10 mm/min.

2 RESULTS AND DISCUSSION

Fig. 2a presents the microstructure of the layer fabricated on the surface of AW-6060 alloy by diffusion bonding in contact with the 100 μm thick Zn foil. Microscopic analysis showed that diffusion processes during bonding resulted in forming a continuous joint between the materials used. As a result, Al and Zn form a simple phase diagram with no intermetallic phases [28]. The SEM observations at high magnification (Fig. 2b), together with the results of the EDS analysis (e.g., 3.16 at.% Zn, 78 at.% Al), suggested that the interface layer between the Zn and AW-6060 alloy had a lamellar microstructure and was composed of a solid solution of Al in Zn and a solid solution of Zn in Al.

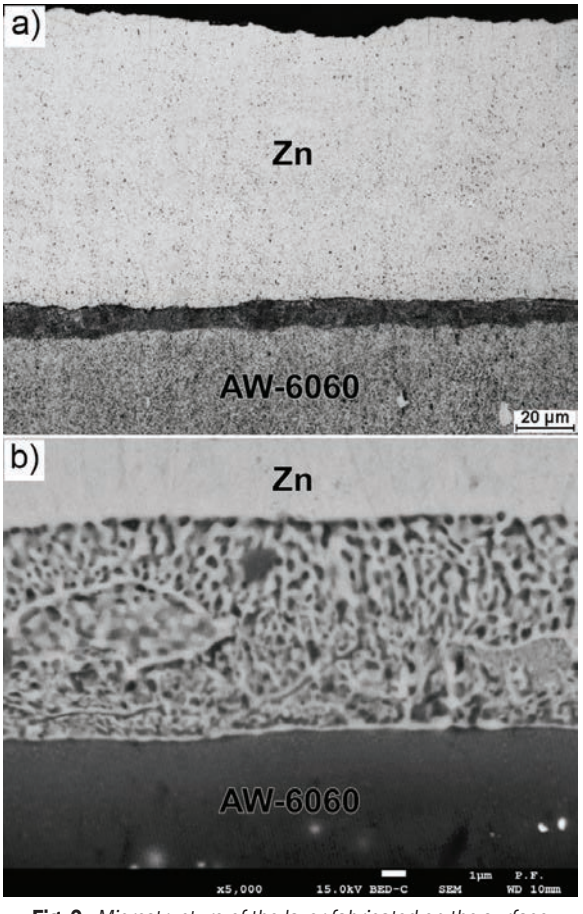

Fig. 2. *Microstructure of the layer fabricated on the surface of AW-6060 alloy by diffusion bonding in contact with the Zn foil; a) OM image, b) high magnification SEM image*

Fig. 3 shows the microstructure of the bonding zone formed by pouring the liquid AZ31 alloy at 680 °C onto the solid AW-6060 alloy insert with a Zn surface layer, which was kept at room temperature. The microscopic observations revealed that the joining process resulted in the formation of a continuous bonding zone with a complex structure. The overall thickness of the bonding zone was about 400 μm.

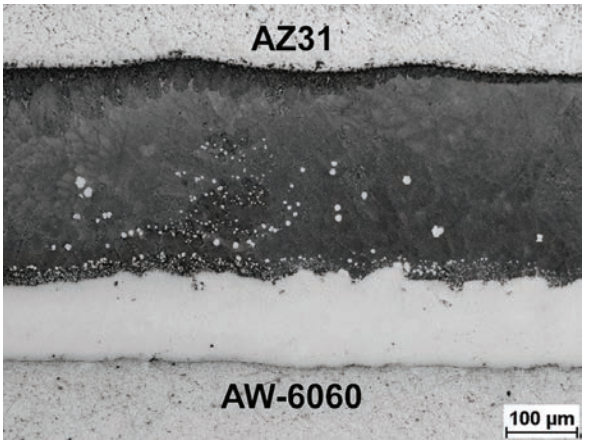

Fig. 3. *Microstructure of the bonding zone formed by pouring the liquid AZ31 alloy at 650 °C onto the solid AW-6060 alloy insert with a Zn surface layer, which was kept at room temperature*

Fig. 4 shows the results of an EDS linear analysis throughout the analysed bonding zone. The distribution of elements along the marked line shows a high content of Zn and Mg, while the concentration of Al was relatively low. The higher content of Al was recorded only in the transition region, which can be distinguished at the interface between the two characteristic layers of the bonding zone.

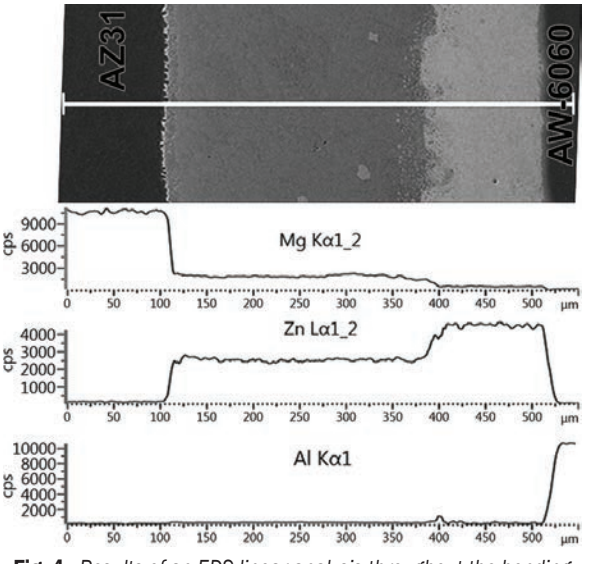

Fig. 4. *Results of an EDS linear analysis throughout the bonding zone formed between the AZ31 alloy and AW-6060 alloy with a Zn surface layer*

The details of the microstructure of the bonding zone observed in SEM are shown in Fig. 5. The results of EDS point analysis performed in marked points are presented in Table 2. The comparison of the result of analysis carried out in areas marked in Fig. 5 as 1 and 2 showed that the AZ31 alloy in the immediate vicinity of the bonding zone was enriched with Zn. The layer of the bonding zone at the AZ31 alloy side was characterized by a two-phase microstructure. The analysis results carried out in points 3 and 4 suggested that this region was composed of a eutectoid containing a MgZn intermetallic phase and a solid solution of Al and Zn in Mg. The chemical composition of the highly dispersed two-phase area (marked as 5) also indicated a eutectoid (a MgZn phase + a solid solution of Al and Zn in Mg). In the transition region, which was observed in the central part of the bonding zone, light particles with high content of Mg, Zn, and Al were located (point 6 in Fig. 5). The composition of these particles indicated a $Mg_5Al_2Zn_2$ ternary phase. The analysis carried out in point 7 showed that the chemical composition of the region observed below the eutectoid is also close to a $Mg_5Al_2Zn_2$ phase. In the next layer of the bonding zone (analysis in point 8), a light matrix was observed. Its chemical composition indicated a $Mg(Al,Zn)_2$ phase. In the structure of this region, fine particles of other phases were also distributed. The results of microscopic observations showed that the particles marked as 9 have a two-phase structure. The small size of these particles made it impossible to perform quantitative analysis in single phases. The result of the analysis in point 9 and the high magnification image presented in Fig. 5 suggests that these particles may be composed of a eutectic containing a $Mg(Al,Zn)_2$ phase and a solid solution of Mg and Zn in Al.

The high content of Mg and Si in particles marked as 10 indicated that the darker particles were composed of a Mg_2Si intermetallic phase, which may originate from the AW-6060 alloy. It can also be formed as a result of diffusion processes between the elements present in the alloys. For example, in [17] and [18], the authors showed that pouring of Mg alloy onto the Si-containing Al alloy insert resulted in the formation of fine particles of the Mg_2Si phase in the bonding zone. The results of the analysis in the area marked as 11 in Fig. 5 showed that the bonding zone on the AW-6060 alloy side also consisted of a $Mg(Al,Zn)_2$ phase with some particles of other phases. Throughout the bonding zone, the light particles containing Al, Fe and Mn or Al, Si and Fe were also found (e.g., 8.56 at.% Al, 7.90 at.% Fe, 2.53 at.% Mn or 8.26 at.% Al, 13.47 at.% Si, 8.27 at.% Fe, respectively). They probably were particles of multicomponent phases originating from the AW-6060 alloy.

Fig. 6 illustrates the effects of microhardness measurements in AZ31 and AW-6060 alloys and in the bonding zone formed between them. The results

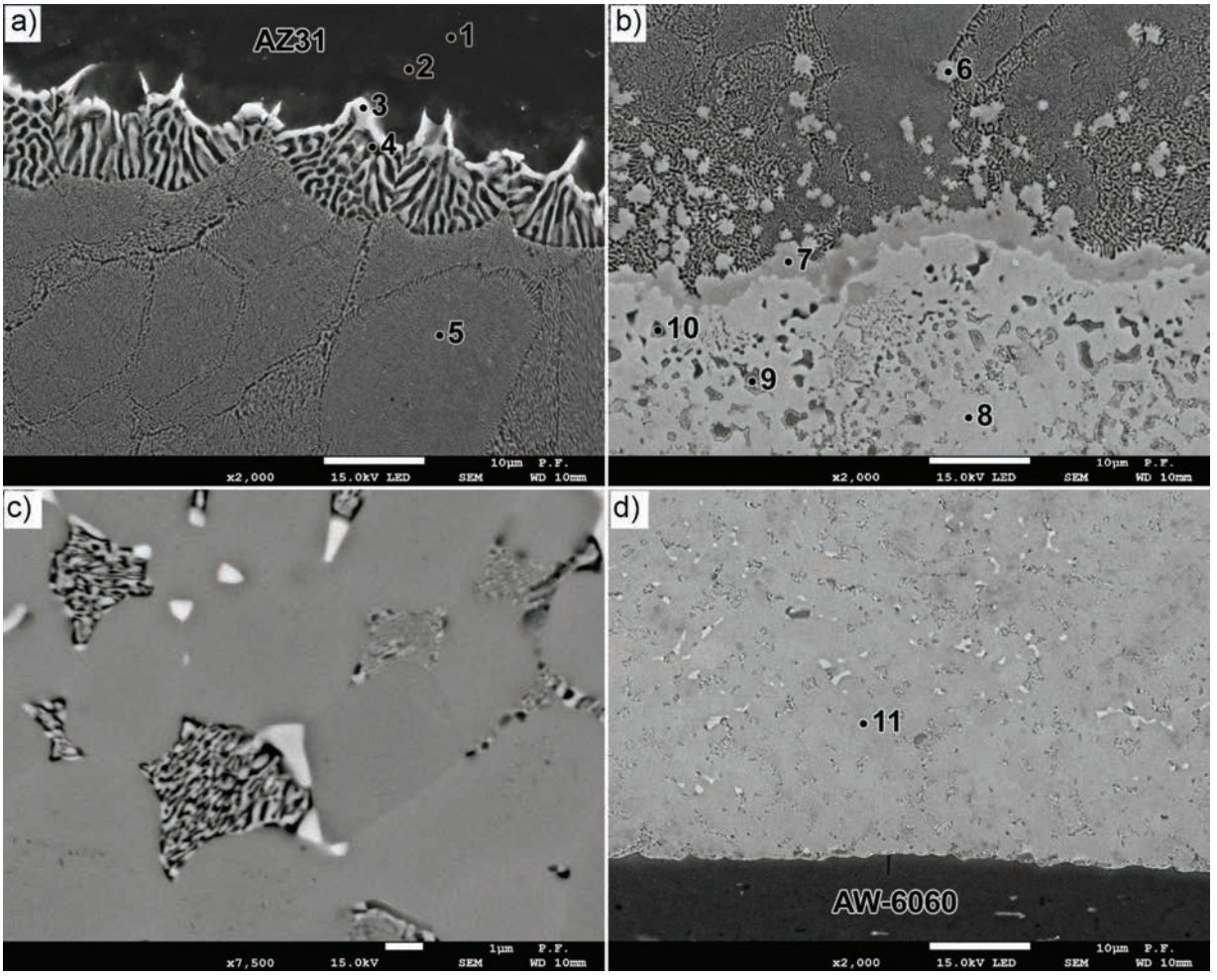

Fig. 5. *Details of the microstructure of bonding zone; a) region close to AZ31 alloy, b) the central region, c) high magnification image of the light matrix observed in the central region, d) region close to AW-6060 alloy*

showed that a relatively high hardness characterizes the bonding zone. The layer with a two-phase structure (a MgZn phase + a solid solution of Zn and Al in Mg), which was observed on the AZ31 alloy side, had a microhardness in the range from 214 HV0.1 to 225 HV0.1. The microphotography presented in Fig. 6 shows that the measurements in this region did not lead to the formation of cracks. In the transition region containing a $Mg_5Al_2Zn_2$ phase (Fig. 6), a higher microhardness was noted. In this area, the cracks propagating from the corners of Vickers tester impressions were observed. The presence of fine cracks indicates a certain brittleness of this area. The highest microhardness (3 1.5 HV0.1 to 299 HV0.1) was reported in the region adjacent to the AW-6060 alloy, which consisted of a $Mg(Al,Zn)_2$ phase and particles of other phases. Fig. 6 shows that the microhardness measurements in this region also resulted in the formation of fine cracks indicating the brittleness of the phases.

Table 2. *Results of the EDS analysis at points marked in Fig. 5 (at.%)*

Point	Mg	Al	Zn	Si
1	96.40	3.03	0.57	-
2	93.71	4.46	1.83	-
3	51.13	2.58	46.29	-
4	90.99	5.81	3.20	-
5	68.79	5.75	25.46	-
6	57.93	17.79	24.28	-
7	56.14	18.42	25.44	-
8	32.63	2.88	64.49	-
9	27.66	15.15	57.19	-
10	66.14	1.14	0.98	31.74
11	30.98	5.59	63.43	-

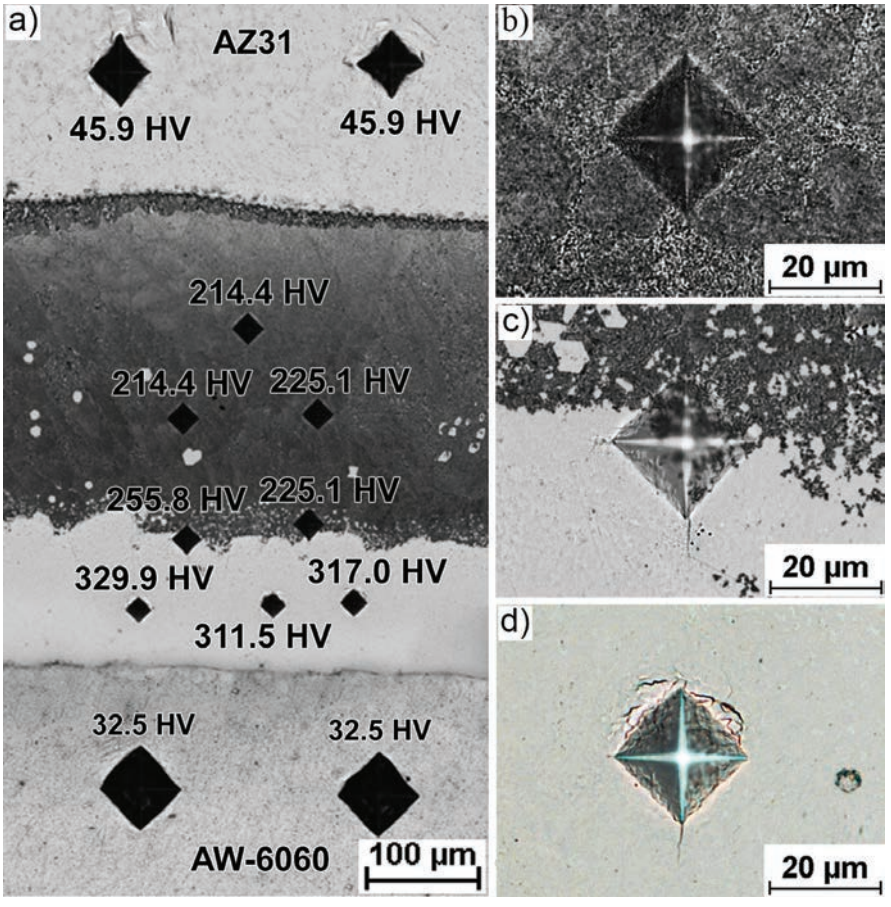

Fig. 6. *Results of Vickers microhardness measurements in the bonding zone; a) low magnification image, high magnification of the indentation left in: b) the region close to AZ31 alloy, c) the central region, d) the region close to AW-6060 alloy*

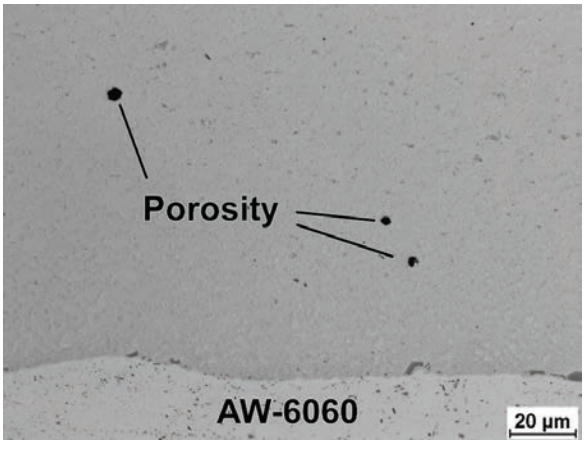

Fig. 7. *Details of the microstructure with fine pores locally distributed throughout the bonding zone*

From the study it is apparent that as a result of compound casting, a continuous bonding zone with no macroscopic defects was formed between the AZ31 alloy and AW-6060 alloy with a Zn surface layer. The microscopic observations revealed that only fine pores could be found locally in the bonding zone, as shown in Fig. 7

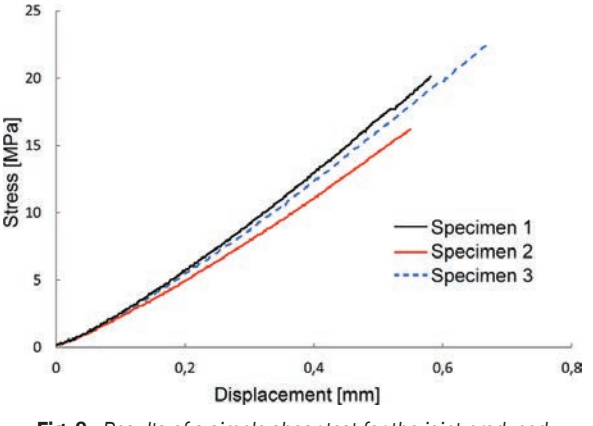

Fig. 8. *Results of a simple shear test for the joint produced between the AZ31 alloy and AW-6060 alloy with a Zn surface layer*

Fig. 8 presents the results of a simple shear test performed for the analysed joint. The average shear strength of the tested specimens was 19 ±2.5 MPa. The shape of the stress-displacement curves was typical of brittle materials. No symptoms of plastic deformation were observed.

A comparative analysis of the presented results and the findings from our previous work [23] allowed us to conclude that using a Zn interlayer may result in substantial changes in the microstructure of the AZ3 / AW-0 joint produced by compound casting at a wide range of process parameters. The use of the Zn interlayer permitted a significant reduction in the pouring temperature and the temperature of the insert. The presence of Zn also limited the formation of Mg-Al binary phases and led to the creation of phases containing Zn. In addition, the bonding zone in the joint formed with the Zn interlayer, which was analysed in the present study, was characterized by higher microhardness and better shear strength in comparison to the direct joint. This phenomenon is worth highlighting because the high hardness of such materials typically corresponds with their brittleness and low strength. The results of the present research showed, however, that the Mg-Al intermetallic phases present in the direct joint were characterized by high brittleness, as indicated by significant cracks at the corners of the indentations left by the microhardness tester. Some cracks were also observed for the joint with Zn interlayer, but the crack dimensions were much smaller despite the higher hardness.

Important insights can be drawn when comparing the joints produced with the Zn interlayer at different pouring temperatures and Al alloy insert temperatures. The results show that depending on the temperature conditions, the diffusion of the elements occurs at different rates. The higher temperature led to the greater content of Al in the bonding zone, while for the joint produced at the lower temperature, the amount of Al remained low. It results in significant differences in the phase composition of the bonding zone. The results of the study are in good agreement with the Mg-Al-Zn phase diagram. The greater content of Al in the first case resulted in the formation of phases rich in Mg, Al, and Zn, while the lower content of Al in the other bonding zone led to the presence of phases rich in Mg and Zn. Furthermore, the joint made at a higher temperature was characterized by the lowest brittleness and the highest shear strength among all analysed variants.

3 CONCLUSIONS

The AZ3 / AW-0 joint was fabricated by the compound casting process. A 100 μm Zn layer was produced on the surface of the insert to act as an interlayer. The compound casting involved pouring the liquid AZ3 magnesium alloy at 6 °C onto a solid AW-0 aluminium alloy insert with a Zn layer, which was placed in a steel mould and kept at room temperature.

As a result of the experiment, a continuous, a 0 μm thick layer was formed between the alloys. The bonding zone has a complex structure. On the AZ3 alloy side, it was composed of a eutectoid containing a MgZn intermetallic phase and a solid solution of Al and Zn in Mg. In the central part of the bonding zone, the particles of a $Mg_5Al_2Zn_2$ ternary intermetallic phase and the thin layer of this phase were observed. The region adjacent to the AW-0 alloy consisted of a $Mg(Al,Zn)_2$ phase matrix with fine particles, whose composition indicated that they were the particles of a Mg_2Si phase, a eutectic (a $Mg(Al,Zn)_2$ phase, and a solid solution of Mg and Zn in Al) and multicomponent phases rich in Al, Fe and Mn or Al, Fe and Si.

The bonding zone was characterized by higher microhardness than that of the joined alloys. The highest microhardness values were observed in the region containing a $Mg(Al,Zn)_2$ phase and in the layer composed of a $Mg_5Al_2Zn_2$ phase. The microhardness measurements in these areas led to the propagation of small cracks in the vicinity of Vickers tester indenters. Observed cracks indicate a noticeable brittleness of the phases. The average shear strength of the joint was 19 ±2.5M Pa.

4 REFERENCES

[1] Kumar, D.S., Phanden, R.K., Thakur, L. (2021). A review on environment friendly and lightweight Magnesium-Based metal matrix composites and alloys. *Materials Today: Proceedings*, vol. 38, p. 359-364, **DOI:10.1016/j.matpr.2020.07.424**.

[2] Ahmad, A., Yunxin, W., Hai, G., Lei, L. (2019). Determination of the effect of cold working compression on residual stress reduction in quenched aluminium alloy 2219 block. *Strojniški vestnik - Journal of Mechanical Engineering*, vol. 65, no. 5, p. 311-318, **DOI:10.5545/sv-jme.2018.5938**.

[3] Zhang, J., Luo, G., Wang, Y., Xiao, Y., Shen, Q., Zhang, L. (2013). Effect of Al thin film and Ni foil interlayer on diffusion bonded Mg-Al dissimilar joints. *Journal of Alloys and Compounds*, vol. 556, p. 139-142, **DOI:10.1016/j.jallcom.2012.12.106**.

[4] Patel, V.K., Bhole, S.D., Chen, D.L. (2012). Microstructure and mechanical properties of dissimilar welded Mg-Al joints by ultrasonic spot welding technique. *Science and Technology of*

Welding and Joining, vol. 17, no. 3, p. 202-206, **DOI:10.1179/1362171811Y.0000000094**.

[5] Hayat, F. (2011). The effects of the welding current on heat input, nugget geometry, and the mechanical and fractural properties of resistance spot welding on Mg/Al dissimilar materials. *Materials & Design*, vol. 32, no. 4, p. 2476-2484, **DOI:10.1016/j.matdes.2010.11.015**.

[6] Zettler, R., Da Silva, A.A.M., Rodrigues, S., Blanco, A., Dos Santos, J.F. (2006). Dissimilar Al to Mg alloy friction stir welds. *Advanced Engineering Materials*, vol. 8, no. 5, p. 415-421, **DOI:10.1002/adem.200600030**.

[7] Mróz, S., Mola, R., Szota, P., Stefanik, A. (2020). Microstructure and properties of 1050A/AZ31 bimetallic bars produced by explosive cladding and subsequent groove rolling process. *Archives of Civil and Mechanical Engineering*, vol. 20, p. 1-15, **DOI:10.1007/s43452-020-00084-4**.

[8] Liu, F., Zhang, Z., Liu, L. (2012). Microstructure evolution of Al/Mg butt joints welded by gas tungsten arc with Zn filler metal. *Materials Characterization*, vol. 69, p. 84-89, **DOI:10.1016/j.matchar.2012.04.012**.

[9] Zhang, H.T., Song, J.Q. (2011). Microstructural evolution of aluminum/magnesium lap joints welded using MIG process with zinc foil as an interlayer. *Materials Letters*, vol. 65, no. 21-22, p. 3292-3294, **DOI:10.1016/j.matlet.2011.05.080**.

[10] Scherm, F., Bezold, J., Glatzel, U. (2012). Laser welding of Mg alloy MgAl3Zn1 (AZ31) to Al alloy AlMg3 (AA5754) using ZnAl filler material. *Science and Technology of Welding and Joining*, vol. 17, no. 5, p. 364-367, **DOI:10.1179/1362171812X13333824902080**.

[11] Hajjari, E., Divandari, M., Razavi, S.H., Emami, S.M., Homma, T., Kamado, S. (2011). Dissimilar joining of Al/Mg light metals by compound casting process. *Journal of Materials Science*, vol. 46, p. 6491-6499, **DOI:10.1007/s11431-008-0345-9**.

[12] Mola, R., Bucki, T., Dziadoń, A. (2016). Formation of Al-alloyed layer on magnesium with use of casting techniques. *Archives of Foundry Engineering*, vol. 16, no. 1, p. 112-116, **DOI:10.1515/afe-2016-0013**.

[13] Emami, S.M., Divandari, M., Arabi, H., Hajjari, E. (2013). Effect of melt-to-solid insert volume ratio on Mg/Al dissimilar metals bonding. *Journal of Materials Engineering and Performance*, vol. 22, p. 123-130, **DOI:10.1007/s11665-012-0243-y**.

[14] Jiang, W., Fan, Z., Li, G., Yang, L., Liu, X. (2016). Effects of melt-to-solid insert volume ratio on the microstructures and mechanical Properties of Al/Mg bimetallic castings produced by lost foam casting. *Metallurgical and Materials Transactions A*, vol. 47, p. 6487-6497, **DOI:10.1007/s11661-016-3788-9**.

[15] Emami, S.M., Divandari, M., Hajjari, E., Arabi, H. (2013). Comparison between conventional and lost foam compound casting of Al/Mg light metals. *International Journal of Cast Metals Research*, vol. 26, no. 1, p. 43-50, **DOI:10.1179/1743133612Y.0000000037**.

[16] Li, G., Yang, W., Jiang, W., Guan, F., Jiang, H., Wu, Y., Fan, Z. (2019). The role of vacuum degree in the bonding of Al/Mg bimetal prepared by a compound casting process. *Journal of Materials Processing Technology*, vol. 265, p. 112-121, **DOI:10.1016/j.jmatprotec.2018.10.010**.

[17] Li, G., Jiang, W., Yang, W., Jiang, Z., Guan, F., Jiang, H., Fan, Z. (2019). New insights into the characterization and formation of the interface of A356/AZ91D bimetallic composites fabricated by compound casting. *Metallurgical and Materials Transactions A*, vol. 50, p. 1076-1090, **DOI:10.1007/s11661-018-5022-4**.

[18] Jiang, W., Li, G., Fan, Z., Wang, L., Liu, F. (2016). Investigation on the interface characteristics of Al/Mg bimetallic castings processed by lost foam casting. *Metallurgical and Materials Transactions A*, vol. 47, p. 2462-2470, **DOI:10.1007/s11661-016-3395-9**.

[19] Mola, R., Bucki, T., Dziadoń, A. (2017). Effects of the pouring temperature on the formation of the bonding zone between AZ91 and AlSi17 in the compound casting process. *IOP Conference Series: Materials Science and Engineering*, vol. 179, p. 1-6, **DOI:10.1088/1757-899X/179/1/012053**.

[20] Mola, R., Bucki, T. (2018). The microstructure and properties of the bimetallic AZ91/AlSi17 joint produced by compound casting. *Archives of Foundry Engineering*, vol. 18, no. 1, p. 71-76, **DOI:10.24425/118814**.

[21] Mola, R., Bucki, T. (2020). Characterization of the Bonding zone in AZ91/AlSi12 bimetals fabricated by liquid-solid compound casting using unmodified and thermally modified AlSi12 alloy. *Strojniški vestnik - Journal of Mechanical Engineering*, vol. 66, no. 7-8, p. 439-448, **DOI:10.5545/sv-jme.2020.6703**.

[22] Mola, R., Bucki, T. (2018). Characterization of the bonding zone in a ZE41/AlSi12 joint fabricated by liquid-solid compound casting. *Archives of Foundry Engineering*, vol. 18, no. 2, p. 203-208, **DOI:10.24425/122529**.

[23] Mola, R., Bucki, T., Gwoździk, M. (2019). The effect of a zinc interlayer on the microstructure and mechanical properties of a magnesium alloy (AZ31)–aluminum alloy (6060) joint produced by liquid–solid compound casting. JOM, vol. 71, p. 2078-2086, **DOI:10.1007/s11837-019-03405-y**.

[24] Li, G., Jiang, W., Guan, F., Zhu, J., Yu, Y., Fan, Z. (2020). Effect of different Ni interlayers on interfacial microstructure and bonding properties of Al/Mg bimetal using a novel compound casting. Journal of Manufacturing Processes, vol. 50, p. 614-628, **DOI:10.1016/j.jmapro.2020.01.017**.

[25] Li, G., Jiang, W., Guan, F., Zhu, J., Zhang, Z., Fan, Z. (2021). Microstructure, mechanical properties and corrosion resistance of A356 aluminum/AZ91D magnesium bimetal prepared by a compound casting combined with a novel Ni-Cu composite interlayer. *Journal of Materials Processing Technology*, vol. 288, p. 1-12, **DOI:10.1016/j.jmatprotec.2020.116874**.

[26] Okamoto, H. (1998). Al-Mg (aluminum-magnesium). *Journal of Phase Equilibria*, vol. 19, p. 598, **DOI:10.1361/105497198770341815**.

[27] Okamoto, H. (1995). Mg-Zn (magnesium-zinc). *Journal of Phase Equilibria*, vol. 16, p. 474-475, **DOI:10.1007/BF02645363**.

[28] Okamoto, H. (1995). Al-Zn (aluminum-zinc). Journal of Phase Equilibria, vol. 16, p. 281-282, **DOI:10.1007/BF02667316**.

[29] Liang, H., Chen, S.-L., Chang, Y.A. (1997). A thermodynamic description of the Al-Mg-Zn system. *Metallurgical and Materials Transactions A*, vol. 28, p. 1725-1734, **DOI:10.1007/s11661-997-0104-8**.

[30] Cheng, K., Sun, J., Xu, H., Wang, J., Zhou, J., Tang, S., Wang, X., Zhang, L., Du, Y. (2021). On the temperature-dependent diffusion growth of Φ-Mg5Al2Zn2 ternary intermetallic compound in the Mg-Al-Zn system. *Journal of Materials Science*, vol. 56, p. 3488-3497, **DOI:10.1007/s10853-020-05439-z**.

[31] Czerwinski, F. (2002). The oxidation behaviour of an AZ91D magnesium alloy at high temperatures. *Acta Materialia*, vol. 50, no. 10, p. 2639-2654, **DOI:10.1016/S1359-6454(02)00094-0**.

Vsebina

Strojniški vestnik - Journal of Mechanical Engineering
letnik 67, (2021), številka 7-8
Ljubljana, julij-avgust 2021
ISSN 0039-2480

Izhaja mesečno

Razširjeni povzetki (extended abstracts)

Strojniški vestnik - Journal of Mechanical Engineering 67(2021)7-8, SI 45

Prejeto v recenzijo: 2021-03-20
Prejeto v recenzijo: 2021-05-18
Odobreno za objavo:2021-06-17

Ultranatančno točkovno diamantno struženje kompleksne sinusoidne površine z aktivnim nadzorom točnosti obdelave

Peixing Ning[1] – Ji Zhao[1,2,*] – Shijun Ji[1] – Jingjin Li[1] – Handa Dai[1]
[1]Univerza v Jilinu, Šola za strojništvo in letalsko tehniko, Kitajska
[2]Severovzhodna univerza, Šola za strojništvo in avtomatizacijo, Kitajska

Točkovno struženje z diamantnim orodjem (SPDT) v kombinaciji s tehnologijo Slow Tool Servo (STS) je najbolj razširjena tehnika izdelave optičnih modulov. Priprava poti orodja je prvi in ključni korak, ki ima velik vpliv na topografijo in kakovost površin izdelka po obdelavi. Dosedanje raziskave tehnologije ultranatančne obdelave kompleksnih optičnih površin so bile usmerjene predvsem v pripravo poti orodja, kompenzacijo radija zaokrožitev in analizo topografije obdelanih površin. Le malo pa je študij na temo priprave poti orodja za doseganje točnosti obdelave. V članku je predstavljena metoda priprave poti orodja na osnovi aktivnega nadzora točnosti obdelave (MAAC), ki učinkovito zagotavlja zahtevano točnost obdelave. Pri tehnologiji SPDT se uporablja kombinacija rotacijskega gibanja vretena in linearnega recipročnega gibanja. Vrtenje vretena in recipročno gibanje po osi *Z* povzročata napako tetive v smeri rezanja, linearno gibanje v smeri *X* pa preostalo napako v smeri podajanja. Preučena je bila odvisnost med potjo orodja in napako obdelave ob upoštevanju omenjenih glavnih virov napak. V članku sta podrobneje predstavljena kompenzacija radija zaokrožitev ter izračun napake tetive in preostale napake. Pot orodja, ki izpolnjuje zahteve glede točnosti obdelave, je tako mogoče izpeljati po obratnem postopku izračuna napake.

Za preverjanje učinkovitosti predlagane metode sta bila opravljena simulacija napak obdelave in eksperiment z obdelavo kompleksne sinusoidne površine. Mejna vrednost preostale napake Δ_{res} in napake tetive Δ_{cho} je bila nastavljena na 0,5 μm. Za načrtovanje poti orodja, ki prinaša oblikovano površino, je bila uporabljena metoda priprave poti orodja na podlagi MAAC. Simulacija napak obdelave je bila izvedena po obratnem postopku zgornjega izračuna poti orodja. Ugotovljeno je bilo, da so vse napake znotraj 0,5 μm. Za dokazovanje učinkovitosti predlaganega pristopa pri realni obdelavi je bil opravljen eksperiment na stroju Nanoform 2θ za SPDT. Obdelana površina je bila izmerjena z optičnim profilometrom na belo svetlobo Zygo newview 9000. Zaradi omejitev merilnega vidnega polja je bilo naključno izbranih osem predelov obdelane površine različnega polmera, vključno z vrhovi, dolinami in vmesnimi območji. Preostala napaka in napaka tetive sta povezani, zato ju je težko meriti in analizirati ločeno. Kakovost obdelave površin je mogoče ocenjevati z največjo višino profila (PV) obdelane površine. Rezultati meritev po izključitvi naključnih napak so pokazali, da je celotno odstopanje (dejanska vrednost PV) obdelane kompleksne sinusoidne površine približno 2,459 μm. Vrednost ne odstopa signifikantno od vnaprej določene vrednosti PV = 2 μm. Ti rezultati so dokazali, da je metoda MAAC primerna za pripravo poti orodja.

Predstavljena metoda je prispevek k raziskavam nadzora točne obdelave kompleksnih površin s tehnologijo SPDT. Obstajajo pa še drugi dejavniki, ki jih ni mogoče nadzorovati – merilne napake, napake obdelovalnega stroja, obraba orodja in delovna temperatura – zaradi katerih dejanska vrednost PV nekoliko presega vnaprej določeno vrednost PV. V prihodnje bo treba preučiti tudi vpliv teh dejavnikov na napake obdelave površin za doseganje zahtevane točnosti.

Ključne besede: aktivni nadzor točnosti obdelave (MAAC), napovedovanje napake obdelave, kompleksna sinusoidna površina, točkovno struženje z diamantnim orodjem (SPDT)

*Naslov avtorja za dopisovanje: Univerza v Jilinu, Šola za strojništvo in letalsko tehniko, Kitajska, jzhao@jlu.edu.cn

Strojniški vestnik - Journal of Mechanical Engineering 67(2021)7-8, SI 46

Prejeto v recenzijo: 2021-04-08
Prejeto popravljeno: 2021-06-09
Prejeto popravljeno: 2021-07-01

Osnovna teorija in metoda za konstruiranje linijskih zobniških mehanizmov z variabilnim kotom gredi

Yang-zhi Chen[1,*] – Chao He[1] – Yue-ling Lyu[2]

[1]Fakulteta za strojništvo in avtomobilsko tehniko, Tehniška univerza Južne Kitajske, Kitajska
[2]Univerza Sun Yat-sen, Yueling Lyu, Fakulteta za biomedicinski inženiring, Kitajska

V članku je predstavljen nov linijski zobniški mehanizem z variabilnim kotom gredi (VSALGM). Mehanizem VSALGM ima dve rotacijski prostostni stopnji: prva je vrtenje zobniške dvojice s konstantnim prestavnim razmerjem, druga pa predstavlja relativni zasuk gredi. Mehanizem je tako primeren za aplikacije, ki zahtevajo konstantno prestavno razmerje in dve prostostni stopnji.

Najprej je podan predlog novega kontaktnega modela VSALGM, ki ga sestavljata ena gnana kontaktna krivulja in ena gonilna delovna površina linijskega zobnika (DLTWS). Površino DLTWS sestavlja množica gonilnih kontaktnih krivulj.

Na osnovi teorije prostorske ubirnice linijskih zobnikov so bile izpeljane osnovne enačbe za konstruiranje po kontaktnem modelu VSALGM. Ker ubirni kot pomembno vpliva na učinkovitost zobniškega prenosnika, je bil narejen primer izračuna ubirnega kota na osnovi kontaktnega modela VSALGM. Rezultati izračunov kažejo, da lahko pri nekaterih kombinacijah parametrov nastopi blokada oziroma nezmožnost vrtenja zobniške dvojice. Zato je bil analiziran in predlagan kriterij ubirnega kota VSALGM na osnovi kontaktnega modela. Iz tega je bila izpeljana osnovna metoda za konstruiranje VSALGM. Podan je tudi primer konstrukcije zobniške dvojice na osnovi zgornjega primera izračuna ubirnega kota, na podlagi katerega so bili 3D-natisnjeni prototipi.

Za preizkus delovanja VSALGM je bilo zgrajeno kinematično preizkuševališče, ki omogoča spreminjanje kota gredi. Na njem so bile opravljene tri skupine kinematičnih eksperimentov s prototipi, v vsaki skupini pa so bili zajeti testi s fiksnim in zvezno spremenljivim kotom gredi. Skupine so se razlikovale po obremenitvah. Nato so bili izvedeni še preizkusi kontaktnih površin zobnikov. Rezultati kinematičnih eksperimentov so dokazali, da ima VSALGM dve prostostni stopnji in da zagotavlja gladek prenos tudi med konstantnim spreminjanjem kota gredi. Iz analize kontaktnih površin sledi ugotovitev, da različne gonilne kontaktne krivulje pri različnih kotih gredi VSALGM ubirajo z vedno isto gnano kontaktno krivuljo. Analiza napak prenosa VSALGM v kinematičnih eksperimentih je pokazala, da so le-te predvsem posledica napak instrumenta in testnih prototipov. Trenutno bi bilo zaradi nizke natančnosti eksperimentalne opreme težko analizirati točnost montaže zobnikov.

V prihodnje bodo razviti natančno preizkuševališče in natančni linijski zobniki za analizo napak prenosa in dinamične zmogljivosti VSALGM. Rezultati eksperimentov so pokazali, da se napaka prenosa povečuje z obremenitvijo. Zdajšnji mehanizmi VSALGM so primerni le za manjše obremenitve. Njihova konstrukcija bo v prihodnje izpopolnjena za povečanje obremenljivosti.

VSALGM ima v primerjavi s predhodnimi rešitvami tovrstnih zobniških dvojic dve prostostni stopnji ter zagotavlja gladek prenos tudi med konstantnim spreminjanjem kota gredi.

Ključne besede: linijski zobnik, variabilen kot gredi, prostostna stopnja, ubirni kot, teorija prostorske ubirnice, kinematični eksperiment, zobniški prenos

*Naslov avtorja za dopisovanje: Tehniška univerza Južne Kitajske, Fakulteta za strojništvo in avtomobilsko tehniko, Guangzhou, Kitajska, meyzchen@scut.edu.cn

Strojniški vestnik - Journal of Mechanical Engineering 67(2021)7-8, SI 47

Prejeto v recenzijo: 2021-02-21
Prejeto popravljeno: 2021-05-11
Odobreno za objavo: 2021-06-21

Napoved nosilnosti in tribološke trajnosti drsnih ležajev

Myron Chernets[1] – Marek Opielak[2] – Anatolii Kornienko[1,*] – Oleg Radko[3]
[1]Nacionalna univerza za letalstvo, Fakulteta za letalski in vesoljski inženiring, Ukrajina
[2]Tehniška univerza v Lublinu, Poljska
[3]Nacionalna univerza za obrambo Ivana Černjahovskega, Ukrajina

Uporaba drsnih ležajev ima pomembno vlogo pri tehničnih aplikacijah, kjer uporaba kotalnih ležajev ni možna oz. praktična. Za njihove delovne naloge so značilne zelo različne obremenitve, premeri gredi, vrtilne frekvence, širine in uporabljeni materiali. Ti ležaji obratujejo v različnih delovnih pogojih ter v prisotnosti fluidov (plinov), mejnega trenja in tudi v pogojih suhega trenja.

Metode za izračun trajnosti tovrstnih ležajev iz literature se v praksi niso uveljavile zaradi uporabe Archardovega zakona abrazivne obrabe, ki ne nastopa v pogojih mejnega trenja. Pri projektiranju drsnih ležajev se pogosto uporabljajo izračuni na osnovi povprečnega tlaka p in Zeinerjevega kriterija pv. Poenostavitev pri računanju nosilnosti na osnovi tlaka p je velik približek. Velikost kontaktnega tlaka ni odvisna le od obremenitve in od premera gredi, temveč v veliki meri tudi od radialne zračnosti ležaja in od elastičnosti materialov. Omenjeni kriteriji ne upoštevajo omenjenih dveh dejavnikov. V fazi konstruiranja prav tako ni vključeno napovedovanje obrabe drsnih ležajev. Ustrezna metoda za izračun ležajev mora temeljiti na kontaktnih problemih teorije elastičnosti za cilindrična telesa podobnih polmerov ob upoštevanju mehanizma obrabe s tornim utrujanjem.

Pričujoči članek predstavlja novo analitično metodo na področju teorije elastičnosti, ki omogoča računanje kontaktne trdnosti in življenjske dobe drsnih ležajev. Metoda temelji na avtorjevi metodologiji za preučevanje kinetike torno-utrujenostnega loma materialov v triboloških sistemih pri pogojih drsnega trenja. Predstavljen je tribokinetični matematični model obrabe, metode za računanje začetnega kontaktnega tlaka in njihova transformacija zaradi obrabe ležajnih elementov, kakor tudi izračun življenjske dobe ležajev do maksimalne linearne obrabe puše. Na podlagi rezultatov numerične simulacije je bil preučen vpliv obremenitve in radialne zračnosti na izhodiščne kontaktne tlake in njihovo zmanjševanje zaradi obrabe. Izdelana je bila računska ocena življenjske dobe ležaja. Ugotovljene so bile kvalitativne in kvantitativne odvisnosti sprememb parametrov kontakta in trajnosti od obremenitve, kotne hitrosti gredi ter radialne zračnosti ležaja.

Metoda omogoča izračun trajnosti ležajev z dovoljeno obrabo puše ter določitev obrabe puše in gredi v določenem obratovalnem obdobju. Predstavljena je zaprta oblika rešitve problema tribološkega kontakta za praktično uporabo s preprostimi programskimi orodji, zlasti s programom Microsoft Excel. Razvita metoda je uporabna brez omejitev za preračun kovinskih ležajev, tudi v prisotnosti različnih prevlek (zaščitnih, za zmanjšanje trenja, obrabno obstojnih). Metoda veliko obeta tudi pri hibridnih (kovinsko-polimernih) ležajih, ki so izdelani iz materialov z znatno različnimi lastnostmi. Postopki konstruiranja za take ležaje še ne obstajajo.

Predstavljena metoda za računsko napovedovanje zmogljivosti drsnih ležajev omogoča kakovosten in učinkovit izračun kontaktne trdnosti in tribološke trajnosti v inženirski praksi. Metoda zagotavlja optimizacijo kriterijev kontaktne trdnosti, obrabne obstojnosti in trajnosti ter izbiro optimalnih materialov pri konstruiranju ležajev. Rešitve tovrstnih problemov kontaktne obrabe omogočajo tudi ocenjevanje napak pri numeričnih izračunih. Metoda ima znanstveno vrednost na področju tribologije, teoretično vrednost na področju tribomehanike in praktično vrednost na področju tribotehnike.

Ključne besede: drsni ležaj, problem kontaktne obrabe, parametri kontakta in tribokontakta, obraba, trajnost

*Naslov avtorja za dopisovanje: Nacionalna univerza za letalstvo, Fakulteta za letalski in vesoljski inženiring, Lubomyr Huzar 1, 03680 Kyiv, Ukrajina, anatoliykor80@gmail.com

Strojniški vestnik - Journal of Mechanical Engineering 67(2021)7-8, SI 48

Prejeto v recenzijo: 2021-03-09
Prejeto popravljeno: 2021-05-18
Odobreno za objavo: 2021-06-28

Eksperimentalna raziskava in matematični model toplotne prehodnosti dvokapnega solarnega destilatorja

Raj Vardhan Patel[1,2], Anshul Yadav[1,2], Jerzy Winczek[3]*

[1]Inštitut za tehnologijo Kamla Nehru, Indija
[2]CSIR - centralni inštitut za raziskave soli in morskih kemikalij, Indija
[3]Tehniška univerza v Čenstohovi, Poljska

Zmogljivost solarnih destilatorjev je odvisna od prenosa toplote v destilatorju, vode v posodi, hitrosti vetra (za hlajenje steklene strehe), itd.

Pričujoča študija obravnava odvisnost toplotne prehodnosti od temperature vode v posodi in hitrosti vetra pri akrilnem solarnem destilatorju, ki je zasnovan za poletne klimatske razmere v Sultanpuru v Indiji. Opravljene so bile eksperimentalne študije za preučitev vpliva vode v posodi in hitrosti vetra na toplotno prehodnost (s konvekcijo, uparjanjem in sevanjem) in kapaciteto solarnega destilatorja. Razvit je bil matematični model za preučitev vpliva globine vode v posodi in hitrosti vetra na prenos toplote in zmogljivost solarnega destilatorja. Ta je bil za poskuse postavljen v smeri vzhod-zahod. S sedmimi digitalnimi temperaturnimi tipali so bile zabeležene vrednosti temperature na različnih mestih v destilatorju. Podatki o sončnem obsevanju, temperaturi okolice in hitrosti vetra so bili pridobljeni iz postaje za spremljanje sončnega sevanja SRRA na inštitutu KNIT v Sultanpuru v Indiji. Hitrost vetra je bila izmerjena z digitalnim anemometrom. Trenutna temperatura je bila odčitana vsako uro. Matematični model je bil uporabljen tudi za primerjavo zmogljivosti in toplotne prehodnosti dvokapnega solarnega destilatorja z rezultati eksperimentov. Ugotovljeno je bilo, da je konvektivna toplotna prestopnost odvisna od mase in temperature vode v posodi ter od temperature steklene strehe. Najvišji vrednosti h_{ew} (5,05 W/(m²K) in 3,08 W/(m²K)) ter h_{cw} (2,48 W/(m²K) in 2,8 W/(m²K)) sta bili ugotovljeni pri globinah 2 cm oz. 5 cm. Največja sevalna toplotna prestopnost znaša 3,8 W/(m²K) pri globini 2 cm in se povečuje s kondenzacijo. Vodna para med kondenziranjem namreč oddaja toploto stekleni površini in jo tako segreva. Ko se globina poveča z 2 cm na 5 cm, se zmogljivost destilatorja zmanjša za 25,45 %. Največja dnevna zmogljivost 2,5 l/m²/dan je bila ugotovljena pri globini vode 2 cm. Zmogljivost destilatorja se povečuje s porastom hitrosti vetra, saj kondenzacija na stekleni površini poteka hitreje. Do tega pride zaradi povišanja temperaturne razlike med stekleno streho in vodo v posodi.

Prednost pasivnih solarnih destilatorjev je v nizki ceni in v nižjih stroških vzdrževanja, njihova pomanjkljivost pa je majhna zmogljivost. Za večjo zmogljivost so potrebni aktivni solarni destilatorji. Zmogljivost pasivnih destilatorjev je odvisna od dejavnikov, kot so hlajenje steklene strehe, materiali posode itd.

V študiji niso bili upoštevani vpliv hlajenja steklene strehe zaradi tekoče vode, vpliv različnih materialov posode, debelina steklene strehe in vpliv oblike posode. Te dejavnike bo mogoče upoštevati v prihodnjih študijah solarnih destilatorjev. Preučiti bo mogoče tudi vključitev sončnih kolektorjev in virov odpadne toplote. Razvoj matematičnega modela optimalne integracije sončnih kolektorjev bi pripomogel k prihodnjim raziskavam solarnih destilatorjev. Tudi masni pretok tekočine, ki kroži skozi kolektorje, ima pomembno vlogo pri izkoriščanju toplote. Možna je optimizacija masnega pretoka in globine vode v posodi destilatorja.

Prenos toplote v destilatorju bi bilo mogoče še dodatno povečati z uporabo nanofluidov. Možnost za izboljšanje prehajanja toplote iz posode na stekleno streho in s tem kapacitete predstavljajo tudi rebra v posodi in notranji odsevniki. V vsakem primeru je izkoristek solarnega destilatorja odvisen od temperaturne razlike med vodo v posodi in stekleno streho.

Ključne besede: dvokapni solarni destilator, sončna energija, destilacija, koeficient prenosa toplote

*Naslov avtorja za dopisovanje: Tehniška univerza v Čenstohovi, 42201 Czestochowa, Poljska, winczek@gmail.com

Strojniški vestnik - Journal of Mechanical Engineering 67(2021)7-8, SI 49

Prejeto v recenzijo: 2021-05-12
Prejeto popravljeno: 2021-06-17
Odobreno za objavo: 2021-07-09

Mehanske lastnosti lepljenih spojev, izdelanih z lepili, občutljivimi na tlak

Anna Rudawska[1,*] – Magd Abdel Wahab[2,3]

[1]Tehniška univerza v Lublinu, Fakulteta za strojništvo, Poljska
[2]Univerza Duy Tan, Razvojno-raziskovalni inštitut, Vietnam
[3]Univerza v Ghentu, Fakulteta za inženiring in arhitekturo, Belgija

Članek obravnava mehanske lastnosti lepljenih spojev, izdelanih z akrilnimi lepili, občutljivimi na tlak. Lepljeni spoji z industrijskimi lepilnimi trakovi, občutljivimi na tlak, so bili v preskusih izpostavljeni več temperaturnim ciklom.

V preskusih sta bili uporabljeni dve vrsti akrilnih lepilnih trakov in tri vrste gradbenih materialov: pločevina iz konstrukcijskega jekla (C45), pločevina iz aluminijeve zlitine (EN-AW 5754) in titanova pločevina (kvalitete 2). Trdnostni preskusi lepljenih spojev so bili opravljeni po kondicioniranju na sobni temperaturi (23 °C) in po 80 temperaturnih ciklih v območju +60 °C/–40 °C. Trdnostni preskusi so bili izvedeni po standardu DIN EN 1465 na stroju Zwick/Roell Z10.

Pri lepljenih spojih, ki so bili izpostavljeni temperaturnim ciklom, ni bilo ugotovljeno poslabšanje mehanskih lastnosti. Lepilni trakovi, občutljivi na tlak, imajo dobro sposobnost lepljenja obravnavanih materialov v danih pogojih. Glavna ugotovitev raziskave je, da temperaturni cikli pozitivno vplivajo na mehansko trdnost spojev, izdelanih z lepilnimi trakovi, občutljivimi na tlak.

Novost pričujoče raziskave je v izpostavitvi omenjenih spojev temperaturnim ciklom v imenovanem območju. Rezultati bodo uporabni pri načrtovanju spojev z uporabo lepilnih trakov, občutljivih na tlak, zlasti tistih, namenjenih obratovanju v prisotnosti temperaturnih ciklov.

Ključne besede: lepljeni spoj, jeklo, aluminijeva zlitina, lepilo, občutljivo na tlak, mehanske lastnosti, temperaturni šoki

*Naslov avtorja za dopisovanje: Tehniška univerza v Lublinu, Nadbystrzycka 38D, Lublin, Poljska, a.rudawska@pollub.pl

Strojniški vestnik - Journal of Mechanical Engineering 67(2021)7-8, SI 50

Prejeto v recenzijo: 2021-05-23
Prejeto popravljeno: 2021-07-01
Odobreno za objavo: 2021-07-12

Karakterizacija spoja AZ31 AW-6060, izdelanega po postopku sestavljenega litja z vmesno plastjo Zn pri razmeroma nizkih temperaturah

Tomasz Bucki[1,*] – Marek Konieczny[1] – Dana Bolibruchova[2] – Sylwia Rzepa[3]

[1]Tehniška univerza Kielce, Fakulteta za mehatroniko in strojništvo, Poljska
[2]Univerza v Žilini, Fakulteta za strojništvo, Slovaška republika
[3]COMTES FHT a.s., Oddelek za mehanske preiskave in termofizikalne meritve, Češka republika

V zadnjih letih je opazen znaten porast uporabe bimetalnih elementov na osnovi lahkih kovin, natančneje aluminija in magnezija. Uveljavljajo se na mnogih področjih, npr. v avtomobilski industriji, kjer prispevajo k zmanjšanju mase vozil in s tem porabe goriva. Magnezijeve in aluminijeve zlitine je mogoče kombinirati z različnimi tehnikami. Pri metalurškem spajanju Mg in Al se običajno formirajo intermetalne faze Mg-Al, ki so same po sebi krhke in povzročijo, da ima spoj slabe mehanske lastnosti. Sestavljeno litje je postopek spajanja podobnih ali raznorodnih zlitin z nalivanjem raztaljene zlitine na drugo zlitino, ki je v trdnem stanju. Proces omogoča razmeroma preprosto in ekonomično proizvodnjo bimetalov v najrazličnejših oblikah in dimenzijah.

Članek obravnava izdelavo spoja magnezijeve zlitine AZ31 in aluminijeve zlitine AW-6060 z vmesno plastjo Zn. Uporabljeno je bilo temperaturno območje, ki je v primerjavi s podatki iz literature razmeroma nizko. Po postopku difuzijskega spajanja je bila na površino vložka AW-6060 nanesena plast Zn. Vložek je bil vstavljen v jeklen kalup na sobni temperaturi in spoj je bil nato izdelan po postopku sestavljenega litja tako, da je bil kalup napolnjen s tekočo zlitino AZ31, ogreto na 650 °C. Predmet študije sta bili analiza mikrostrukture ter preiskava mikrotrdote in strižne trdnosti izdelanega spoja. Mikrostruktura je bila preučena pod optičnim mikroskopom in z vrstičnim elektronskim mikroskopom, opremljenim z energijsko disperzijskim rentgenskim spektrometrom. Izmerjena je bila tudi mikrotrdota po Vickersu. Trdnost spoja je bila določena s strižnim preskusom.

Ugotovljeno je bilo, da se je med zlitinama oblikoval 400 µm debel spoj. Mikrostrukturna analiza je pokazala, da je za območje spoja značilna visoka koncentracija Zn in Mg. Spoj na strani AZ31 sestavljata evtektoid z intermetalno fazo MgZn ter trdna raztopina Al in Zn v Mg. V osrednjem delu območja spoja so bili ugotovljeni delci ternarne intermetalne faze $Mg_5Al_2Zn_2$ in tanek sloj te faze. V območju zraven AW-6060 je bila ugotovljena osnova $Mg(Al,Zn)_2$ s finimi delci drugih faz. Za območje spoja je značilna višja mikrotrdota kot pri obeh zlitinah. Najvišje vrednosti mikrotrdote so bile ugotovljene v območju s fazo $Mg(Al,Zn)_2$ ter v sloju, sestavljenem iz faze $Mg_5Al_2Zn_2$. Meritve mikrotrdote v tem predelu so povzročile širjenje manjših razpok v okolici konice merilnika trdote po Vickersu, ki dokazujejo opazno krhkost faz. Povprečna strižna trdnost spoja je znašala 19,6 ± 2,5 MPa.

Rezultati študije bogatijo znanje na področju spajanja Mg in Al zlitin po postopku sestavljenega litja. Ugotovljen je bil vpliv vmesne plasti Zn na oblikovanje spoja. Uporaba te plasti je omogočila oblikovanje spoja brez krhkih faz Mg-Al. Predstavljeni spoj je glede na podatke v literaturi manj krhek in ima boljše mehanske lastnosti kot spoji, izdelani brez vmesne plasti. Ugotovljeno je bilo tudi to, da temperaturne razmere pomembno vplivajo na oblikovanje spoja z vmesno plastjo Zn. Pri nizkih temperaturah so se formirale faze, bogate z Mg in Zn, pri povišanih temperaturah pa je bila ugotovljena višja vsebnost Al. Iz predstavljenih rezultatov sledi sklep, da je uporaba vmesnih plasti obetavna rešitev za spajanje zlitin Mg in Al. Z ustrezno modifikacijo mikrostrukture spoja je mogoče znatno izboljšati njegove mehanske lastnosti, s tem pa uporabnost materialov.

Ključne besede: sestavljeno litje, magnezijeva zlitina, aluminijeva zlitina, cinkova vmesna plast, mikrostruktura, mehanske lastnosti

*Naslov avtorja za dopisovanje: Tehniška univerza Kielce, Fakulteta za mehatroniko in strojništvo, 25-314 Kielce, Poljska, tbucki@tu.kielce.pl

Guide for Authors

All manuscripts must be in English. Pages should be numbered sequentially. The manuscript should be composed in accordance with the Article Template given above. The maximum length of contributions is 12 pages (approx. 5000 words). Longer contributions will only be accepted if authors provide justification in a cover letter. For full instructions see the Information for Authors section on the journal's website: http://en.sv-jme.eu .

SUBMISSION:

Submission to SV-JME is made with the implicit understanding that neither the manuscript nor the essence of its content has been published previously either in whole or in part and that it is not being considered for publication elsewhere. All the listed authors should have agreed on the content and the corresponding (submitting) author is responsible for having ensured that this agreement has been reached. The acceptance of an article is based entirely on its scientific merit, as judged by peer review. Scientific articles comprising simulations only will not be accepted for publication; simulations must be accompanied by experimental results carried out to confirm or deny the accuracy of the simulation. Every manuscript submitted to the SV-JME undergoes a peer-review process.

The authors are kindly invited to submit the paper through our web site: http://ojs.sv-jme.eu. The Author is able to track the submission through the editorial process - as well as participate in the copyediting and proofreading of submissions accepted for publication - by logging in, and using the username and password provided.

SUBMISSION CONTENT:

The typical submission material consists of:

- A **manuscript** (A PDF file, with title, all authors with affiliations, abstract, keywords, highlights, inserted figures and tables and references),
- Supplementary files:
  - a **manuscript** in a WORD file format
  - a **cover letter** (please see instructions for composing the cover letter)
  - a ZIP file containing **figures** in high resolution in one of the graphical formats (please see instructions for preparing the figure files)
  - possible **appendicies** (optional), cover materials, video materials, etc.

Incomplete or improperly prepared submissions will be rejected with explanatory comments provided. In this case we will kindly ask the authors to carefully read the Information for Authors and to resubmit their manuscripts taking into consideration our comments.

COVER LETTER INSTRUCTIONS:

Please add a **cover letter** stating the following information about the submitted paper:

1. Paper **title**, list of **authors** and their **affiliations**. **One** corresponding author should be provided.
2. **Type of paper**: original scientific paper (1.01), review scientific paper (1.02) or short scientific paper (1.03).
3. A **declaration** that neither the manuscript nor the essence of its content has been published in whole or in part previously and that it is not being considered for publication elsewhere.
4. State the **value of the paper** or its practical, theoretical and scientific implications. What is new in the paper with respect to the state-of-the-art in the published papers? Do not repeat the content of your abstract for this purpose.
5. We kindly ask you to suggest at least two **reviewers** for your paper and give us their names, their full affiliation and contact information, and their scientific research interest. The suggested reviewers should have at least two relevant references (with an impact factor) to the scientific field concerned; they should not be from the same country as the authors and should have no close connection with the authors.

FORMAT OF THE MANUSCRIPT:

The manuscript should be composed in accordance with the Article Template. The manuscript should be written in the following format:

- A **Title** that adequately describes the content of the manuscript.
- A list of **Authors** and their **affiliations**.
- An **Abstract** that should not exceed 250 words. The Abstract should state the principal objectives and the scope of the investigation, as well as the methodology employed. It should summarize the results and state the principal conclusions.
- 4 to 6 significant **key words** should follow the abstract to aid indexing.
- 4 to 6 **highlights;** a short collection of bullet points that convey the core findings and provide readers with a quick textual overview of the article. These four to six bullet points should describe the essence of the research (e.g. results or conclusions) and highlight what is distinctive about it.
- An **Introduction** that should provide a review of recent literature and sufficient background information to allow the results of the article to be understood and evaluated.
- A **Methods** section detailing the theoretical or experimental methods used.
- An **Experimental section** that should provide details of the experimental set-up and the methods used to obtain the results.
- A **Results** section that should clearly and concisely present the data, using figures and tables where appropriate.
- A **Discussion** section that should describe the relationships and generalizations shown by the results and discuss the significance of the results, making comparisons with previously published work. (It may be appropriate to combine the Results and Discussion sections into a single section to improve clarity.)
- A **Conclusions** section that should present one or more conclusions drawn from the results and subsequent discussion and should not duplicate the Abstract.
- **Acknowledgement** (optional) of collaboration or preparation assistance may be included. Please note the source of funding for the research.
- **Nomenclature** (optional). Papers with many symbols should have a nomenclature that defines all symbols with units, inserted above the references. If one is used, it must contain all the symbols used in the manuscript and the definitions should not be repeated in the text. In all cases, identify the symbols used if they are not widely recognized in the profession. Define acronyms in the text, not in the nomenclature.
- **References** must be cited consecutively in the text using square brackets [1] and collected together in a reference list at the end of the manuscript.
- **Appendix(-icies)** if any.

SPECIAL NOTES

Units: The SI system of units for nomenclature, symbols and abbreviations should be followed closely. Symbols for physical quantities in the text should be written in italics (e.g. *v*, *T*, *n*, etc.). Symbols for units that consist of letters should be in plain text (e.g. ms^{-1}, K, min, mm, etc.). Please also see: http://physics.nist.gov/cuu/pdf/sp811.pdf .

Abbreviations should be spelt out in full on first appearance followed by the abbreviation in parentheses, e.g. variable time geometry (VTG). The meaning of symbols and units belonging to symbols should be explained in each case or cited in a **nomenclature** section at the end of the manuscript before the References.

Figures (figures, graphs, illustrations digital images, photographs) must be cited in consecutive numerical order in the text and referred to in both the text and the captions as Fig. 1, Fig. 2, etc. Figures should be prepared without borders and on white grounding and should be sent separately in their original formats. If a figure is composed of several parts, please mark each part with a), b), c), etc. and provide an explanation for each part in Figure caption. The caption should be self-explanatory. Letters and numbers should be readable (Arial or Times New Roman, min 6 pt with equal sizes and fonts in all figures). Graphics (submitted as supplementary files) may be exported in resolution good enough for printing (min. 300 dpi) in any common format, e.g. TIFF, BMP or JPG, PDF and should be named Fig1.jpg, Fig2.tif, etc. However, graphs and line drawings should be prepared as vector images, e.g. CDR, AI. Multi-curve graphs should have individual curves marked with a symbol or otherwise provide distinguishing differences using, for example, different thicknesses or dashing.

Tables should carry separate titles and must be numbered in consecutive numerical order in the text and referred to in both the text and the captions as Table 1, Table 2, etc. In addition to the physical quantities, such as *t* (in italics), the units [s] (normal text) should be added in square brackets. Tables should not duplicate data found elsewhere in the manuscript. Tables should be prepared using a table editor and not inserted as a graphic.

REFERENCES:

A reference list must be included using the following information as a guide. Only cited text references are to be included. Each reference is to be referred to in the text by a number enclosed in a square bracket (i.e. [3] or [2] to [4] for more references; do not combine more than 3 references, explain each). No reference to the author is necessary.

References must be numbered and ordered according to where they are first mentioned in the paper, not alphabetically. All references must be complete and accurate. Please add DOI code when available. Examples follow.

Journal Papers:

Surname 1, Initials, Surname 2, Initials (year). Title. Journal, volume, number, pages, DOI code.

[1] Hackenschmidt, R., Alber-Laukant, B., Rieg, F. (2010). Simulating nonlinear materials under centrifugal forces by using intelligent cross-linked simulations. *Strojniški vestnik - Journal of Mechanical Engineering,* vol. 57, no. 7-8, p. 531-538, DOI:10.5545/sv-jme.2011.013.

Journal titles should not be abbreviated. Note that journal title is set in italics.

Books:

Surname 1, Initials, Surname 2, Initials (year). Title. Publisher, place of publication.

[2] Groover, M.P. (2007). *Fundamentals of Modern Manufacturing*. John Wiley & Sons, Hoboken.

Note that the title of the book is italicized.

Chapters in Books:

Surname 1, Initials, Surname 2, Initials (year). Chapter title. Editor(s) of book, book title. Publisher, place of publication, pages.

[3] Carbone, G., Ceccarelli, M. (2005). Legged robotic systems. Kordić, V., Lazinica, A., Merdan, M. (Eds.), Cutting Edge Robotics. Pro literatur Verlag, Mammendorf, p. 553-576.

Proceedings Papers:

Surname 1, Initials, Surname 2, Initials (year). Paper title. Proceedings title, pages.

[4] Štefanić, N., Martinčević-Mikić, S., Tošanović, N. (2009). Applied lean system in process industry. *MOTSP Conference Proceedings*, p. 422-427.

Standards:

Standard-Code (year). Title. Organisation. Place.

[5] ISO/DIS 16000-6.2:2002. *Indoor Air – Part 6: Determination of Volatile Organic Compounds in Indoor and Chamber Air by Active Sampling on TENAX TA Sorbent, Thermal Desorption and Gas Chromatography using MSD/FID.* International Organization for Standardization. Geneva.

WWW pages:

Surname, Initials or Company name. Title, from http://address, date of access.

[6] Rockwell Automation. Arena, from *http://www.arenasimulation.com,* accessed on 2009-09-07.

EXTENDED ABSTRACT:

When the paper is accepted for publishing, the authors will be requested to send an **extended abstract** (approx. one A4 page or 3500 to 4000 characters or approx. 600 words). The instruction for composing the extended abstract are published on-line: http://www.sv-jme.eu/information-for-authors/ .

COPYRIGHT:

Authors submitting a manuscript do so on the understanding that the work has not been published before, is not being considered for publication elsewhere and has been read and approved by all authors. The submission of the manuscript by the authors means that the authors automatically agree to transfer copyright to SV-JME when the manuscript is accepted for publication. All accepted manuscripts must be accompanied by a Copyright Transfer Agreement, which should be sent to the editor. The work should be original work by the authors and not be published elsewhere in any language without the written consent of the publisher. The proof will be sent to the author showing the final layout of the article. Proof correction must be minimal and executed quickly. Thus it is essential that manuscripts are accurate when submitted. Authors can track the status of their accepted articles on http://en.sv-jme.eu/.

PUBLICATION FEE:

Authors will be asked to pay a publication fee for each article prior to the article appearing in the journal. However, this fee only needs to be paid after the article has been accepted for publishing. The fee is 380 EUR (for articles with maximum of 6 pages), 470 EUR (for articles with maximum of 10 pages), plus 50 EUR for each additional page. The additional cost for a color page is 90.00 EUR (only for a journal hard copy; optional upon author's request). These fees do not include tax.

Strojniški vestnik -Journal of Mechanical Engineering
Aškerčeva 6, 1000 Ljubljana, Slovenia, e-mail: info@sv-jme.eu

ISSN 0039-2480

http://www.sv-jme.eu

Contents

Papers